

Copyright

by

Samantha Sparr Taylor

2019

**The Dissertation Committee for Samantha Sparr Taylor Certifies that this is the approved version of the following Dissertation:**

**Investigating Surface Topography Effects on Directional Emissivity of Metallic Additively Manufactured Parts**

**Committee:**

---

Joseph J. Beaman, Supervisor

---

Carolyn C. Seepersad

---

Eric M. Taleff

---

Alexander J. Heltzel

---

Eric C. Forrest

**Investigating Surface Topography Effects on Directional Emissivity of  
Metallic Additively Manufactured Parts**

**by**

**Samantha Sparr Taylor**

**Dissertation**

Presented to the Faculty of the Graduate School of

The University of Texas at Austin

in Partial Fulfillment

of the Requirements

for the Degree of

**Doctor of Philosophy**

**The University of Texas at Austin**

**August 2019**

## **Dedication**

This dissertation is dedicated to my family and friends who have supported me throughout this entire process. I am extremely grateful for all that they have done.

## **Acknowledgements**

I would like to thank my committee for their time and feedback during this research project. I would like to give a special thanks to my advisor Dr. Beaman for his support and guidance throughout this process. I also want to give a special thanks to Dr. Fish for his guidance during my time at Texas. I want to thank Bradley Jared, Josh Koepke, Jeremy Wright, Nick Calta, and Josh Stanford for their help. I would like to give a special thanks to Allen Roach for mentoring me during my time at Sandia National Labs. I would also like to give a special thanks to Eric Forrest, who has helped me throughout this project.

\*Supported by the Laboratory Directed Research and Development program at Sandia National Laboratories, a multi-mission laboratory managed and operated by National Technology and Engineering Solutions of Sandia, LLC, a wholly owned subsidiary of Honeywell International, Inc., for the U.S. Department of Energy's National Nuclear Security Administration under contract DE-NA0003525.

This dissertation describes objective technical results and analysis. Any subjective views or opinions that might be expressed in the dissertation do not necessarily represent the views of the U.S. Department of Energy or the United States Government.

SAND2019-8440 T

## **Abstract**

# **Investigating Surface Topography Effects on Directional Emissivity of Metallic Additively Manufactured Parts**

Samantha Sparr Taylor, PhD

The University of Texas at Austin, 2019

Supervisor: Joseph J. Beaman

Researchers are focusing on qualification methods and simulations to gain a better understanding of metal powder bed additive manufacturing (AM) processes. Because of the direct relationship between thermal history and mechanical behavior, in-situ thermal monitoring is key in gauging the quality of both the process and produced parts. To accurately monitor the temperatures of an AM process, key environment and object parameters need to be known, most importantly, object emissivity. The emissivity of an object is dependent on several variables, including: wavelength of light, material composition, temperature, and surface topography. Most have been concerned with the thermal emissivity dependence on temperature since large temperature ranges are seen in metal powder bed processes, but there is also an extensive range of surfaces produced by AM. This work will focus on discovering what surface characteristics control directional thermal emissivity. In addition to defining the surface characteristics, in build conditions

will be simulated while conducting thermal measurements of AM parts to quantify errors that result from incorrect emissivity assumptions. Lastly, a method for determining the surface topography in-situ to allow for layerwise correction of emissivity will be implemented in an additive machine.

## Table of Contents

List of Tables .....	xi
List of Figures.....	xii
<b>INTRODUCTION .....</b>	<b>1</b>
<b>BACKGROUND .....</b>	<b>3</b>
Thermal Monitoring in AM.....	3
Radiation and Emissivity.....	4
Surface Roughness Standards.....	6
Surface Roughness in Additive Manufacturing .....	9
Surface Roughness and Emissivity .....	12
<b>RESEARCH PLAN .....</b>	<b>14</b>
<b>CHAPTER 1: DEFINING SURFACE CHARACTERISTICS THAT AFFECT EMISSIVITY .....</b>	<b>17</b>
Simulations .....	17
Initial Simulation Decisions .....	17
Material .....	19
Simulation Wavelength Range.....	20
Simulation Region - Boundary Conditions and Mesh.....	21
Source Radiation .....	23
Simulation Monitors.....	23
Parameter Sweep .....	24
Surface Roughness Analysis .....	24
Simulations Performed .....	25
Isosceles Triangle .....	25

3D Isosceles Pyramid .....	31
Parabolic Valley .....	34
Flat Valley .....	37
Skewed Triangles .....	41
Variable Sized Peaks .....	45
Overall Simulation Results.....	49
Experimental Surface Roughness and Emissivity Correlation.....	51
Sample Fabrication.....	52
Surface Roughness Measurement .....	61
Emissivity Measurements.....	68
Oxide Layer Measurement .....	72
Emissivity Dependence on Surface Roughness .....	75
Conclusions .....	81
<b>CHAPTER 2: ANGULAR SENSITIVITY OF SURFACE ROUGHNESS DEPENDENT</b>	
<b>EMISSIVITY BEHAVIOR .....</b>	<b>83</b>
Vacuum Furnace Setup.....	83
Simulating in Build Environment.....	86
Experimental Procedure .....	88
Sample Selection .....	91
Results .....	94
Room Temperature Measurements .....	94
Raised Temperature Measurements .....	96

<b>CHAPTER 3: IN-SITU MEASUREMENTS .....</b>	<b>103</b>
Surface Topography Measurement Technique Selection Process.....	103
Experimental Procedure .....	107
Results .....	111
Conclusion.....	113
<b>OVERALL CONCLUSIONS .....</b>	<b>114</b>
Future Work.....	115
Appendix A - Surface Roughness vs Emissivity Analysis.....	117
<b>REFERENCES .....</b>	<b>118</b>

## List of Tables

<b>Table 1:</b> Optical Index of Refraction Data Calculated for 304 Stainless Steel. ....	20
<b>Table 2:</b> Isosceles Triangle Parameter Sweep Ranges. ....	26
<b>Table 3:</b> 3D Pyramid Parameter Sweep Ranges. ....	32
<b>Table 4:</b> Parabolic Valley Parameter Sweep Ranges.....	35
<b>Table 5:</b> Flat Valley Parameter Sweep Variable Ranges.....	38
<b>Table 6:</b> Symmetric Skewed Triangles Parameter Sweep Variable Ranges. ....	42
<b>Table 7:</b> Three Peak Skewed Triangle Parameter Sweep Variable Ranges. ....	43
<b>Table 8:</b> Variable Sized Peaks - Height Change Parameter Sweep Values.....	45
<b>Table 9:</b> Variable Sized Peaks - Width Change Parameter Sweep Values.....	46
<b>Table 10:</b> Variable Sample Build Parameter Combinations.....	59
<b>Table 11:</b> Constant Sample Build Parameters. ....	59
<b>Table 12:</b> Keyence VR3100 Repeatability. ....	63
<b>Table 13:</b> Hemispherical Emissivity Results of DMLS Samples.....	71
<b>Table 14:</b> Surface Roughness Variation Among Nine Measurement Points Taken Within AM Samples. ....	81
<b>Table 15:</b> Selected Samples for Vacuum Furnace Tests. ....	92
<b>Table 16:</b> Possible Temperature Errors Due to Incorrect Emissivity Assumptions. ....	102
<b>Table 17:</b> OCT Part Build Settings.....	108
<b>Table 18:</b> Build Parameters for OCT AM Specimens.....	109
<b>Table 19:</b> Keyence VR3100 Measurement Resolution Based on Magnification Level. ....	110
<b>Table 20:</b> Surface Roughness Differences between Measurement Techniques. ....	111
<b>Table 21:</b> Correlation Strengths of Surface Roughness Parameters and Combinations of Parameters to Measured Sample Emissivity .....	117

## List of Figures

<b>Figure 1:</b> Planck's Distribution .....	5
<b>Figure 2:</b> Surface Roughness Variables Diagram .....	7
<b>Figure 3:</b> Optical Focus Variation Surface Topography Measurement of Selective Laser Melting Part .....	9
<b>Figure 4:</b> Emissivity Regimes based on Surface Roughness .....	12
<b>Figure 5:</b> Characteristic Optical Simulation with Labeled Parts. ....	22
<b>Figure 6:</b> New Surface Roughness Measurement Definition Diagram. ....	25
<b>Figure 7:</b> Isosceles Triangle Optical Simulation Setup. ....	26
<b>Figure 8:</b> Surface Roughness Parameters Plotted Against Emissivity for Observation Wavelength = 1 micron. ....	27
<b>Figure 9:</b> Surface Roughness Parameters Plotted Against Emissivity for Observation Wavelength = 3.11 microns. ....	28
<b>Figure 10:</b> Surface Roughness Parameters Plotted Against Emissivity for Observation Wavelength = 7 microns. ....	30
<b>Figure 11:</b> Surface Roughness Parameters Plotted Against Emissivity for Observation Wavelength = 14 microns. ....	30
<b>Figure 12:</b> 3D Pyramid Simulation Setup. ....	32
<b>Figure 13:</b> Top Down View of Reduced Simulation Space with Symmetry Boundary Conditions. ....	32
<b>Figure 14:</b> Surface Roughness Parameters Plotted Against Emissivity for Observation Wavelength = 1 microns for 3D Pyramid Simulation. ....	33
<b>Figure 15:</b> Surface Roughness Parameters Plotted Against Emissivity for Observation Wavelength = 14 microns for 3D Pyramid Simulation. ....	34
<b>Figure 16:</b> Parabolic Valley Optical Simulation Setup. ....	35
<b>Figure 17:</b> Parabolic Valley Simulation - Surface Roughness Parameters Plotted Against Emissivity for Observation Wavelength = 1 micron. ....	36
<b>Figure 18:</b> Parabolic Valley Simulation - Surface Roughness Parameters Plotted Against Emissivity for Observation Wavelength = 7 microns. ....	36
<b>Figure 19:</b> (LEFT) Internal Reflections for Isosceles Triangle Simulation (RIGHT) Internal Reflection for Parabolic Valley Simulation. ....	37
<b>Figure 20:</b> Flat Valley Optical Simulation Setup. ....	38
<b>Figure 21:</b> Surface Plot Describing Emissivity Dependence on Valley Width and Peak Height for Observation Wavelength = 1 micron. ....	39
<b>Figure 22:</b> Surface Plot Describing Emissivity Dependence on Valley Width and Peak Height for Observation Wavelength = 7 microns. ....	39
<b>Figure 23:</b> Surface Plot Describing Emissivity Dependence on Valley Width and Peak Height for Observation Wavelength = 14 microns. ....	40
<b>Figure 24:</b> Symmetric Skewed Triangles Optical Simulation Setup. ....	41
<b>Figure 25:</b> Peak Apex Coordinate Definition Diagram. ....	41
<b>Figure 26:</b> (TOP) Peak Angle Normalized with Observation Wavelength Plotted Against Emissivity (BOTTOM) Valley Angle Normalized with Observation Angle Plotted Against Emissivity. ....	42

<b>Figure 27:</b> Three Peak Skewed Triangle Simulation Geometry.....	43
<b>Figure 28:</b> Surface Roughness Parameters Plotted Against Emissivity for Three Peak Skewed Triangles with Observation Wavelength = 1 micron.....	44
<b>Figure 29:</b> Surface Roughness Parameters Plotted Against Emissivity for Three Peak Skewed Triangles with Observation Wavelength = 7 microns. ....	44
<b>Figure 30:</b> Variable Sized Peaks Simulation Geometry. ....	45
<b>Figure 31:</b> Surface Roughness Parameters Plotted Against Emissivity for Multi-Scale Peak Simulation - Height Change with Observation Wavelength = 3.11 microns. ....	46
<b>Figure 32:</b> Surface Roughness Parameters Plotted Against Emissivity for Multi-Scale Peak Simulation - Width Change with Observation Wavelength = 3.11 microns. ....	47
<b>Figure 33:</b> Multi-Scale Simulation - Small Peak Height Influence on Emissivity with Large Peak Height = 5 microns. ....	48
<b>Figure 34:</b> Multi-Scale Simulation - Small Peak Height Influence on Emissivity with Large Peak Height = 30 microns. ....	48
<b>Figure 35:</b> As Built 316 Stainless Steel Samples on Build Plate. ....	53
<b>Figure 36:</b> Density Cube Study - $S\Delta q$ as a Function of Volumetric Energy Density. ....	56
<b>Figure 37:</b> $S\Delta q$ Process Map with ProX 200 Powder. ....	57
<b>Figure 38:</b> $S\Delta q$ Process Map with ProX 320 Powder. ....	57
<b>Figure 39:</b> Build Setting Locations Superimposed on $S\Delta q$ Process Map. ....	58
<b>Figure 40:</b> Build Plan for Pair of Laser Parameter Combination Builds.....	60
<b>Figure 41:</b> Sample Position Labeling Scheme. ....	60
<b>Figure 42:</b> Keyence VR3100 Visual Macroscope Functional Diagram. ....	62
<b>Figure 43: (LEFT):</b> 12x Magnification 3D Height Map of DMLS Sample <b>(RIGHT):</b> 160x Magnification 3D Height Map of DMLS Sample. ....	63
<b>Figure 44:</b> Surface Height Measurement Locations and Labels. ....	64
<b>Figure 45: (TOP)</b> Sample $R\Delta q$ Values for Direction Perpendicular to Scan Vectors <b>(BOTTOM)</b> Sample $R\Delta q$ Values for Direction Parallel to Scan Vector ....	66
<b>Figure 46:</b> Positional Percent Deviation from Average Surface Roughness.....	67
<b>Figure 47:</b> Surface Roughness as a Function of Volumetric Energy Density. ....	68
<b>Figure 48:</b> Hemispherical Directional Reflectometer Coupled with Fourier Transform Interferometer. ....	69
<b>Figure 49:</b> HDR Functional Diagram. ....	70
<b>Figure 50:</b> HDR Measurement Planes Relative to Scanning Direction. ....	70
<b>Figure 51:</b> Total Hemispherical Emissivity based on Orientation to Scan Direction. ....	72
<b>Figure 52:</b> Total Hemispherical Emissivity based on Volumetric Energy Density. ....	72
<b>Figure 53:</b> SEM Image of Sample A from Set 2 Build 2. ....	74
<b>Figure 54:</b> Oxygen Composition Results from AES Method for Sample A from Set 2 Build 2. ....	74
<b>Figure 55:</b> Sputter Time to Signal End of Oxide Layer Versus Sample Emissivity. ....	75
<b>Figure 56:</b> Valley Angle Calculation Diagram.....	77
<b>Figure 57:</b> Linear Average Surface Roughness Plotted Against Hemispherical Emissivity. ....	78
<b>Figure 58:</b> Linear Root Mean Square Slope Plotted Against Hemispherical Emissivity. ....	78

<b>Figure 59:</b> Average Surface Roughness Multiplied by Average Tilt Angle Plotted versus Hemispherical Emissivity.....	79
<b>Figure 60:</b> Surface Valley Angle Divided by Valley Height Plotted versus Hemispherical Emissivity.....	80
<b>Figure 61:</b> Vacuum Furnace Setup Diagram.....	84
<b>Figure 62:</b> Transmission Spectrum of Sapphire Viewing Window.....	85
<b>Figure 63:</b> (LEFT) 0 Degree Sample Holder (RIGHT) 45 Degree Sample Holder.....	87
<b>Figure 64:</b> Cross Sectional View of Crucible Assembly.....	89
<b>Figure 65:</b> Energy Density Effect on Emissivity with Selected Samples Boxed.....	92
<b>Figure 66:</b> Angular Reflectance at Various Common IR Wavelength Ranges for the 0 Degree Orientation of Sample A Built from Set 4 Parameter Set A.....	93
<b>Figure 67:</b> Angular Reflectance at Various Common IR Wavelength Ranges for the 90 Degree Orientation of Sample E Built from Set 4 Parameter Set B.....	94
<b>Figure 68:</b> Emissivity Dependence on View Angle Measured with MWIR Camera at Room Temperature.....	95
<b>Figure 69:</b> Emissivity Dependence on View Angle Measured with LWIR Camera at Room Temperature.....	95
<b>Figure 70:</b> MWIR Image of Metal AM Sample Placed in 45 Degree Holder.....	97
<b>Figure 71:</b> Elevated Temperature Emissivity Results at Range of View Angles for Set 4 Build 1 Sample A.....	98
<b>Figure 72:</b> Elevated Temperature Emissivity Results at Range of View Angles for Set 4 Build 1 Sample E.....	98
<b>Figure 73:</b> Elevated Temperature Emissivity Results at Range of View Angles for Set 3 Build 1 Sample E.....	99
<b>Figure 74:</b> 45 Degree View Angle Emissivity Results for All Tested Samples.....	101
<b>Figure 75:</b> Stainless Steel 316 Cubes Built for OCT Measurement Test (Left to Right): Cube 2, Cube 7, Cube 9.....	108
<b>Figure 76:</b> Effects of Surface Topography Measurement Magnification on Level of Fit with Emissivity Trends.....	111
<b>Figure 77:</b> OCT and Keyence Microscope Surface Roughness Differences and Resultant Emissivity Differences.....	113

## INTRODUCTION

Additive manufacturing (AM) is becoming increasingly popular for a variety of applications. However, there is still hesitancy in placing AM parts in safety critical applications such as load bearing parts in the aerospace and medical industries. To overcome this lack of confidence and improve the overall quality of parts, researchers are focusing their efforts on better qualification techniques and process simulations to gain a better understanding of the parts that are produced. The focus of this dissertation is on metallic parts, as those are normally predominant in industrial applications. In metal AM processes, such as direct metal laser sintering (DMLS) or laser engineered net shaping (LENS), key issues that arise are intense thermal cycling and the residual stresses it creates within the parts. Because of the direct relationship between thermal history and mechanical behavior, in-situ thermal monitoring is key in gauging the quality of both the process and produced parts. In-situ monitoring also provides valuable data for validating the physics-based models. For proper validation and tuning of the process, the measurements need to be accurate. This is a difficult task as processes like LENS and DMLS are highly dynamic with many process variables that change based on the part application. As the process changes the part quality, it also changes the environment that the process is conducted in. To accurately monitor the thermal history of an AM process, key environment and object parameters need to be known. One of the most important of these parameters is emissivity of the object of interest. The emissivity of an object is dependent on several variables, including: material composition, temperature, and surface

topography. Most research in non-contact temperature measurement for AM applications has concerned itself with understanding the temperature dependence of emissivity. The main issue with this is that it is a circular problem. Non-contact thermal methods need emissivity to obtain an accurate temperature measurement, but to have an accurate emissivity value, the temperature must be known. Just as there is a large range in temperatures during processes for AM, there is also a large range of surface topographies produced. Surface topography in AM is dependent on many process variables that can easily change from build to build. This dissertation will focus on investigating the dependence of emissivity on surface topography. The focus will specifically be on metallic parts created with the DMLS process as it is the most popular of the metallic AM technologies and therefore has had the most research performed related to it [1]. The material of focus for this study will be 316 stainless steel as it is popular in industry and has also been the largest focus of metallic AM surface roughness research [1]. Although additive manufacturing is the application of focus for this dissertation, there is a significant impact for the scientific community for any person performing non-contact thermal measurements using a thermal imager.

## **BACKGROUND**

### **Thermal Monitoring in AM**

With the onset of additive manufacturing, new qualification needs were introduced. With traditional manufacturing techniques, material qualification and machining qualification were separate tasks. In AM, material properties are established in conjunction with part dimensions, so qualification processes must occur simultaneously. Not only do additive parts need to be qualified, but the physics of the process needs to be better understood. Many aspects of AM processes are still unknown. Therefore, process monitoring not only provides insight into part quality but a better understanding of the process itself.

Thermal monitoring is a common technique used in additive manufacturing. There are two main categories of thermal monitoring in metal additive manufacturing: melt pool and overall build surface. The melt pool thermal monitoring focuses on the temperature, size, and shape of the molten melt pool as an indication of the quality of the process. The overall build surface monitoring looks at the overall build surface and the thermal gradients over the parts. This study will focus on the thermal monitoring of the solidified parts after they have been lased, which follows the global thermal monitoring techniques. In metal AM technologies such as DMLS, LENS, and electron beam additive manufacturing (EBAM), a common thermal monitoring technique is non-contact thermal imaging with an infrared camera. For example, in Price et al., a near-infrared thermal camera was used to monitor the thermal history of parts built with the EBAM process [2]. In Cheng et al., an infrared camera was used to monitor the effects of laser process

parameters on the properties of the melt pool [3]. Not only are non-contact thermal imagers used for monitoring techniques, but they are also being implemented in control strategies. In Rodriguez et al., a long wave infrared camera is used to provide measurements and feedback for controlling the preheat temperature of the powder bed in an EBAM Arcam machine [4]. From all of these examples, it can be concluded that the reliance on thermal imaging is increasing. As the reliance on these measurements increases, so does the need for confidence in the accuracy of the measurements. In a lot of the literature, the main concern about accuracy of the measurements has been focused on the dependence of emissivity on temperature of the material of interest. However, as seen below, temperature is not the only factor that should be considered when determining thermal emissivity.

### **Radiation and Emissivity**

Thermal emissivity is the relationship between the amount of radiation emitted by an object compared to that emitted by a black body. A black body is an ideal object that absorbs and emits one hundred percent of the incident radiation. Josef Stefan found that the rate of emitted radiation from an object was based on its temperature to the fourth power [5]. In conjunction with Boltzmann's work, came the Stefan-Boltzmann law that described the emitted radiation for a gray body, which is a body that has the same emissivity for all wavelengths as seen in Equation 1 [6]. However, the gray body assumption does not hold for most objects.

$$E(T) = \varepsilon(T)\sigma T^4 \quad (1)$$

As seen with the Planck distribution, the amount of radiation changes depending on the wavelength of that radiation. As seen in Figure 1, for the ideal case of a black body, there is a complicated relationship between temperature, wavelength, and the amount of radiation given off by the body. The curves seen in Figure 1 are smooth along all wavelengths. However, for real objects, the amount of radiation emitted varies in both wavelength and direction [7]. Therefore, it is more difficult to determine an accurate temperature of an object as the emissivity is dependent on several variables, one of which is the temperature of the object, which creates a circular problem with non-contact thermal monitoring techniques.

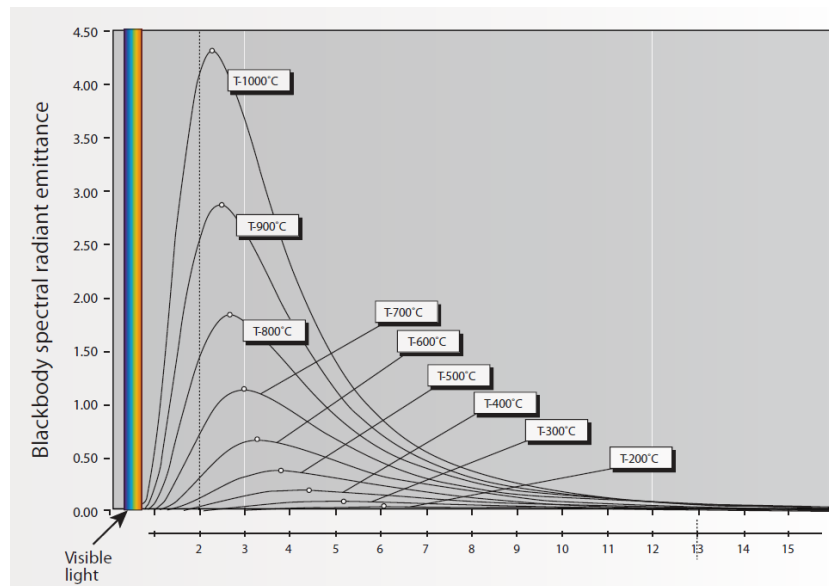


**Figure 1:** Planck's Distribution [8].

There is one method that removes the need to calculate the exact value of emissivity for a given temperature range. Two color pyrometry uses two sensors that measure radiation at two wavelengths. The wavelengths that are used for measurement

are close together so that the assumption can be made that the emissivity at both wavelengths is the same, also known as the gray body assumption. The ratio of radiation intensity measured at each wavelength is then used to calculate temperature without a direct calculation of emissivity. However, the assumption that the emissivity value is equal holds true very little of the time. This incorrect assumption had produced thermal errors when monitoring AM processes.

A very common non-contact thermal measurement method is a thermographic camera, which measures radiation in a range of wavelengths. Common wavelength ranges for thermal monitoring of AM include the near-infrared (.75-1.5 microns), short-wave infrared (1-3 microns), mid-wave infrared (3-5 microns), and long-wave infrared (8-13 microns). These cameras use a single emissivity value for calculating the temperature of an object for the camera's sensor wavelength range. The camera determines the peak radiation wavelength and fits a Planck's distribution curve to the data it gathers. Most use emissivity values either from look up tables or experimental data under constant environment conditions. With the look up tables, the surface topography is usually optically smooth or slightly rough. However, most surfaces vary from these ideal conditions.

### **Surface Roughness Standards**

There are two main standards that define surface roughness parameters: ASME B46.1 [9] and ISO 4287 [10]. These standards define standard terms when describing the topography of any surface. Within these standards, universal surface roughness

measurement parameters are defined. The most common of these standards being the average roughness, or  $R_a$ . This parameter describes the mean height of the surface roughness. The mathematical calculation can be found in Equation 2, whose parameters can be defined in Figure 2 [9]. Another parameter that is used often and is heavily related to the average roughness is the root mean square roughness,  $R_q$ . This parameter describes the average deviation of the surface height from the mean line, which can be seen in Equation 3 [9].

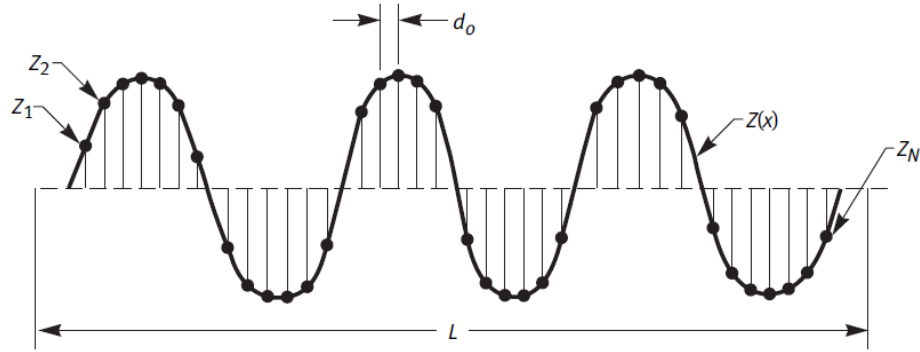


**Figure 2:** Surface Roughness Variables Diagram [9].

$$R_a = \frac{1}{L} \int_0^L |Z(x)| dx \quad (2)$$

$$R_q = \sqrt{\frac{1}{L} \int_0^L Z(x)^2 dx} \quad (3)$$

There are many other surface roughness parameters that describe characteristics such as height, spacing, and shape, but only a select few were focused on in this study due to their presence in additive manufacturing and/or optical literature related to this study.  $R_a$  and  $R_q$  were prevalent in both types of literature. The slope of the surface was referenced in optical literature, which is directly measured with  $R\Delta a$ , the average tilt

angle. The calculation of this parameter can be found in Equation 4 [9]. Another parameter related to slope, the root mean square slope ( $R\Delta q$ ) was also focused upon from suggestions in both optical and additive literature. The calculation of this is similar to  $R\Delta a$  and can be found in Equation 5 [9].

$$R\Delta a = \frac{1}{L} \int_0^L \frac{|dZ|}{|dx|} dx \quad (4)$$

$$R\Delta q = \sqrt{\frac{1}{L} \int_0^L \left(\frac{dZ}{dx}\right)^2 dx} \quad (5)$$

In addition to these linear surface roughness parameters, there are also area parameters that are used to describe the surface roughness for a given sampled area of a surface. There is the average roughness,  $S_a$ , which describes the average height of the roughness of a given area of interest. The calculation for this parameter can be found in Equation 6 [9]. Another linear parameter that is translated into an area measurement that will be used during this study is the root mean square gradient,  $S\Delta q$ . This parameter's calculation can be found in Equation 7 [11].

$$S_a = \frac{1}{A} \int_0^{L_y} \int_0^{L_x} |Z(x, y)| dx dy \quad (6)$$

$$S\Delta q = \sqrt{\frac{1}{A} \int_0^{L_y} \int_0^{L_x} \left(\frac{dZ(x, y)}{dx}\right)^2 + \left(\frac{dZ(x, y)}{dy}\right)^2 dx dy} \quad (7)$$

## Surface Roughness in Additive Manufacturing

Additive manufacturing has created unique surface finishes that range in both size and feature type depending on the process used. Although AM is only roughly thirty years old, the traditional surface roughness parameters, which can be found in standards like ASME B46.1 [9] and ISO 4287 [10], that are used to define surface topography have been used for much longer. Due to the unusual surfaces created through the various AM technologies, a need to investigate new definitions of surface roughness or employ rarely used already existing surface roughness parameters has arisen. Fused deposition modeling creates rougher, macroscale surface textures that are easily observed and measured due to the larger size of material filament used during the process. Metal processes like LENS and DMLS have somewhat finer surfaces but are still very rough compared to traditional subtractive machining techniques. An example of a DMLS surface can be found in Figure 3.

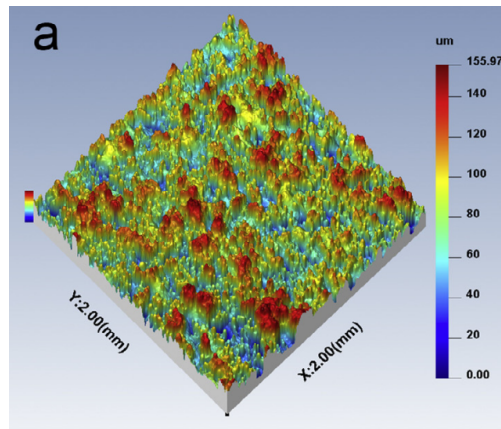


**Figure 3:** Optical Focus Variation Surface Topography Measurement of Selective Laser Melting Part [1].

In direct metal laser sintering, the surface roughness for horizontal surfaces is dictated through the thermal dynamics of the process. As the laser moves across the surface, the thermal gradients induced in the melt pool creates shear forces that affect the surface tension in the melt pool, generating a ripple effect. Since the cooling rate of the metal and laser scan speed are rapid, the ripples become frozen, creating surface texture [12]. In addition to this frozen ripple effect, balling is also another major contribution to the roughness of the horizontal surfaces. Balling can occur through the behavior referred to as Raleigh instability, which happens when the molten melt pool's length is too long compared to its width, which causes it to break up. This situation arises when the scan speed is too fast for the given laser power setting [13]. Another instance where balling can occur is the where there is a high energy density with a high power to speed ratio [13]. In that instance, balling is generated through the thermal gradients causing surface tension differences throughout the melt pool, which produces currents that pull material in an outward direction from the melt pool. When the forces are large enough, material is ejected as spherical particles from the melt pool, which then solidify, contributing to the roughness of the surface [12]. For all angled surface of the part that are not horizontal, the major contributing factors for surface roughness are partially melted powder and stair stepping. Since almost all lasers used in metal powder bed fusion processes are a Gaussian beam, the edges of the beam partially melt powder on the edges of the part due to a lack of power [12].

Since the surface texture of horizontal surfaces is highly dependent on the melt pool dynamics, certain process parameters have a considerable influence on the surface

roughness. Rombouts et al. found that scan speed and hatch spacing, which is the distance between the centerline of successive scan lines, to be the most influential process parameters on surface roughness [14]. As seen in the literature, there is a wide range of these parameters that are used in both research and industry. The scanning parameters of speed, hatch spacing, and laser power are chosen based on both material and whatever final part properties the manufacturer determines as paramount. Most research focuses on mechanical properties, for which the process parameters will be tuned to optimize. Therefore, the parameters that are chosen can have a broad range, which would result in numerous possible surface textures.

Additive manufacturing is well known for having build-to-build and even within build variability for mechanical properties and performance. This is not only true for properties like strength and ductility, but also surface roughness. As seen in Kleszczynski et al., there is a dependence on position within the build chamber for surface roughness. Identical parts with identical laser scanning parameters were created in a single build, and the surface roughness varied among the parts [15]. This demonstrates the need for in-situ monitoring of surface roughness for accurate measurements since it can change throughout a build.

The arithmetic mean height has been used for the majority of AM literature related to surface roughness [1]. It calculates the average deviation of all points on the surface from the mean line [9]. Although  $R_a$  is a commonly used surface parameter, it does not provide an adequate representation of surface topographical characteristics for many phenomena influenced by surface roughness [16]. This statement highlights the

need to define a new characteristic parameter or physics-based correlation to adequately define surfaces created through additive manufacturing processes.

## Surface Roughness and Emissivity

Surface roughness is an important property of parts that affects not only their mechanical behavior but also their thermal properties. The main concern of this investigation is on the effect of surface topography on emissivity. There are several factors that affect the thermal emissivity of parts. They include temperature of the object, material composition, possible mechanical damage caused by machining, and surface roughness [17]. When looking at how surface roughness affects thermal emissivity, there are three main cases to consider. As can be seen in Figure 4 below, the characteristic ratio is  $R_q/\lambda$ , which is a ratio between the root mean square roughness of the surface and the radiation wavelength [18].

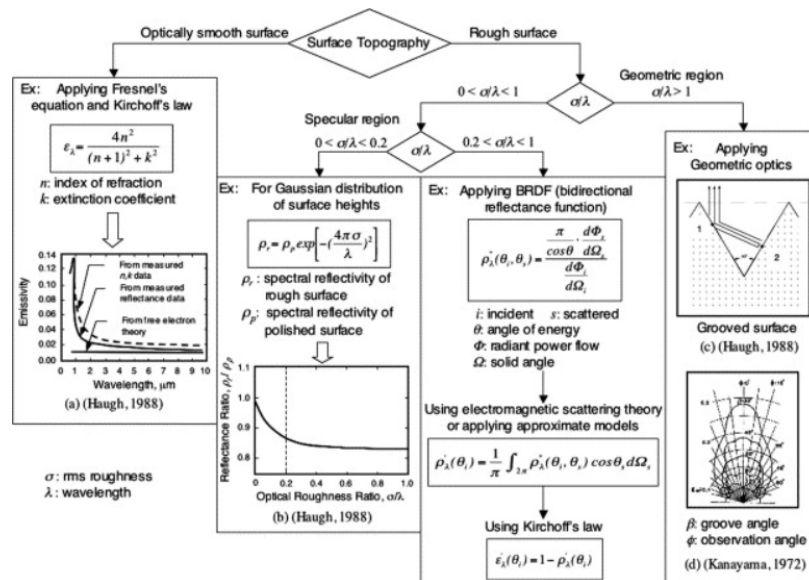


Figure 4: Emissivity Regimes Based on Surface Roughness [18].

Case 1:  $R_q / \lambda \ll 1$

This case represents an optically smooth surface, where the roughness of the surface does not affect the thermal emissivity of the object.

Case 2:  $0.2 < R_q / \lambda < 1$

This is termed the intermediate region where there is no easily defined relationship between emissivity and surface roughness. The roughness of the surface does contribute but is not solely responsible for affecting the emissivity.

Case 3:  $1 < R_q / \lambda$

In this region, termed the geometric region, it is suggested that the slope of the peaks and valleys of the surface can play a key role in emissivity trends [18].

According to Wen et al., both the slope of the grooves in the surface and the observation angle play a large part in the directional thermal emissivity of the object [18]. Similarly, according to Sabuga and Todtenhaupt, for a surface with a variety of slopes and heights, the defining property for thermal emissivity is the steepest slope [19]. The slope of the surface is captured in some respect in various surface roughness parameters, however they are not currently being used en masse to describe additive surfaces.

## RESEARCH PLAN

This study's purpose is to determine what aspect of surface topography influences thermal emissivity of metallic additively manufactured parts, quantify possible temperature errors due to incorrect emissivity assumptions, and identify a method to account for emissivity changes due to variable surface roughness common in additive manufacturing builds.

The first aspect of this dissertation will be to determine the characteristic(s) of the surface topography that affects the directional emissivity. The focus of this dissertation will be in the geometric optical region where the ratio of the average surface roughness height to the measurement wavelength is greater than or equal to one, as this commonly occurs in metallic additive manufacturing. For this initial step of the investigation, simulation work will be conducted using commercial multiphysics software. The simulations will allow for a range of geometries to be analyzed for their effect on emissivity. The results of the simulations will be used to guide the experimental exploration of the relationship between the topography of real AM surfaces and their corresponding emissivity. For the experimental side of this surface characteristic determination, metal parts will be produced using the DMLS process. 316 stainless steel is the chosen material for these parts as it is a common material in industry both for additive and conventionally manufactured parts. Once the parts are manufactured, their surfaces topographies and spectral emissivity will be measured using corresponding techniques. The raw surface topography data will then be measured for both existing and new surface roughness parameters to identify the characteristic that best describes the

changes in measured emissivity. As the calculation of traditional surface parameters is widely known, the goal of this dissertation is to provide a way to calculate a new surface parameter (or combination of existing surface parameters) that reflects the physical topographic characteristics of the surface that affects emissivity.

Once the surface characteristics have been defined, a series of experiments will be conducted to simulate simplified build conditions to look at emissivity changes. On an individual basis, the parts will each be placed in a vacuum chamber, which will be backfilled with an inert gas common to AM metal builds and heated to a range of temperatures while monitored with an infrared (IR) camera to determine the band-integrated response of certain detector and camera types commonly used for AM applications. Using the various sensors and IR camera, the emissivity trends related to surface roughness and view angle differences will be observed. These trends will be analyzed to determine the sensitivity of view angles and emissivity to the varying surface roughness of metallic AM parts. Quantification of possible errors due to incorrect emissivity assumptions will also be performed.

To make this dissertation more applicable to improve the overall process of thermal monitoring, a possible method for measuring surface topography in-situ will be determined. A range of non-contact methods that are traditionally used for measuring surface roughness will be investigated for their ability to measure the surface characteristics defined in this dissertation that affects emissivity and the ability of the method for being implemented in a commercial machine. One method will be integrated into a commercial metal AM machine. Parts will be produced, and their surfaces will be

measured with the chosen method. Ex-situ surface measurements will then be compared to the in-situ measurements to test the validity of the measurement method for in-situ emissivity adjustment.

# **CHAPTER 1: DEFINING SURFACE CHARACTERISTICS THAT AFFECT EMISSIVITY**

## **Simulations**

The first task of this study will be to determine a characteristic of the surface topography that affects the emissivity. To determine the best surface topography parameter or measurement that describes emissivity changes, simulation work will be conducted first to investigate the effects of certain geometric characteristics on emissivity as numerous simulations can be performed quickly and relatively cheaply. Geometric characteristics such as average surface height and slope were some of the characteristics that were mentioned in previous literature [18, 19]. The simulation work focused on both validating previous literature and generating surface characteristics to further investigate during the experimental portion of this task. As discussed in the introduction, there are three optical regions relating surface roughness and emissivity. The focus of the simulation work will be in the geometrical optical region, which is where  $R_q/\lambda$  is greater than or equal to one. This region, where the dependence of emissivity on surface roughness is strong, is the focus of this study as AM metallic parts are very rough compared to the shorter wavelengths commonly used for in-situ thermal monitoring [18].

### **INITIAL SIMULATION DECISIONS**

Simulations were conducted using commercial multiphysics software. Since the surface features of the additive parts are on the same order of magnitude as the wavelengths of interest, finite difference time domain (FDTD) methods for calculating emissivity are preferred over ray tracing. This is because ray tracing may not accurately

capture all optical behavior that is present when the object's features and simulated wavelengths are on the same scale [20]. The finite difference time domain methodology alternates in calculating the electric and magnetic fields. Since both fields' change in time is dependent on the other's change in space, each equation is calculated at alternating half time steps. This allows for ease of computation since simultaneous equations do not have to be solved. Due to this, Lumerical FDTD was the software package chosen to perform the simulations. The software uses a Maxwell solver, which solves Maxwell's equations of electric field, magnetic field, electric flux, and magnetic flux for the Yee cell, which is the fundamental spatial cube that makes up the simulation space [21]. This software also allows for parameter sweeps, enabling simulation of a range of geometries without having to set up each simulation individually. This saves time and allows for geometric dependent trends to be easily evaluated.

Before specific surface geometries were simulated, some overall decisions needed to be made. The first major decision was to have all the simulations be in two dimensions instead of three. Only simulating in two dimensions requires less computational time and memory requirements. There was not a significant need to simulate in three dimensions since the purpose of the simulation was to gather emissivity trends based on geometric characteristics instead of determining an absolute emissivity value for a given surface. It also offered simpler calculations of surface roughness parameters when analyzing them for their ability to predict emissivity changes.

## **Material**

The material of interest for this study is 316 stainless steel (SS) due to the popularity of this material for use in both traditional and additively manufactured parts. However, this material is not a common material used in optical simulations, as seen by it not being included in the preloaded list of common simulated materials. However, Lumerical FDTD offers several material models when simulating new materials to the software. One of the models that is common for metals is the perfect electrical conductor (PEC). The model ignores any absorption by the metal and is not suitable for this study [22]. There is also a NK model, which uses the real and imaginary parts of the optical refractive index of a material from experimental measurements to generate a best fit model to use during simulation. The closest NK data was found for 304 stainless steel, which is of similar composition to 316 compared to other metals for which NK data was available. The NK values were calculated for 304 stainless steel over a wavelength range of 0.1-12 microns, which can be seen in Table 1 [23]. Boyden and Zhang compared the calculated values to previously measured experimental data for 304 SS and concluded that it matched well [23]. The NK values were calculated using the Drude model theory, which treats a material as a sea of free electrons and is one of the most common models used for metals [24]. This data is suitable for this study's simulation as it covers most of the wavelength range of interest and is calculated at room temperature, which will be the temperature of the samples when the emissivity measurements take place [23]. Furthermore, even though the data is for 304 SS and not 316 SS, the data was used

because the focus of the simulation work was to look at general trends of emissivity based on surface geometry, not obtain absolute values of emissivity.

**Table 1:** Optical Index of Refraction Data Calculated for 304 Stainless Steel [23].

<b>Wavelength</b>	<b>N (real part of refractive index)</b>	<b>K (imaginary part of refractive index)</b>
0.100	0.184	0.662
0.500	1.863	4.804
1.000	4.281	7.303
2.000	7.632	10.075
3.000	9.997	12.049
4.000	11.907	13.702
5.000	13.549	15.162
6.000	15.012	16.488
7.000	16.343	17.712
8.000	17.573	18.855
9.000	18.722	19.931
10.000	19.804	20.952
11.000	20.830	21.925
12.000	21.807	22.856

### **Simulation Wavelength Range**

Since the focus of this study is the thermal monitoring of additive manufacturing processes, the simulation wavelength range will include the ranges of the commonly used monitoring devices. As stated in the introduction, there are three main ranges of infrared cameras that are used for thermal monitoring of additive manufacturing processes. They are short (1-3 microns), middle (3-5 microns), and long (7.5-13 microns). The wavelength range for the simulations was set at 1-14 microns to encapsulate the most common wavelengths used for AM monitoring. As stated above, the material data for the

304 SS was given between .1-12 microns, covering most of the simulation wavelength range, which is acceptable to use for this study's purpose.

### **Simulation Region - Boundary Conditions and Mesh**

For reduced computational time and ease of setup and analysis, all simulations represented unit cells of a larger periodic surface. Although AM surfaces are more randomized than traditional manufacturing techniques, periodic structures were used since the main goal was to observe which surface characteristics had the strongest effect on emissivity behavior. Therefore, the lateral boundaries along the x axis, which were placed at the edges of the unit geometry, were selected as periodic boundaries. The boundaries for the y-axis, which were horizontal, were perfectly matched layer (PML) boundaries. These absorb all incoming radiation and best simulate the radiation propagating out to infinity which would not be reflected back into the simulation region [25]. This allows a small simulation space to behave like there is an infinite area past the structure. An example of one of the simplified 2D simulations with the appropriate items labeled can be seen in Figure 5.

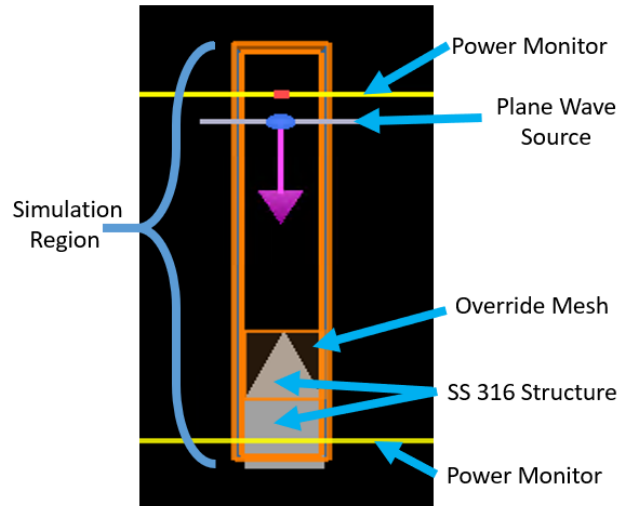


**Figure 5:** Characteristic Optical Simulation with Labeled Parts.

The mesh size of the simulation was chosen based on guidelines established by the creators of Lumerical FDTD. The setting of *conformal mesh 1* was used. This setting calculates the mesh size based on desired accuracy and simulation wavelength. For example, a conformal mesh index of 2 generates 10 mesh cells per smallest wavelength, which for this study was 1 micron so the mesh size would be 0.1 micron. A mesh index of 2 was used for all regions of the simulation, except for the interfaces between the environment and surface structure. For this, an override mesh region was created with a mesh index of 3, which generates 14 mesh cells per wavelength. As the mesh index increases, the simulation time increases as a function of mesh size to the third power, so as mesh size decreases by half, the simulation time increases by a power of eight [26]. The gained accuracy by decreasing the mesh even further is not worth the gained time, as only emissivity trends were of concern, not absolute emissivity values.

## Source Radiation

There are several illumination source options in Lumerical FDTD. The plane wave source was chosen since it best simulates diffuse radiation from the environment. However, the main source of radiation is from the part itself since during an AM build it is at an elevated temperature from the energy imparted to it from the laser. The external radiation of the part allows the emissivity trends to be found instead of absolute emission of a part at a given temperature, which is not the purpose of this study.

## Simulation Monitors

The sole focus of simulation measurements is emissivity. Since the structures in the simulation were made sufficiently thick, they are assumed to be optically opaque where there is no transmission through the structure. Another assumption made is that the emissivity is equal to the absorption of the surface. This assumption is made using Kirchoff's law, which states that under isothermal conditions and when isolated from the environment, meaning no net heat transfer, the emissivity of a surface is equal to its absorptivity [27]. Therefore, only absorption and reflection need to be measured to calculate the emission of the surface. Equation 8 was used to calculate the emissivity from the measured reflection of the surface.

$$E = A = 1 - R - T \quad (8)$$

To calculate the emissivity of the simulated surface geometries, the reflection and transmission are first measured. As can be seen in Figure 5, there are two frequency-domain field power monitors. These monitors, which is the term used in Lumerical, are sensors that measure the power of all incident radiation onto them [28]. One monitor is

above the surface at a distance equivalent to one period of the longest wavelength, 14 microns, which is the guideline stated by the creators of Lumerical to allow all interactions of light with the surface to occur before the radiation reaches the power monitor [29]. This monitor measures all radiation reflected from the surface. The second monitor is placed below the surface of the part to measure any radiation that is transmitted by the structure. With both measurements and Equation 8, the emissivity is calculated for each simulated structure.

### **Parameter Sweep**

Another large benefit of Lumerical FDTD is that it allows the user to easily generate parameter sweeps that run a series of simulations where various aspects of the geometry sweep through a range of values at a predetermined step size. The geometry of the simulations is controlled via a script function which uses input variables determined by the user. All simulations in this study used this software feature to observe emissivity trends.

### **Surface Roughness Analysis**

Previous literature was used as the initial guideline for investigating trends between surface roughness and emissivity.  $R_q$  was the parameter most used in describing surfaces in literature pertaining to surface emissivity [18]. Slope was also suggested as being possibly influential, so  $R\Delta q$ , which is related to surface slope, was another surface roughness parameter of interest [18, 19]. In literature discussing surface roughness in additive manufacturing, ninety percent of literature referenced  $S_a$ , so that parameter will

also be viewed to see if it is indicative of emissivity changes [1]. In addition to these surface parameters, newly calculated surface parameters such as average peak angle, average valley angle, ratio between height and width of surface features, etc. were calculated and compared with emissivity results to observe any possible relationships. A diagram describing these new measurements can be seen in Figure 6. The hope of this overall simulation study is to discover the best existing and/or new surface roughness parameter(s) that relate to emissivity trends.

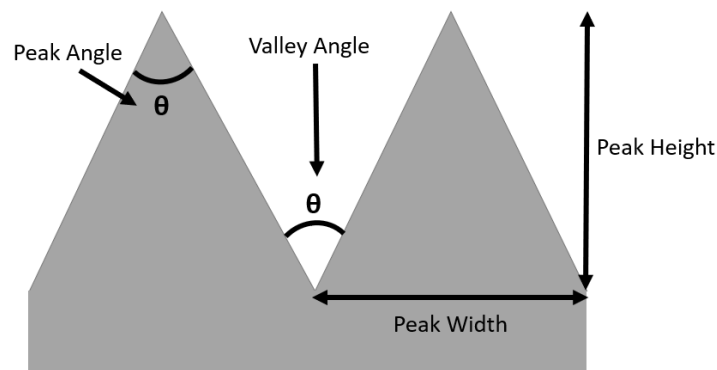


**Figure 6:** New Surface Roughness Measurement Definition Diagram.

## **SIMULATIONS PERFORMED**

### **Isosceles Triangle**

The focus of this initial simulation was to create the fundamental surface roughness geometry to observe the effects on emissivity. The basic geometry also made the calculation of a range of surface parameters simple. The simulation geometry and setup can be seen below in Figure 7. The simulation geometry was an isosceles triangle whose width and height were varied through the parameter sweep function. The values of these variables can be found in Table 2 below. Below the isosceles triangle which

represented the surface roughness was a 5 micron thick rectangle with the same 304 stainless steel properties to represent a part that is sufficiently thick to prevent optical transmission of the wavelengths of interest.

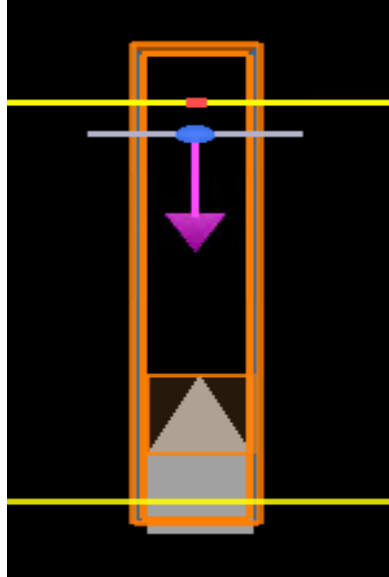


**Figure 7:** Isosceles Triangle Optical Simulation Setup.

**Table 2:** Isosceles Triangle Parameter Sweep Ranges.

Variable	Range	Number of Points	Units
Height of triangle	0-30	31	Microns
Width of triangle	1-30	30	microns

For the given variable ranges, a total of 676 simulations were performed. The measured value of interest for each simulation was the emissivity, which was stored in a three-dimensional matrix, whose dimensions were dictated by the simulation wavelengths and parameter sweep values. Surface roughness parameters were calculated for each simulation geometry and plotted against the emissivity value to observe trends.  $R_a$ ,  $R_q$ ,

and  $R\Delta q$  were the already existing parameters that were focused on for the initial analysis. New surface parameters included valley angle, peak angle, and valley height-width ratio. Some of these plotted trends can be seen below in Figure 8 and Figure 9. These plots demonstrate the high dependence of emissivity on surface roughness changes as the ratio of wavelength to  $R_q$  is greater than one for both of these figures, representing the geometric optical region.

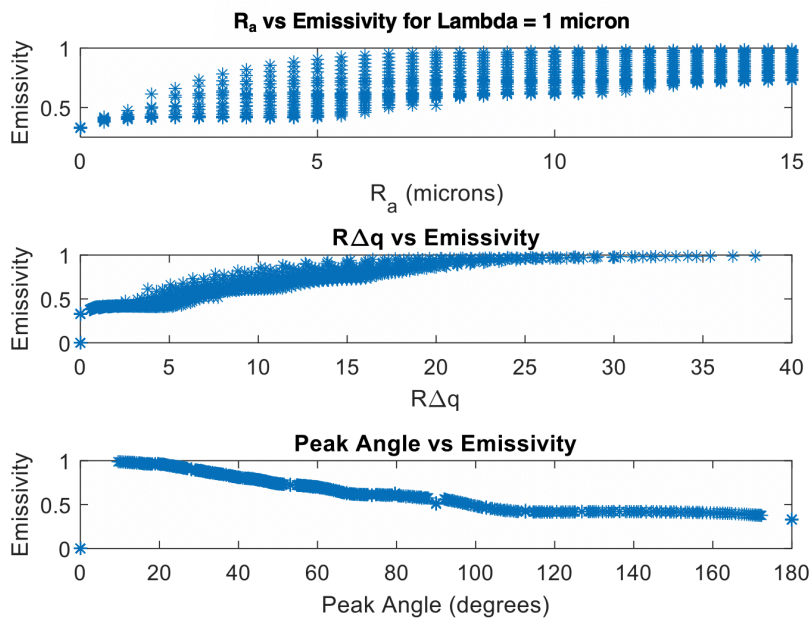


**Figure 8:** Surface Roughness Parameters Plotted Against Emissivity for Observation Wavelength = 1 micron.

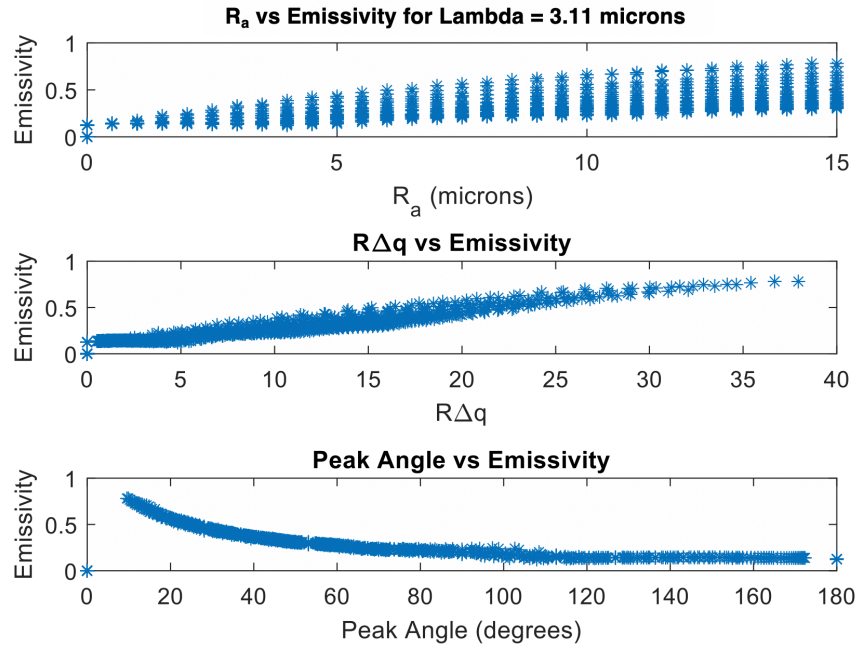


**Figure 9:** Surface Roughness Parameters Plotted Against Emissivity for Observation Wavelength = 3.11 microns.

As can be seen in the  $R_a$  plots, there is a lot of spread in the emissivity value for a given arithmetic surface height value. This result agrees with the statement by Sabuga and Todtenhaupt that the emissivity and  $R_q$ , which is related to  $R_a$ , are not in good agreement [19]. The main source of spread in the data is that for a given  $R_a$ , the surface shape can change drastically, which causes differing emissivity values. The emissivity trends are dictated by internal reflections within the valleys that are created by the surface features. This phenomenon will be explained in further detail in the simulation conclusion section. These internal reflections are not solely controlled by the height of the surface. This translates into a lack of correlation with  $R_a$  which will also be seen in further simulation geometries. Since for this geometry, the valley and peaks were the same size during each simulation, both the valley and peak angles had the best relationship with emissivity

changes. This surface characteristic will be focused on in further simulations to test if it is the best indicator for emissivity changes. A similar simulation study with this particular geometry was conducted in past literature to look at passive radiative cooling in nature. This study looked at the relationship between the geometry of ant hairs and the resultant emissivity. This study also used Lumerical FDTD and found that emissivity increases with triangle size, like the findings with this particular simulation geometry [30].

In addition to observing which surface roughness measurements had stronger correlations, the wavelength dependence of the level of effect that the roughness had on emissivity was observed. When looking at Figure 8 and Figure 9, there is a strong one to one ratio between the valley angle and emissivity. However, when the observation wavelength increases, as in Figure 10 and Figure 11, the relationship between the valley angle and emissivity weakens, due to the fact that the  $R_q$  value of a substantial portion of the simulation geometries produced with the parameter sweep function is significantly lower than the observation wavelength, no longer putting the simulation set fully in the geometric optical region. This can also be seen by the deviation and erratic behavior of the some of the geometries when looking at  $R\Delta q$  and peak angle behavior as seen in Figure 11. When the  $R_q$  to observation wavelength ratio is between 0.1 and 1, there are more factors to consider when predicting emissivity trends [18]. This behavior translates to a higher sensitivity to surface roughness changes in the additive process when observing with shorter wavelengths. In the metallic additive manufacturing processes, where the temperatures are higher, it is more popular to use shorter wavelength thermal

monitoring techniques. Therefore, most of the time, the geometric optical region behavior will be dominant.

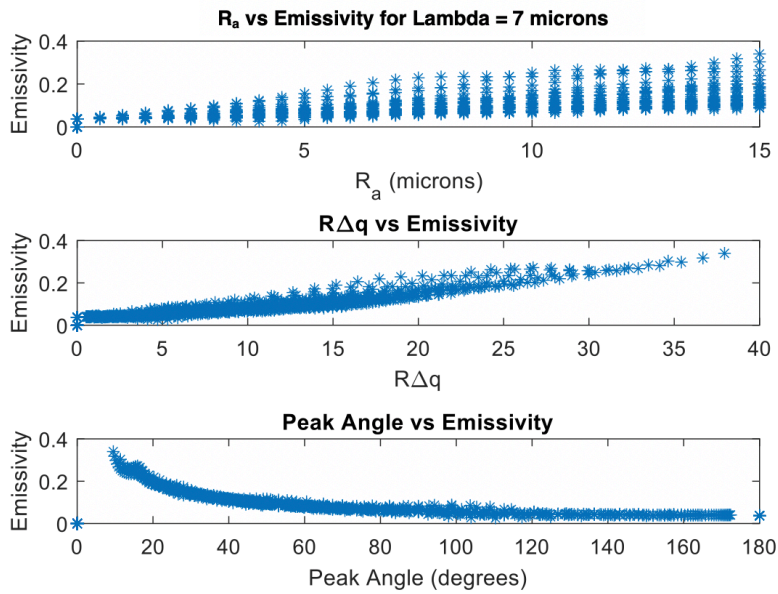


**Figure 10:** Surface Roughness Parameters Plotted Against Emissivity for Observation Wavelength = 7 microns.

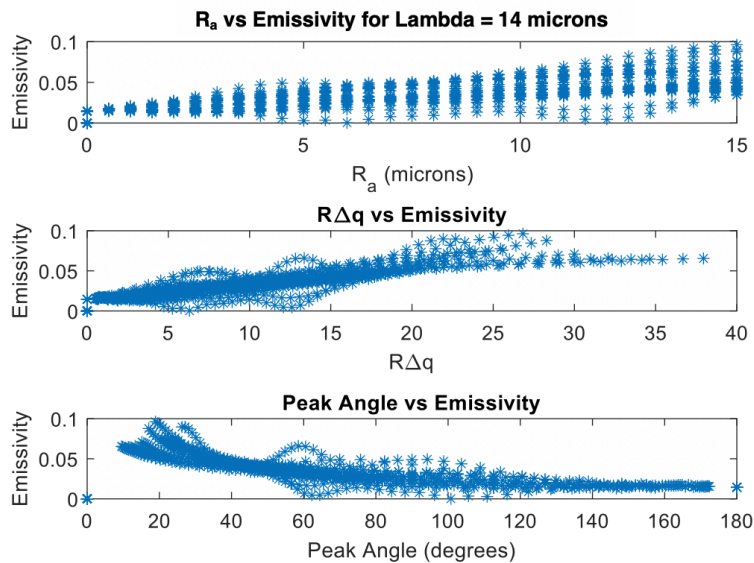


**Figure 11:** Surface Roughness Parameters Plotted Against Emissivity for Observation Wavelength = 14 microns.

### **3D Isosceles Pyramid**

This simulation set was chosen to validate the decision to perform 2D simulations to represent 3D surface geometry. This simulation set was run to demonstrate that the 2D simulations, which were less computationally expensive, produced results that agreed with the 3D simulations, which were a more accurate representation of an actual surface. The overall geometry and setup of the simulation can be seen in Figure 12 below. For this simulation, the boundary conditions were slightly different. Instead of periodic boundary conditions for the X and Y axes, symmetric and anti-symmetric boundaries were used to reduce the simulation space by a factor of four. As can be seen in Figure 13 below, the gray quadrant of the simulation space is the quadrant where the simulation is run, whereas the colored quadrants represent the assumption that the magnetic fields and electric fields are symmetric about the X and Y axes. This assumption allows the simulation space to become a quarter of what it was originally, saving memory and computational time to run each simulation. In addition to this computational shortcut, the mesh style used in this simulation was set to staircase to further reduce the simulation time. This mesh style is the simplest option in the Lumerical FDTD options and therefore was chosen to reduce memory for meshing and running the simulations. The parameter sweep variables for this simulation were the same for the 2D isosceles triangle simulation set: peak width and peak height. The values of the variables can be found in Table 3 below. Since these simulations take significantly longer to run than the 2D versions, not all values in the range were used in the parameter sweep. Instead, equally spaced points were used within the given ranges below.

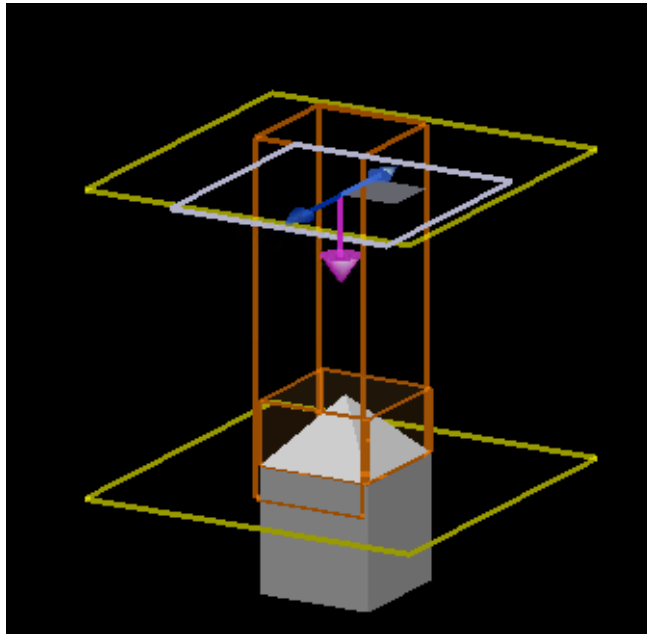


**Figure 12:** 3D Pyramid Simulation Setup.

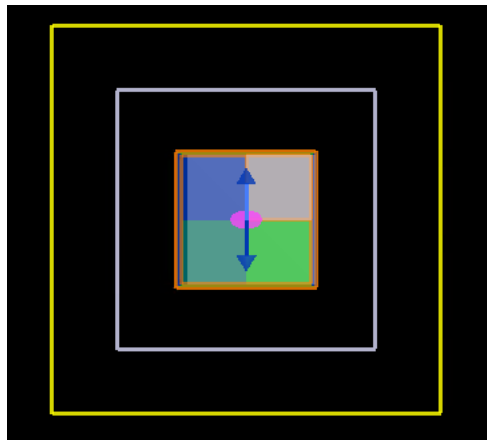


**Figure 13:** Top Down View of Reduced Simulation Space with Symmetry Boundary Conditions.

**Table 3:** 3D Pyramid Parameter Sweep Ranges.

<b>Variable</b>	<b>Range</b>	<b>Number of Points</b>	<b>Units</b>
Peak Height	5-30	6	Microns
Peak Width	5-30	6	Microns

The results of this simulation are compared with the 2D simulation to see if the emissivity measurements and trends match. As can be seen for the 1 micron measurement wavelength in Figure 8 and Figure 14, the general emissivity trends are similar for the 2D and 3D representation of the same geometry. Even for the longer wavelength of 14 microns, as seen in Figure 11 and Figure 15, the emissivity trends still match closely. Therefore, it was decided to perform only 2D simulations to look at the possible surface geometries going forward.

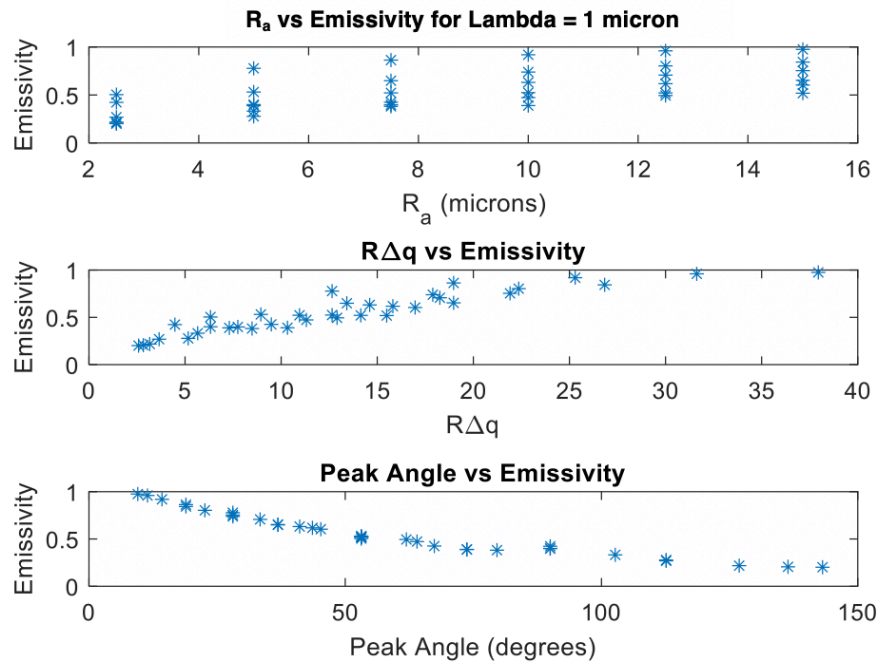


**Figure 14:** Surface Roughness Parameters Plotted Against Emissivity for Observation Wavelength = 1 micron for 3D Pyramid Simulation.

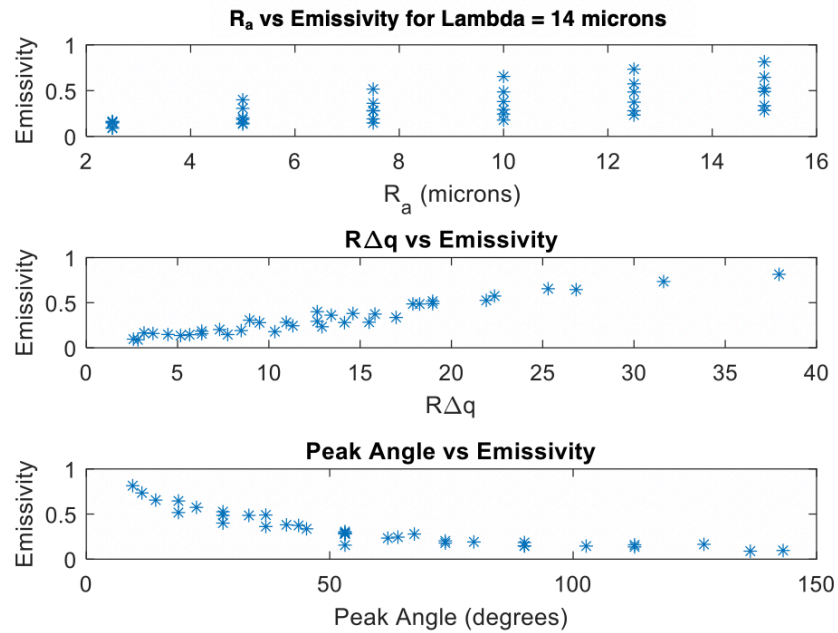


**Figure 15:** Surface Roughness Parameters Plotted Against Emissivity for Observation Wavelength = 14 microns for 3D Pyramid Simulation.

### Parabolic Valley

This simulation was performed to observe the effects of the valley geometry when the valley is not represented by an ideal triangle. The parabolic shape more aptly represents real surface profile geometry. The simulation geometry can be seen in Figure 16. However, this geometry creates more complex geometry calculations, making exploration of the ideal surface parameter to describe emissivity changes more arduous. Therefore, this simulation was performed to compare the relationships between the surface roughness parameters and emissivity to those found in the 2D isosceles triangle simulation. If the relationships are similar between this parabolic valley simulation and the isosceles triangle simulation, then the triangular shape will continue to be used for future simulations for ease of calculations. Like the 2D isosceles triangle simulation, the

parameter sweep variables were valley width and valley height whose values can be found in Table 4.

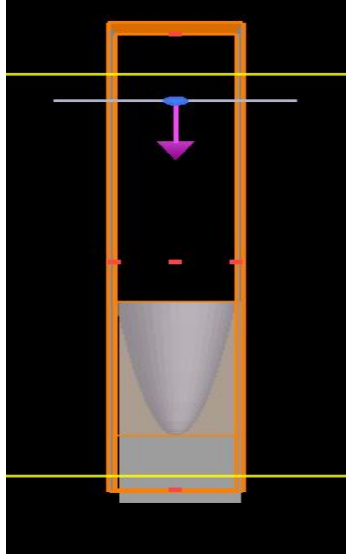


**Figure 16:** Parabolic Valley Optical Simulation Setup.

**Table 4:** Parabolic Valley Parameter Sweep Ranges.

<b>Variable</b>	<b>Range</b>	<b>Number of Points</b>	<b>Units</b>
Height of parabolic valley	0-30	31	Microns
Width of parabolic valley	1-30	30	Microns

As seen in Figure 17 and Figure 18 below, the relationship between emissivity and some of the common surface roughness parameters demonstrate similar trends, but do not follow the triangular simulation exactly, most likely due to the lessening of internal reflections due to the curved slopes of the valley surface.

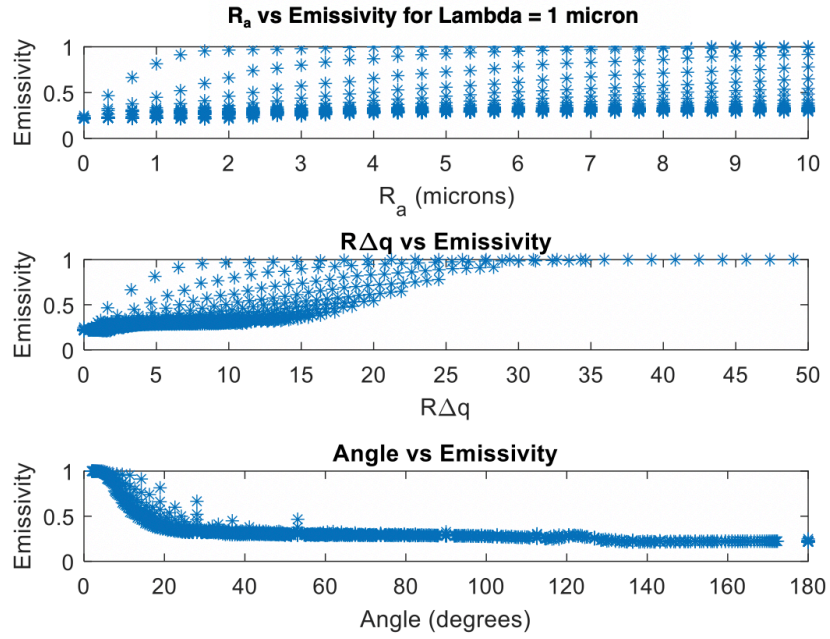


**Figure 17:** Parabolic Valley Simulation - Surface Roughness Parameters Plotted Against Emissivity for Observation Wavelength = 1 micron.

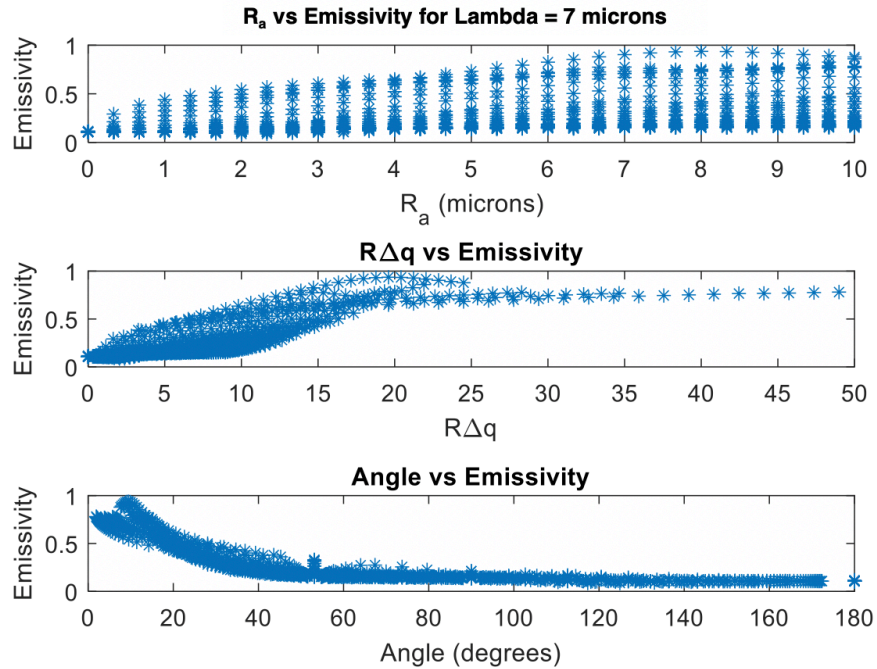


**Figure 18:** Parabolic Valley Simulation - Surface Roughness Parameters Plotted Against Emissivity for Observation Wavelength = 7 microns.

A snapshot of the internal reflections of this simulation compared to the triangular simulation can be seen in Figure 19 below. In this figure, red represents the largest amount of optical power, while green and light blue represent the least amount of optical power for each respective simulation. It is clearly seen that the internal reflection behavior differs between the simulation geometries, causing differences in measured emissivity for similar geometric dimensions. However, the level of difference in overall emissivity trends between the two simulation geometries is believed to be insufficient to allow for the ideal case of the triangle to be used to model surface features in future simulations.

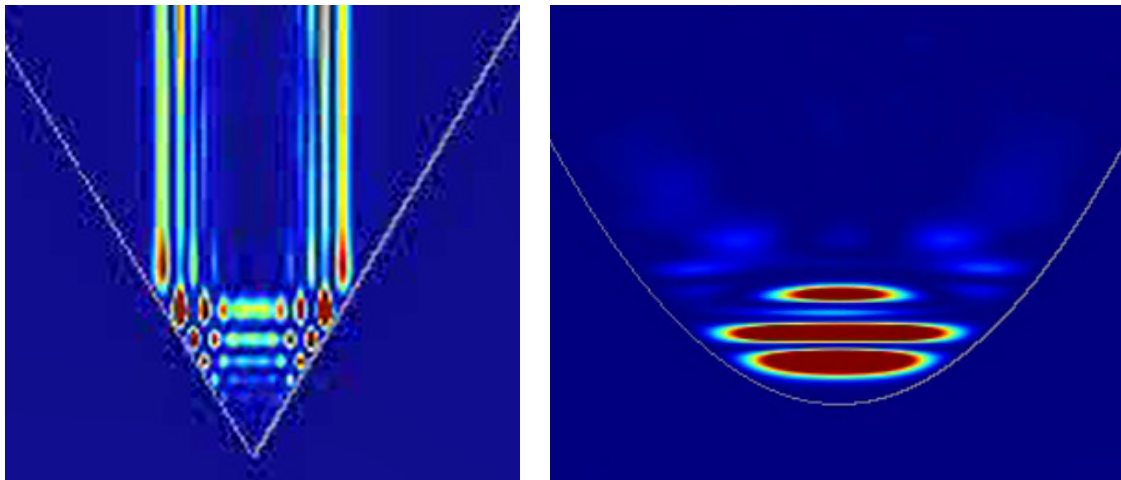


**Figure 19:** (LEFT) Internal Reflections for Isosceles Triangle Simulation (RIGHT) Internal Reflection for Parabolic Valley Simulation.

### **Flat Valley**

The focus of this simulation set was to discover the effects of the width of the valley since the valley angle was found to be the best indication of emissivity changes in the isosceles triangle simulation above. An image of the representative simulation geometry can be seen in Figure 20 below. For the parameter sweep, the variables were

the valley width as measured at the bottom and the peak height (both peaks were the same height). The width of the peaks was held constant at 15 microns. The variable ranges can be found in Table 5 below.

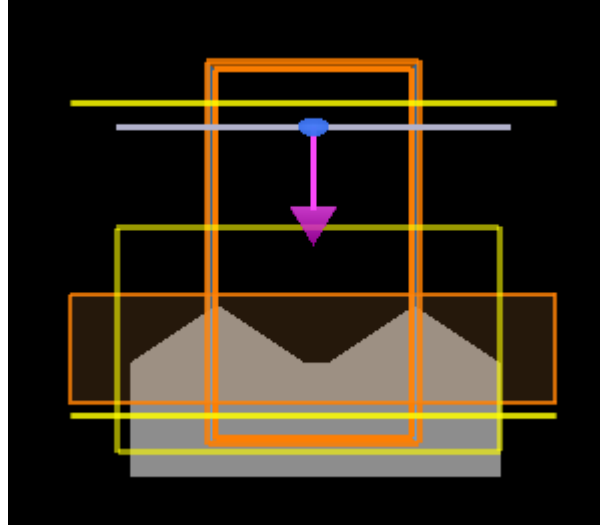


**Figure 20:** Flat Valley Optical Simulation Setup.

**Table 5:** Flat Valley Parameter Sweep Variable Ranges.

<b>Variable</b>	<b>Range</b>	<b>Number of Points</b>	<b>Units</b>
Width of valley	0-15	16	Microns
Height of peaks	5-30	26	Microns

Once again emissivity was measured for each simulation iteration. The focus of the analysis was the effect of the valley width on the resultant emissivity. It was determined from the isosceles simulation above that an increase in peak height should increase the emissivity since the valley height increases as peak height increases. A 3D plot with peak height, valley width, and emissivity can be seen in Figure 21, Figure 22, and Figure 23 below.

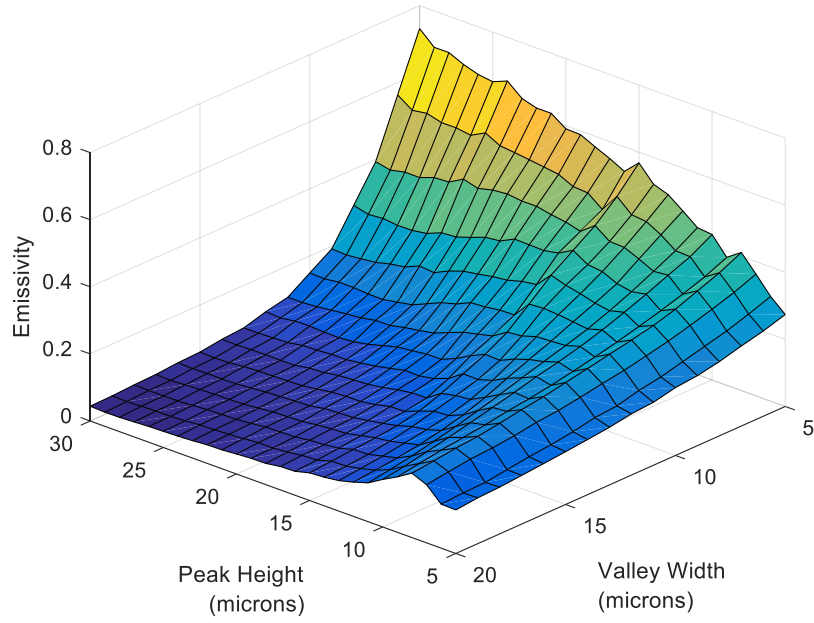


**Figure 21:** Surface Plot Describing Emissivity Dependence on Valley Width and Peak Height for Observation Wavelength = 1 micron.

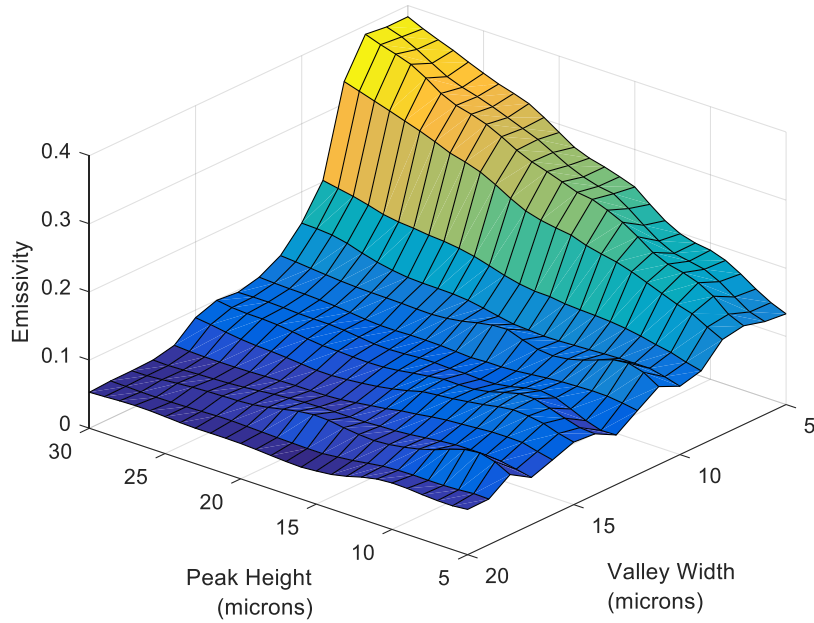


**Figure 22:** Surface Plot Describing Emissivity Dependence on Valley Width and Peak Height for Observation Wavelength = 7 microns.

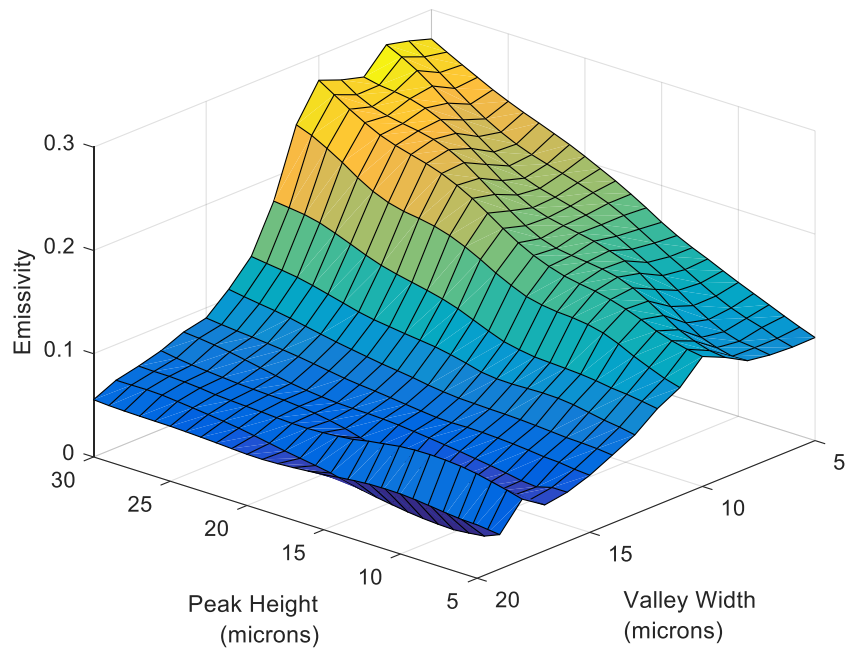


**Figure 23:** Surface Plot Describing Emissivity Dependence on Valley Width and Peak Height for Observation Wavelength = 14 microns.

In each figure, below a certain threshold of valley width, whose value is about the observation wavelength, peak height has little to no effect on the emissivity value. For example, the emissivity drastically increases as the valley width approaches five microns when the observation wavelength is 1 micron, as in Figure 21. However, the emissivity remains elevated for a large range of valley widths when the observation wavelength is 14 microns, as in Figure 23. This demonstrates that internal reflections in a narrow valley relative to the observation wavelength are the influencing factor of the highly rough surfaces relative to the wavelength of interest. As seen in the figures above, for the structure to influence the emissivity, the scale of the valleys needs to be on the same or smaller scale than the wavelength for it to have any effect.

## Skewed Triangles

This simulation set was performed to create different peak and valley dimensions within a single overall geometry. This geometry was chosen as the peak angle and valley angle differed except when the peak apex was centered and then the simulation would resemble the isosceles triangle simulation. The initial geometry for this simulation set can be seen in Figure 24 below. The parameter sweep variables for this simulation were the peak height and peak apex location. A diagram showing how the peak apex location was defined can be found in Figure 25. The peak apex location is zero at the center line of the simulation space. The values for the simulation variables can be seen in Table 6.

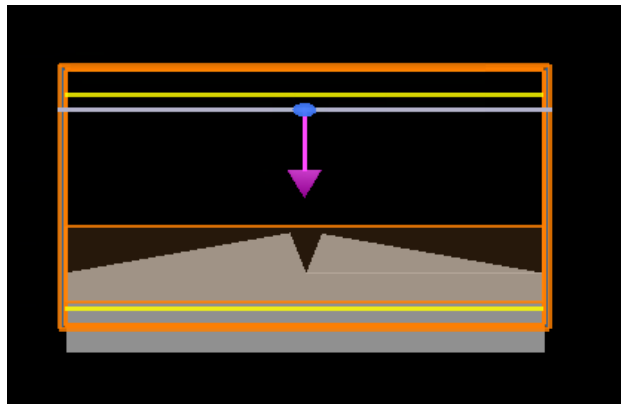


**Figure 24:** Symmetric Skewed Triangles Optical Simulation Setup.

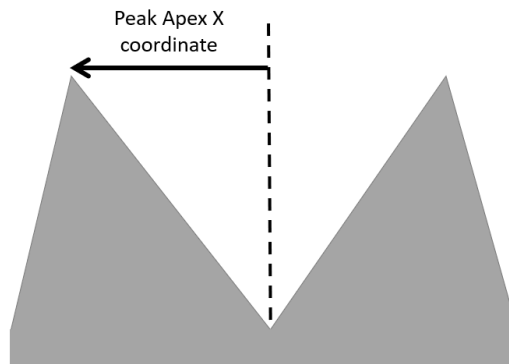


**Figure 25:** Peak Apex Coordinate Definition Diagram.

**Table 6:** Symmetric Skewed Triangles Parameter Sweep Variable Ranges.

Variable	Range	Number of Points	Units
Height of Peak	0-30	31	Microns
Peak Apex Location	0-30	31	Microns

In running the parameter sweep, it was found that although the values of the peak and valley angles were different, they were tied to each other, thereby preventing the ability to decouple their behavior with this particular simulation geometry. The tied behavior can be seen below in a weighted plot of both the peak and valley angles Figure 26. The weighted value is the angle multiplied by the measurement wavelength.

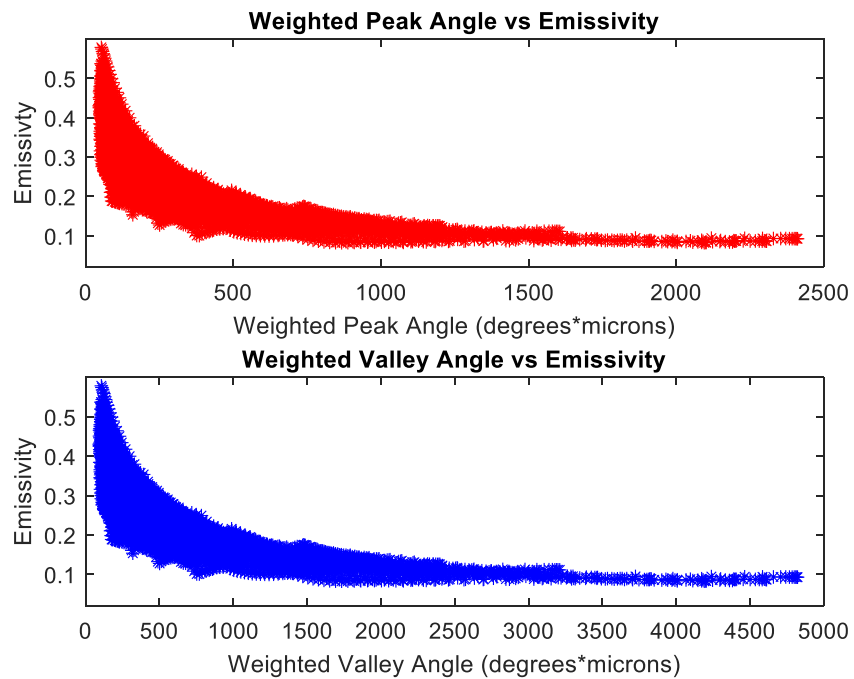


**Figure 26:** (TOP) Peak Angle Normalized with Observation Wavelength Plotted Against Emissivity (BOTTOM) Valley Angle Normalized with Observation Angle Plotted Against Emissivity.

Therefore, a new simulation geometry was chosen to separate the valley and peak angle trends from each other. In this simulation with the addition of a third triangle whose peak angle did not change at the same rate that the other two skewed peak angles did. As can be seen in Table 7 below, the height of the peaks as well as the angle of the left two peaks as seen in Figure 27 below were controlled in the parameter sweep. Once again, the two peak apex locations were defined from the symmetry line as seen in Figure 25. The height of the right peak as seen in Figure 27 was five microns taller than the height variable of the left two as dictated by the height variable in the parameter sweep.

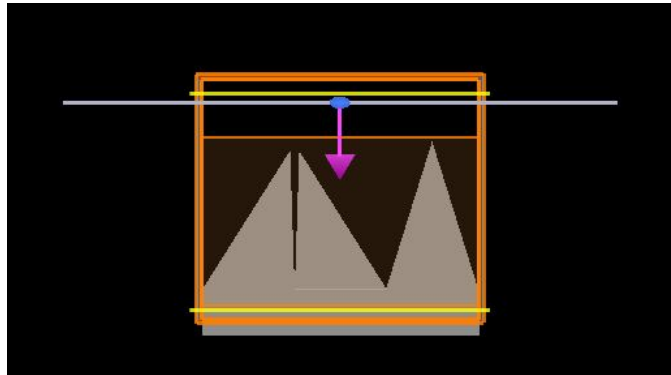


**Figure 27:** Three Peak Skewed Triangle Simulation Geometry.

**Table 7:** Three Peak Skewed Triangle Parameter Sweep Variable Ranges.

<b>Variable</b>	<b>Range</b>	<b>Number of Points</b>	<b>Units</b>
Peak Height	5-30	26	Microns
Peak Apex Location	0-30	31	Microns

As can be seen in Figure 28 and Figure 29 below, there were still similar trends with the peak and valley angles. However, the valley angle had a tighter vertical spread, meaning

it had a better relationship with emissivity than the peak angle. As will be discussed in further detail in the simulation conclusion section, the valley angle is the driving force behind the emissivity trends.

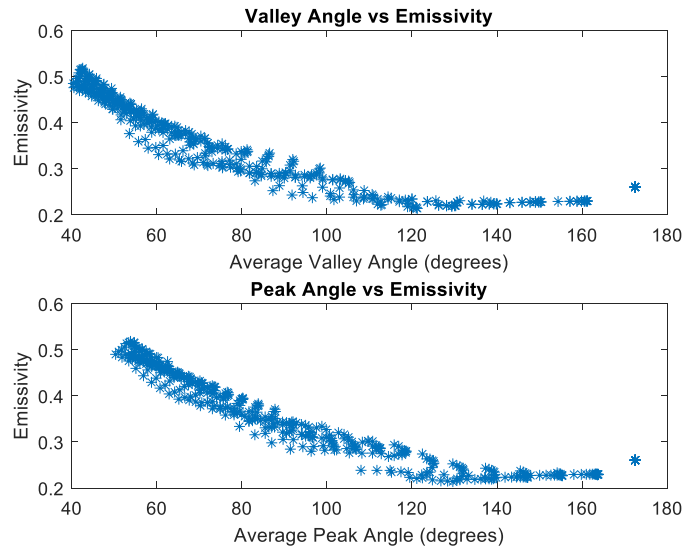


**Figure 28:** Surface Roughness Parameters Plotted Against Emissivity for Three Peak Skewed Triangles with Observation Wavelength = 1 micron.

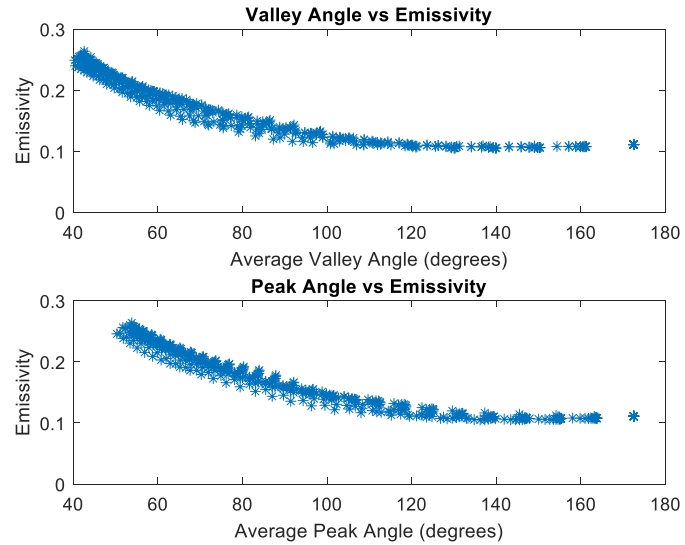


**Figure 29:** Surface Roughness Parameters Plotted Against Emissivity for Three Peak Skewed Triangles with Observation Wavelength = 7 microns.

### Variable Sized Peaks

This simulation was performed to investigate the possibility of different length scales of surface features and their effects on emissivity. The main focus of this simulation was to see if the average valley angle remained the key surface parameter to watch, or if the multi-scale structure required a different approach to predict emissivity behavior. Two different sets of simulations were performed. The sets had similar geometry with two peaks, one large and one small, as can be seen in Figure 30.

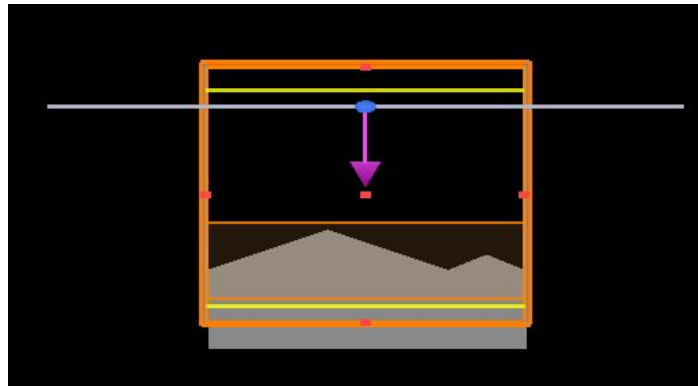


**Figure 30:** Variable Sized Peaks Simulation Geometry.

The first simulation set run used the parameter sweep to change the heights of the two peaks. The dimension and variable values can be found in Table 8. The second simulation set that was run used the parameter sweep to change the width of the peaks. The dimensional and variable values can be found in Table 9 below.

**Table 8:** Variable Sized Peaks - Height Change Parameter Sweep Values.

Variable	Range / Value	Number of Points	Units
Large Triangle Width	30	1	Microns
Small Triangle Width	10	1	Microns
Large Triangle Height	5-30	26	Microns
Small Triangle Height	5-30	26	Microns

**Table 9:** Variable Sized Peaks - Width Change Parameter Sweep Values.

Variable	Range / Value	Number of Points	Units
Large Triangle Height	30	1	Microns
Small Triangle Height	10	1	Microns
Large Triangle Width	5-30	26	Microns
Small Triangle Width	5-30	26	Microns

As can be seen in Figure 31 and Figure 32 below, the main aspect of the surface that affects the emissivity behavior is still the valley angle. As can be seen in Figure 32 where only the width of the peaks was changed, the  $R_a$  value remained the same for all 676 simulations even though the shape was changed drastically. The peak width change set is the clearest example that  $R_a$  is insufficient for describing emissivity changes when in the geometric optical region.

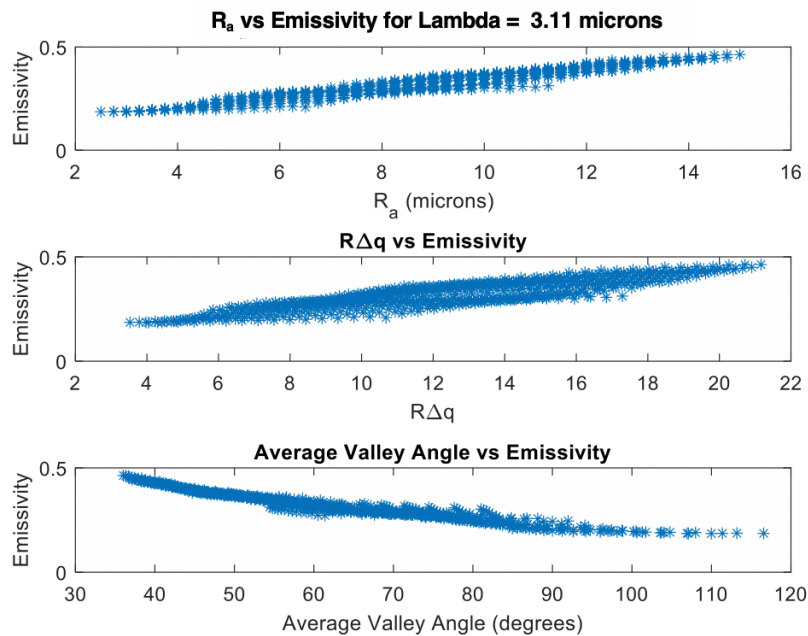


**Figure 31:** Surface Roughness Parameters Plotted Against Emissivity for Multi-Scale Peak Simulation - Height Change with Observation Wavelength = 3.11 microns.

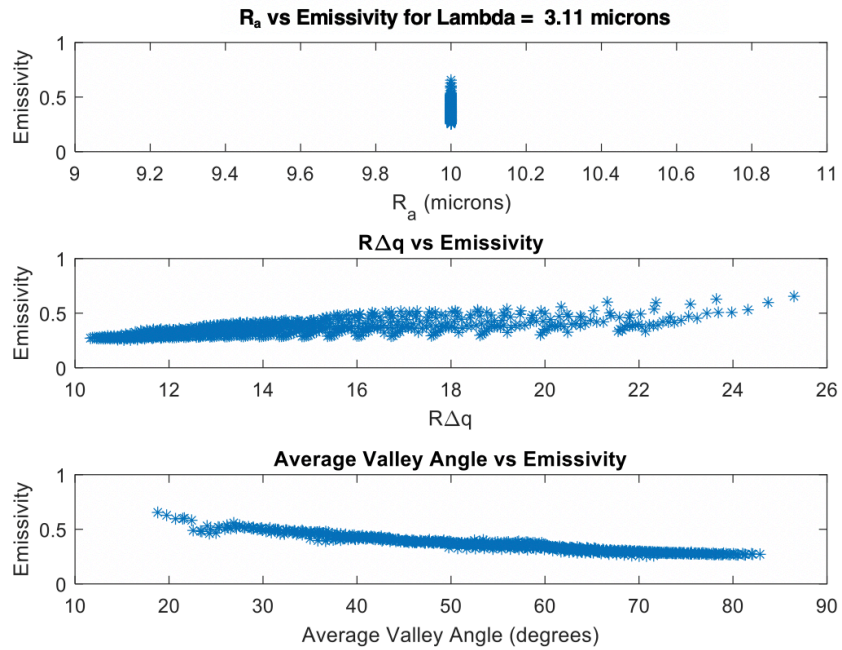


**Figure 32:** Surface Roughness Parameters Plotted Against Emissivity for Multi-Scale Peak Simulation - Width Change with Observation Wavelength = 3.11 microns.

In addition to investigating which surface roughness parameters were key, further analysis was performed to see if the larger scale structures influenced the emissivity more than the smaller scale structures, or if the structure as a whole was to be considered. In Figure 33, the larger peak was held constant at 5 microns tall while the smaller peak's height was swept through 5-30 microns. In comparison, in Figure 34, the larger peak's height was held constant at 30 microns tall while the smaller peak's height was swept through the previous range.

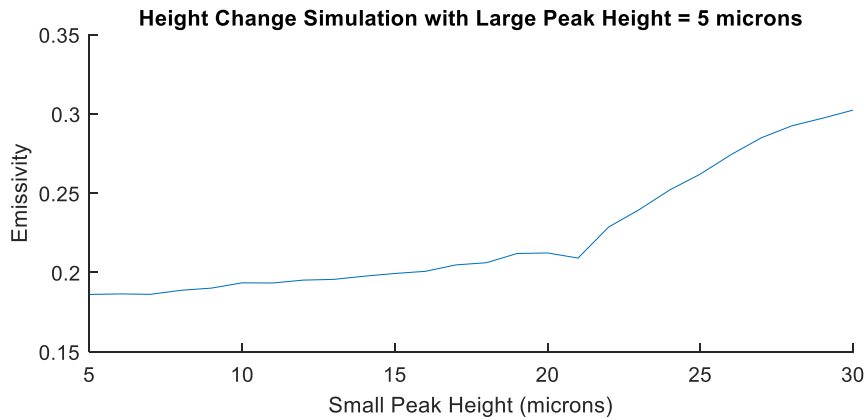


**Figure 33:** Multi-Scale Simulation - Small Peak Height Influence on Emissivity with Large Peak Height = 5 microns.

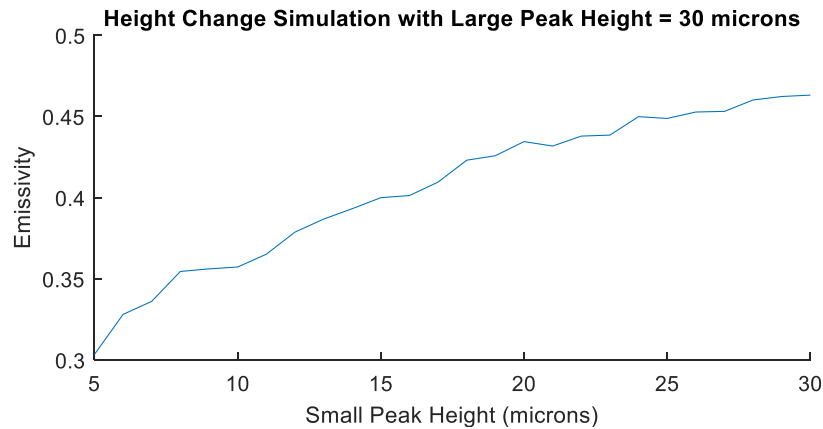


**Figure 34:** Multi-Scale Simulation - Small Peak Height Influence on Emissivity with Large Peak Height = 30 microns.

Even though the height of the larger peak is drastically different between the two situations, the total effect on emissivity is nearly the same, demonstrating that it is not the size of the feature, but the slope or angle of the feature that is key. This result is also seen in Yang and Buckius, where it was found that the largest sloped surface feature dominated the emissivity behavior even if the surface feature was smaller in overall size than other surface features with lower slopes [31].

## OVERALL SIMULATION RESULTS

There are several overall trends that were found throughout all simulation geometries. The slope of the surfaces had a stronger relationship with emissivity than the overall size of the features, which was seen in the plots as  $R\Delta q$  having a stronger relationship to emissivity than  $R_a$ . Also seen was that the angle of the valleys had the strongest effect on emissivity. This trend can be explained with the Mendenhall wedge effect. As a valley becomes narrower, decreasing the valley angle, it causes the “incident radiation to undergo more reflections, and hence more absorption, and hence approaching more and more closely what is called a ‘blackbody’” [5]. This behavior has been used for over a century to create near-blackbodies for experimental purposes. Charles Mendenhall calculated that the reflection of a wedge-like cavity was exponentially dependent on the angle of the cavity in the ideal case that there is no optical transmission present [32]. The equation he used to estimate emissivity of the cavity can be found in Equation 9 below [32]. The reflection power of the surface is always less than one, so as the angle decreases, absorption, and therefore emissivity increases.

$$E \approx A = 1 - r^{\frac{180}{\theta}} \quad (9)$$

E = emissivity

A = Absorption

r = reflection power of the material surface

$\theta$  = internal wedge angle

In addition to discovering what aspect of the surface topography had the greatest influence on emissivity, it was observed that the ratio of the surface roughness to the measurement wavelength was key to determining the degree of influence. As was discussed in the introduction, there are three optical regions. The main one of focus, the geometric optical region, is where the ratio of surface roughness to measurement wavelength exceeds one. As can be seen in Figure 8-11, as the wavelength decreases, the range of emissivity values for the same range of surface roughness values is significantly larger. This behavior is important to consider when selecting an instrument for thermal monitoring in AM processes. The non-contact instruments such as SWIR cameras are more sensitive to surface roughness changes than the MWIR and LWIR cameras.

## **Experimental Surface Roughness and Emissivity Correlation**

Following the simulation work, the next step was testing and validating the simulation findings using experimental measurements. For this experimental side of the surface characteristic determination, metal parts were produced using the DMLS process. Specifically, a ProX 200 was used with a range of build parameters to produce a range of surface textures. To reiterate, 316 stainless steel is the chosen material for these parts as it is a common material in the traditional manufacturing as well as additive manufacturing. The part design was a square with sufficient thickness so as to prevent transmission of any measurement wavelength. Once the parts were manufactured, their surfaces were measured. The method for measuring the surfaces was determined based on how accurate it can measure the rough and highly reflective parts and the ability to save raw data for manipulation. Through the literature review, it was determined that some optical measurement techniques are not suitable for these AM parts as they are too reflective and cause inaccurate readings. Some methods that were investigated will be X-ray coherence tomography (XCT), contact profilometry, and confocal microscopy.

After the surfaces were measured, the spectral emissivity of each part was measured using a Hemispherical Directional Reflectometer (HDR) coupled with a Fourier Transform Infrared (FTIR) spectrometer. These instruments allowed for directional reflectance and total hemispherical emissivity to be measured. The raw surface data was then analyzed in conjunction with the emissivity results to define the characteristic that affects the measured emissivity. As the calculation of traditional surface parameters is widely known, the goal of this dissertation is to provide a way to

calculate a new surface parameter (or combination of surface parameters) that reflects the physical topographic characteristics of the surface that affects emissivity.

### **SAMPLE FABRICATION**

A ProX 200 machine by 3D systems was used to produce the samples. This system has a build area of 140x140x100 mm [33]. The sample geometry was determined by the restrictions of the equipment that would be used to measure surface topography and emissivity. The final geometry was determined to be a 25 mm square that was 5 mm thick. Previous studies investigating surface roughness effects on emissivity had samples that ranged in thickness between 3-12 mm [18, 19]. The main concern about the thickness of the samples was to have stiff parts that would not be easily bent to keep as level a surface as possible, but not excessively thick, as it would waste material and cause the builds to take longer than necessary. As stated previously, the material used for all samples is 316 stainless steel as it is both a common conventional and additive manufacturing material used. Exemplar samples can be seen in the Figure 35 below.

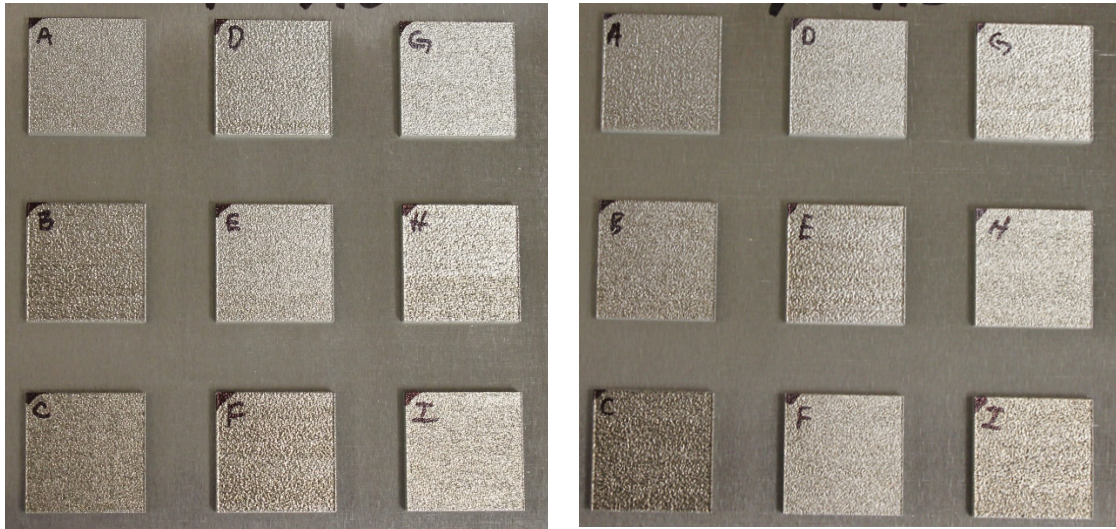


**Figure 35:** As-Built 316 Stainless Steel Samples on Build Plate.

To demonstrate the range of surfaces produced by the direct metal laser sintering process, a range of process parameters was used to produce the samples. The key value in the DMLS process that many researchers control to change the quality of parts is the energy density input into powder bed. The equation for applied energy density is seen below in Equation 10 [34].

$$E_A = \frac{\text{Laser Power}}{\text{Scan Velocity} \times \text{Scan Spacing}} \quad (10)$$

There are three process parameters that affect energy density: laser power, scan speed, and hatch spacing. Although only one parameter change is needed to affect the energy density, two variables were altered throughout the building process to affect the other mechanisms at play that affect surface topography, density, and mechanical strength such as heat transfer and fluid dynamics seen in the melt pool. As was stated in introduction section, the generation of surface roughness is directly related to both laser power and scan speed.

A customary practice in preparing a new machine to produce parts is performing test builds for the optimization of the build parameters to achieve the best strength, density, surface roughness, or other mechanical properties that are of interest to the customer. For the ProX 200, the laser power range available is 0-265 W and the scan speeds available are 10-2800 mm/s. For a concurrent but non-related study, test parts were built with a combination of laser powers and scan speeds in the ranges stated above [35]. Most of the samples were produced using ProX 200 powder with a Gaussian distribution with a mean particle size around 15 microns. Two builds were produced using the 316 stainless steel ProX 320 powder, whose size had a Gaussian distribution with a mean around 25 microns. Due to the large use of the ProX 200 powder, the ProX 320 powder was the only available option for the creation of the samples for this emissivity study. The test parts for the process optimization were in the form of two centimeter cubes to allow for density and surface roughness, both on top and the sides, to be measured. They were built with a combination of laser powers and scan speeds to study the relationship both density and surface roughness had with the energy density of the process. All cubes were built with 30 micron layer thickness with the exception of one build with the ProX 320 powder, which had a 40 micron layer thickness. For certain combinations of parameters, the cubes were not completed due to a lack of fusion or extremely rough surfaces that did not allow the recoater blade of the machine to proceed in placing an even layer of powder down. These combinations had either too low or too high energy density. For example, very slow scan speeds with high laser power produced parts that were too rough for the process to continue. Therefore, the data presented is only

the subset of parameters that allowed the cubes to be fully built. The surface roughness of the cubes was measured using a Keyence VR3100 optical microscope that is designed to measure surface roughness using a non-contact optical method.

Since the purpose of this study is to ascertain a new parameter in describing the surface topography that better relates to emissivity changes, choosing an already existing surface roughness parameter that would be used to decide which build settings would be best suited to make a range of samples was difficult. Areal surface roughness measurements were used to gain an overall perspective of the surfaces for ease of data visualization. From the literature review, it was suggested and confirmed with the optical simulations in this study that the slope of the peaks and valleys that comprise the surface had a good relationship to the emissivity changes of the varying surfaces. The slope is not enough to completely describe emissivity changes but was sufficient at this stage for selecting build settings to generate a range of samples. Therefore, an already existing surface roughness parameter that relates to the slope,  $S\Delta q$ , was used as the determining factor for the selection of builds settings. This surface roughness parameter has been used to delineate different AM surfaces from each other when  $S_a$  was insufficient, such as in Grimm et. al. [36]. For  $S\Delta q$ , the higher the value, the steeper the slope of the peaks and valleys that compose the surface. The graph seen in Figure 36 below demonstrates the relationship between energy density and  $S\Delta q$  as observed from data that was generated through the separate study mentioned above [35].

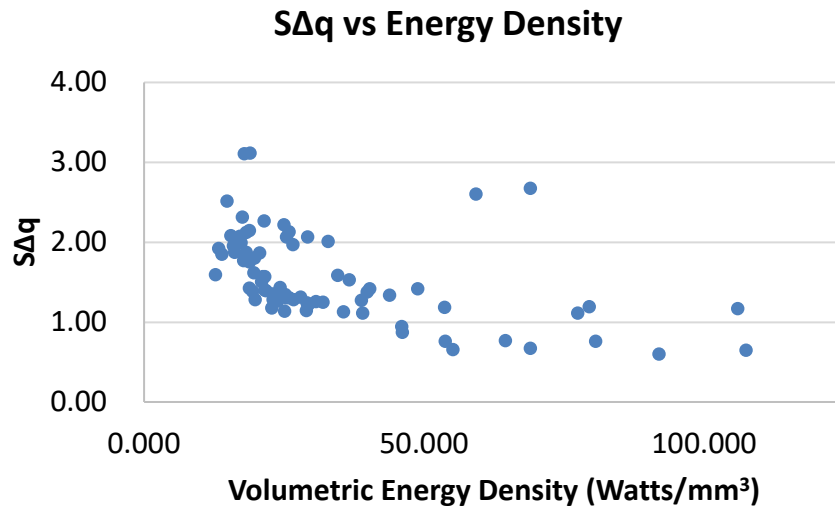


**Figure 36:** Density Cube Study - SΔq as a Function of Volumetric Energy Density.

Since for some volumetric energy density values, a range of SΔq values were produced, a process map that looked at laser power and scan velocity and the resultant SΔq was created to better enable the selection of a range of SΔq. This process map can be seen below in Figure 37. For this process map, the size of the circle and value inside the circle represents the SΔq value for that given laser power and scan speed combination. This process map represents all the builds that were performed with the ProX 200 powder with a mean around 15 microns. A second process map seen in Figure 38 was created to observe the effects of the process parameters on parts that were fabricated with the ProX 320 powder with a mean around 25 microns.



### SΔq for 30 Micron Layer Thickness Density Cubes

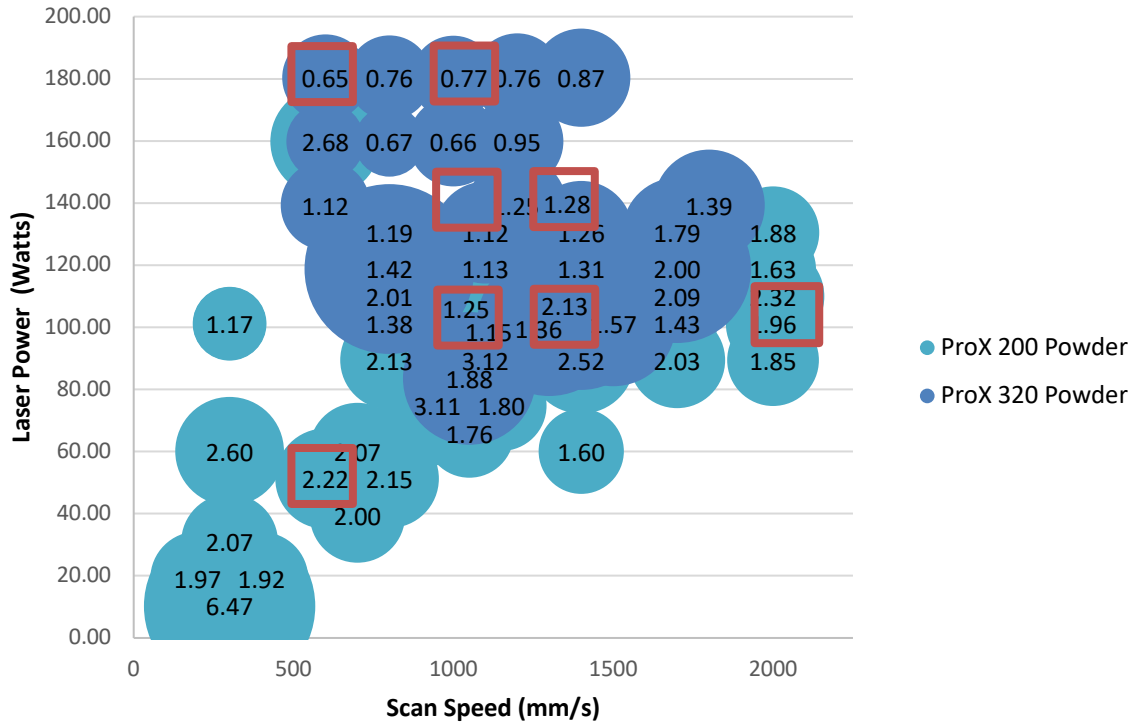


**Figure 39:** Build Setting Locations Superimposed on SΔq Process Map.

For the choice of build settings, combinations that were well spaced values within the acceptable process setting domain and had variable SΔq values were chosen. When choosing these sets, pairs of settings with either identical laser power or scan velocity were chosen to observe the effects of either setting on surface roughness. A diagram that shows where the final pairings were located on the process map and what values of SΔq they had can be found in Figure 39. At least one pair of settings with identical energy densities were chosen with varying power and scan velocity to see if energy density was a good indicator of surface roughness. In total, eight build setting combinations were

chosen which can be seen in Table 10 below. In addition to the variable build settings, the remainder of the build settings which were held constant can be found in Table 11.

**Table 10:** Variable Sample Build Parameter Combinations.

<b>Set</b>	<b>Parameter</b>	<b>Laser Power</b>	<b>Scan Velocity</b>
1	A	180 W	600 mm/s
1	B	50 W	600 mm/s
2	A	180 W	1000 mm/s
2	B	100 W	1000 mm/s
3	A	100 W	1400 mm/s
3	B	100 W	2000 mm/s
4	A	140 W	1000 mm/s
4	B	140 W	1400 mm/s

**Table 11:** Constant Sample Build Parameters.

<b>Scan Strategy</b>	<b>Layer Thickness</b>	<b>Hatch Spacing</b>	<b>Laser Spot Size</b>
0/90	30 microns	50 microns	100 microns

As stated in the introduction section, additive manufacturing has a great deal of variability in the process. Both build to build and within build, position dependent variabilities are present. Therefore, to observe the issue that the emissivity of surfaces which are generated in the process are dynamic throughout a build or between builds and need to be accounted for when performing in-situ non-contact thermal monitoring, a specific build plan was devised. The build setup can be seen in the diagram in Figure 40 below. As stated above the sample dimensions were 25x25x5 mm due to the restrictions of measurement instruments that would be used in successive steps in the study.

Therefore, a 3x3 grid of parts was fabricated in each build due to the limitations of the build envelope. The build setting combinations were paired off and were used in conjunction during two successive builds. For each build, roughly half of the parts were

fabricated with one setting combination, while the other half used the other setting combination. This allowed for both forms of part variability to be studied. A diagram showing how a pair of builds was laid out, with “A” and “B” referring to the parameter letter in Table 10. Once all samples were built, the samples were labeled with letters prior to being cut off using electrical discharge machining (EDM). Samples were labeled A-I which can be seen in Figure 41. In later sections, the locations may be referred to as positions 1-9.

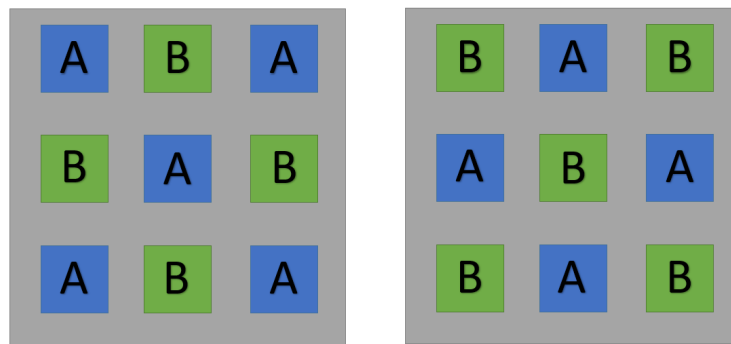


**Figure 40:** Build Plan for Pair of Laser Parameter Combination Builds.

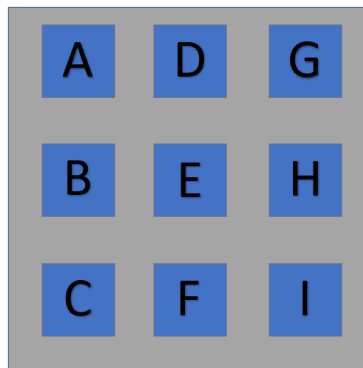


**Figure 41:** Sample Position Labeling Scheme.

## **SURFACE ROUGHNESS MEASUREMENT**

Once all samples were fabricated, the surface roughness was measured. For the purposes of this study, which are investigating possible new surface parameters, the raw height data of the surfaces needed to be acquired. The surface measurement techniques that were considered for this task included contact profilometry, white light interferometry, X-ray coherence tomography (XCT), confocal microscopy, focus variation microscopy, and fringe pattern projection microscopy.

There are two issues with measuring the surface roughness of metallic additively manufactured parts. The first is the highly reflective nature of the parts, which interferes with some of the non-contact techniques used to measure surface roughness. The second issue is the highly rough and irregular nature of the surfaces produced, which can affect both non-contact and contact techniques. These issues prevent confocal microscopy, focus variation microscopy, and white light interferometry from being used to measure the surfaces accurately [1]. While contact profilometry is one of the most common methods for surface roughness characterization, the irregular surfaces of AM parts pose a risk for possible damage to the measurement stylus and aliasing. While X-ray coherence tomography is a widely used technique for defect detection within additively manufactured parts, due to its resolution limits dictated by the study's specific sample geometry and surface detection issues, it is not suitable for this study. In addition to this issue, the resultant data from XCT images along the surface are gray scale, so accurate determination of surface features is difficult and could cause incorrect surface height data. Therefore, the most suitable method for this study is fringe pattern projection

microscopy. This method projects fringe patterns with variable frequency and position onto the sample. Using a CMOS sensor which detects the fringe pattern distortions and computer algorithms, it calculates the surface heights of an area of interest. A diagram of this function can be seen in Figure 42 below. The specific measurement device used was a Keyence VR3100 visual microscope.

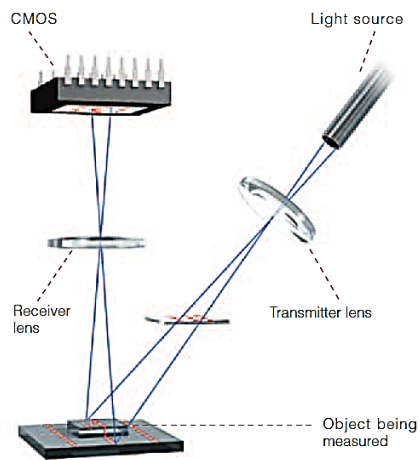


**Figure 42:** Keyence VR3100 Visual Macroscope Functional Diagram [37].

The dimensions of the area that is measured depends on the focus selected at the time of measurement. At the lowest magnification, 12x, the area measured is about 24 x 18 mm. At the highest magnification, 160x, the area measured is about 1.9 x 1.4 mm with a height resolution of 0.1  $\mu\text{m}$  [37]. Examples of the height map produced from each magnification can be seen below in Figure 43.

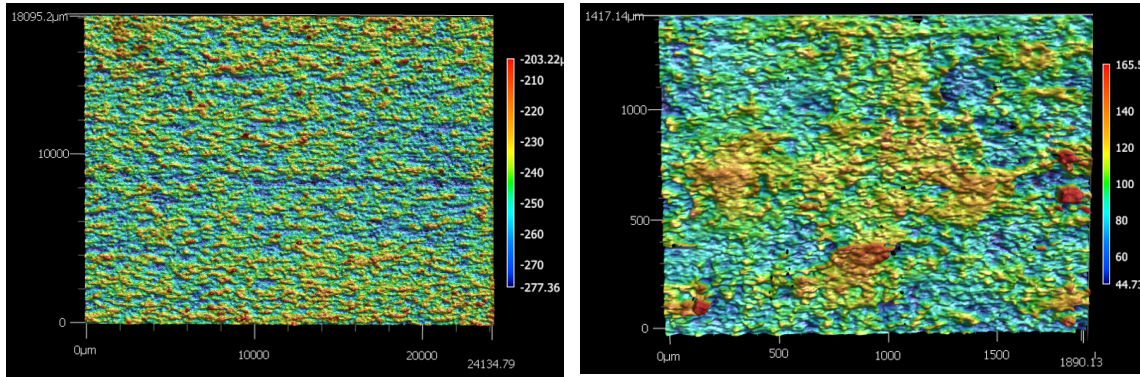


**Figure 43: (LEFT): 12x Magnification 3D Height Map of DMLS Sample (RIGHT): 160x Magnification 3D Height Map of DMLS Sample.**

The highest magnification was used for all surface parameter measurements and calculations in this section. The associated Keyence software that views and processes all the macroscope data allows for excel spreadsheets containing the raw surface height data to be exported, which enables custom post-processing and surface measurements.

The repeatability of this method for measuring surface height and calculating surface roughness parameters from its data was sufficient. As seen in Table 12 below, the repeatability for some of the common surface roughness parameters was good. Therefore, it is believed that this method is very well suited for measuring the metallic AM surfaces of the samples.

**Table 12: Keyence VR3100 Repeatability.**

Surface Roughness Parameter	$R_a$	$R_{rms}$	$R\Delta q$
Standard Deviation (% of Mean Value)	0.17 %	0.25 %	0.79 %

Now that the surface roughness measurement technique has been determined, a measurement methodology needed to be established. For this study, the surface roughness measurement procedure was used in guidance with the procedure used for

contact profilometry measurements in the same laboratory. However as mentioned above contact profilometry could not be used due to the extreme roughness and irregularity of the samples. The procedure used for the contact profilometer was modeled after the principles established in the ASME B46 standard [9]. A 12x magnification image was taken at the center of each sample to obtain a visual image of each sample. For the surface height data meant for analysis, there was a total of nine measurements points for each sample. In Figure 44, a diagram shows the locations of all nine points. At each location, an area of 1.9 x 1.4 mm was evaluated for surface height at 160x magnification. All nine points were then averaged together to get a single value for each surface roughness parameter for a given sample.

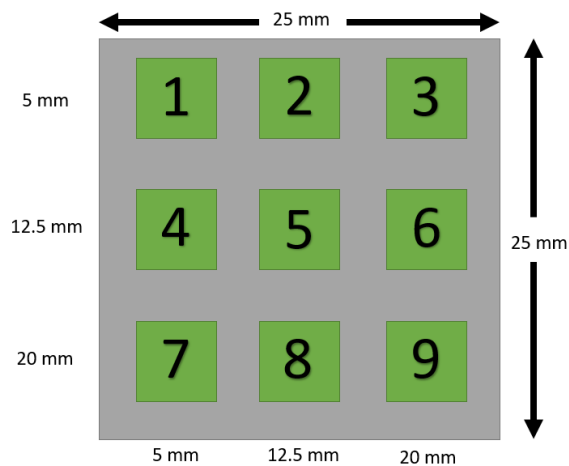


**Figure 44:** Surface Height Measurement Locations and Labels.

All surface measurements were performed while all the samples were still attached to the build plate to aid with positioning and leveling since the build plates themselves are machined to be level. Although it was believed that the samples on the build plate were level, a plane tilt correction was performed on all surface height data. No filtering was

performed on the raw surface height data as it could cause surface characteristics which could be influential to resultant emissivity to be thrown out. Both the linear and areal surface roughness parameters were evaluated. Areal measurements allowed for an easier analysis, but linear measurements were key since emissivity is dependent on view angle of the surface. In addition, since the samples were built with a 0/90 scan strategy, the surfaces are highly directional, which emphasizes the need for linear surface roughness measurements compared to the areal.

The surface height data was used to calculate traditional surface roughness parameters to allow for part variability assessment in addition to sample down selection for successive emissivity measurements. Emissivity measurements for each sample take a significant amount of time, and due to limited resources, all 72 samples could not be measured. Therefore, following the previous procedure of choosing build setting combinations to make the samples,  $R\Delta q$  was used to choose a subset of samples to move forward with in the study since the logic still follows that emissivity is related to  $R\Delta q$ . However, while the areal parameter  $S\Delta q$  was used for selecting the sample build parameters, the linear parameter  $R\Delta q$  was used in selecting the subset of samples to continue with for further measurements. This is due to the directional nature of emissivity and the 0/90 scan pattern used for the samples. A graph with all 72 samples demonstrating both position and build setting dependence on linear  $R\Delta q$  in both orientations can be seen in Figure 45. In viewing the resultant  $R\Delta q$  values, it was decided that samples in position 5, labeled sample “E” or “Echo” as they will be referred to, and samples in position 1, labeled sample “A” also referred to as “Alpha”, would move

forward to emissivity measurements. The selected samples' surface roughness values are circled in red in Figure 45. This decision came from the fact that the combination of both sets of samples provided a large, evenly spaced range of  $R\Delta q$  values in both the 0 and 90-degree orientations relative to the scan direction of the final layer of the build.

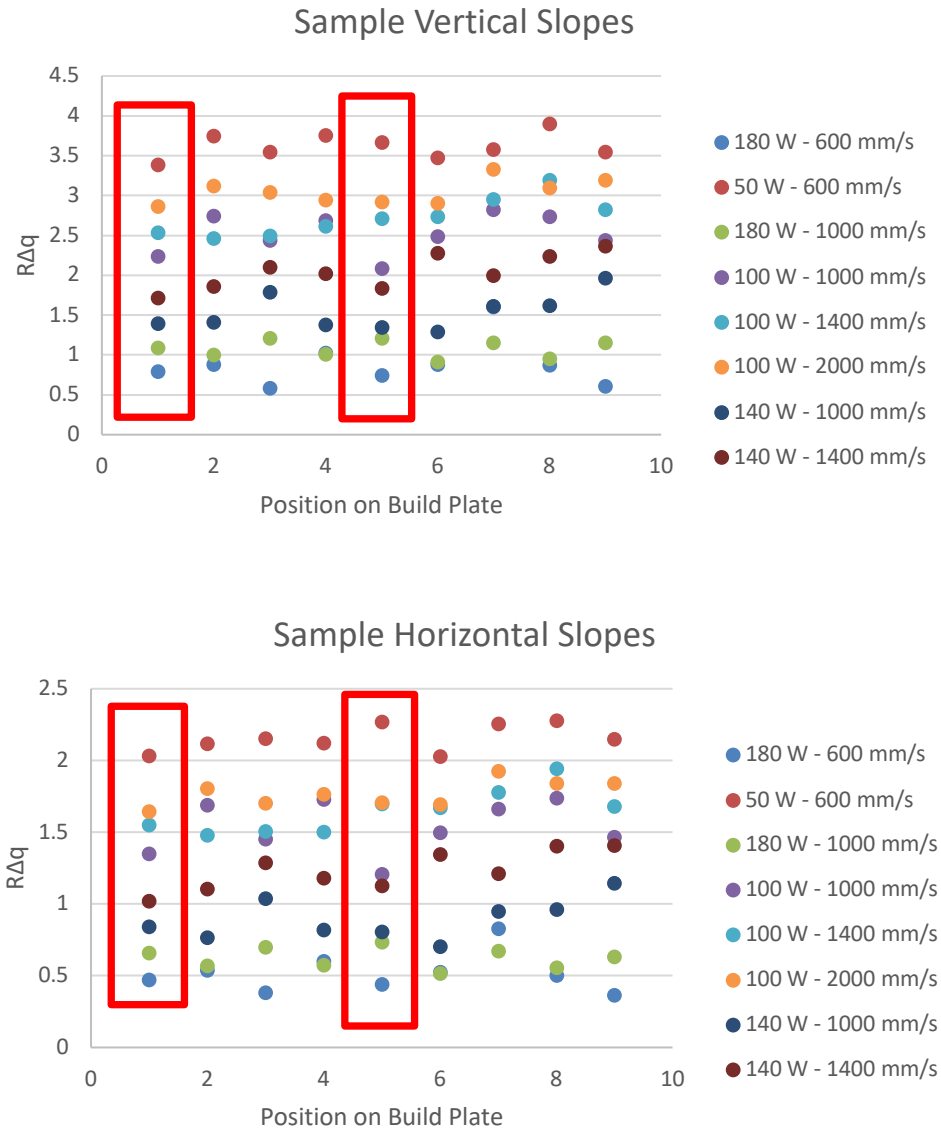


**Figure 45: (TOP)** Sample  $R\Delta q$  Values for Direction Perpendicular to Scan Vectors **(BOTTOM)** Sample  $R\Delta q$  Values for Direction Parallel to Scan Vector

## Position and Build Surface Roughness Variance

Looking at the surface roughness of all the samples, there are some clear trends. The samples that were closest to the roller home position (Samples G-I or 7-9) were the roughest both in terms of average surface roughness but also root mean square slope. The average percent deviation over all build parameter combinations for each sample position can be seen in Figure 46 below. There is a clear position dependence of surface roughness.

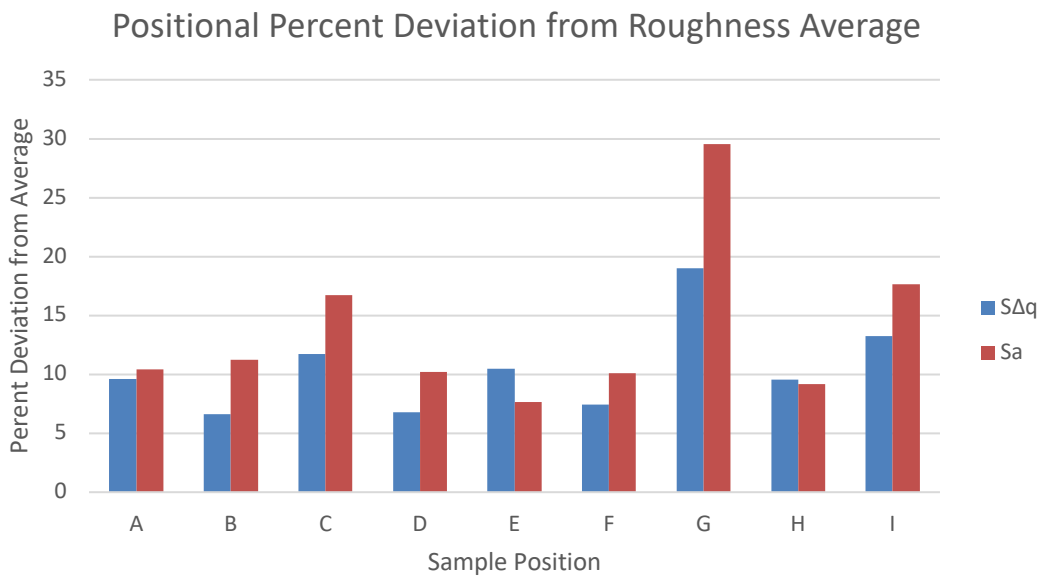


**Figure 46:** Positional Percent Deviation from Average Surface Roughness.

Not only is there a position to position variability in surface roughness as seen above, but there is also a build to build variability. The range of surface roughness values for a set of parts depends on the combination of build parameters, as can be seen in Figure 47. As the power increases and the scan speed decreases, the total range of surface roughness, specifically SΔq, increases slightly then declines steadily. This trend demonstrates how

dependent the surface roughness is to the thermal and fluid dynamics that dominate the melt pool. These results further support the need to be able to measure surface roughness in-situ to account for variations in emissivity that the surface topography causes.

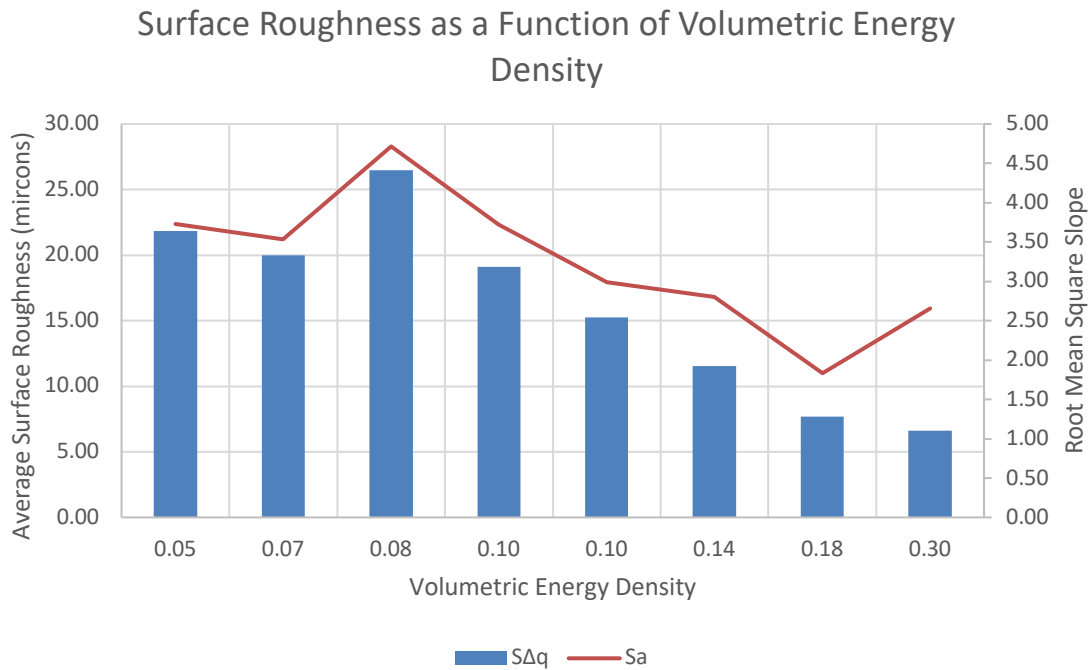


**Figure 47:** Surface Roughness as a Function of Volumetric Energy Density.

### EMISSION MEASUREMENTS

To measure emissivity, a Surface Optics Corporation Hemispherical Direction Reflectometer (HDR) connected to a Thermo Fischer Fourier transform interferometer (FTIR) was used. An image of which can be seen below in Figure 48. The HDR gathers the angular reflectance from the sample and direct it into the FTIR, which performs the spectral measurements of the radiation. The entire system measures sample reflectance at discrete angles, which is then integrated to calculate directional hemispherical emissivity of a sample in a controlled environment.



**Figure 48:** Hemispherical Directional Reflectometer Coupled with Fourier Transform Interferometer [38]. It is assumed that since the samples are sufficiently thick, that there is no transmission through the sample, and therefore Equation 8 can be used. The HDR was chosen due to its ability to measure the directional reflectance of the sample at a variety of angles to allow for the directionality of the additive surfaces of the samples to be observed. The HDR can measure angular reflectance from 10-80 degrees relative to the surface normal in 5-degree increments and has a wavelength range of 2.5-24 microns [38].

A basic functional diagram of the HDR can be seen in Figure 49 below. The sample is placed in the center of the hemisphere, and a black body is located at the base of the hemisphere offset from the center. The black body radiates towards the hemisphere which through reflection, directs the radiation onto the surface of the sample. A mirror on a gantry arm, rotates about the sample in 5 degree increments and directs the reflected radiation off the sample into the FTIR. The FTIR then produces a spectrum of the reflected radiation. The FTIR compares the spectrum to that of a reference sample and calculates reflectance. The reflectance of the sample over all measured angles and the wavelength range of the HDR are integrated to get at total hemispherical emissivity of the sample. A hemispherical emissivity is calculated for the two orientations of the sample, 0

and 90 degrees, which are relative to the scanning direction of the last layer of the samples, as seen in Figure 50. In addition to measuring the AM samples, baseline measurements were performed with a sanded surface finish and polished stock 316 SS material to gain a baseline emissivity value for comparison. The emissivity results of all samples and orientations can be found in Table 13 below.

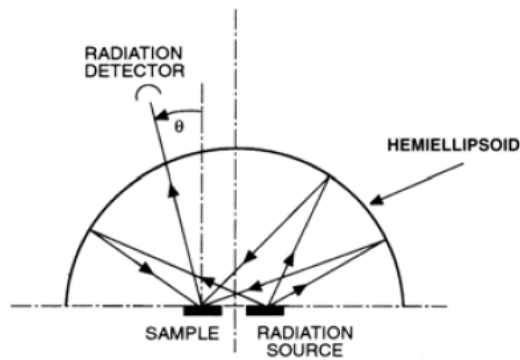


**Figure 49:** HDR Functional Diagram [38].

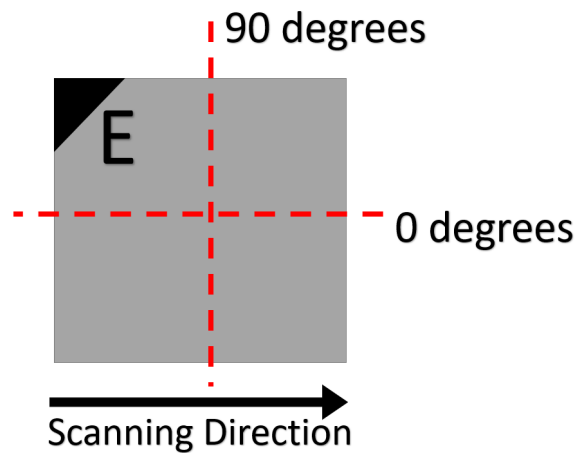


**Figure 50:** HDR Measurement Planes Relative to Scanning Direction.

**Table 13:** Hemispherical Emissivity Results of DMLS Samples.

<b>Laser Power (Watts)</b>	<b>Scanning Velocity (mm/s)</b>	<b>Sample Position</b>	<b>Parallel to Scan Direction</b>	<b>Perpendicular to Scan Direction</b>
50	600	Alpha	0.209	0.228
		Echo	0.244	0.247
100	1000	Alpha	0.153	0.192
		Echo	0.177	0.201
100	1400	Alpha	0.236	0.248
		Echo	0.247	0.255
100	2000	Alpha	0.171	0.198
		Echo	0.183	0.206
140	1000	Alpha	0.141	0.173
		Echo	0.140	0.171
140	1400	Alpha	0.139	0.169
		Echo	0.158	0.189
180	600	Alpha	0.134	0.143
		Echo	0.122	0.126
180	1000	Alpha	0.140	0.155
		Echo	0.143	0.163
Sanded SS 316 AM Samples Average Value			0.119	
Mirror Finish SS 316 Stock Average Value			0.094	

There were two main emissivity trends that were observed. The first of which is the clear dependence on orientation to the scan direction. As can be seen in Figure 51 below, the emissivity measured parallel to the scan direction is lower for all samples that were measured. This can be attributed to the fact that the surface roughness parallel to the scan direction is lower than the perpendicular orientation. This dependence on surface roughness will be discussed in further detail in the following section. The second trend observed is the dependence on volumetric energy density. Again, this trend refers back to the dependence of emissivity on surface roughness as the numerical trend in emissivity seen in Figure 52 mimics the decaying trend of surface roughness seen in Figure 47.

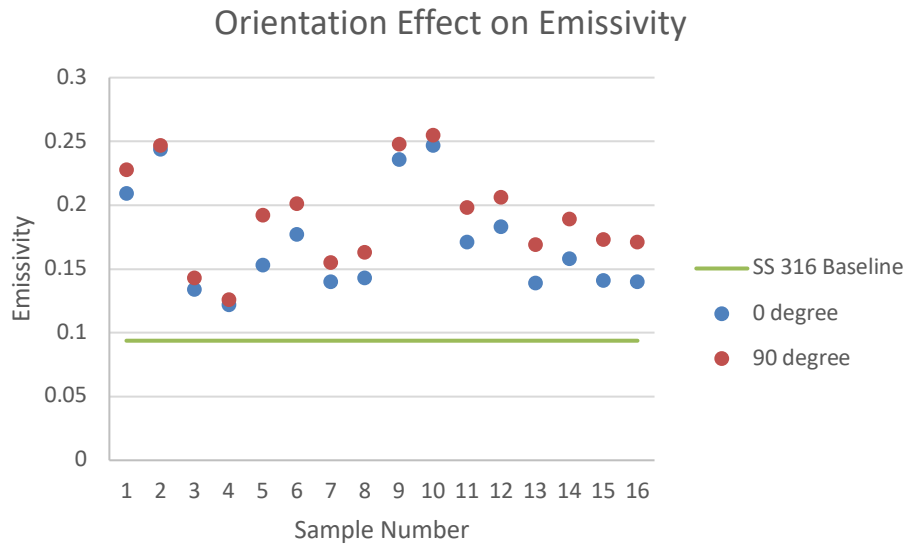


**Figure 51:** Total Hemispherical Emissivity based on Orientation to Scan Direction.

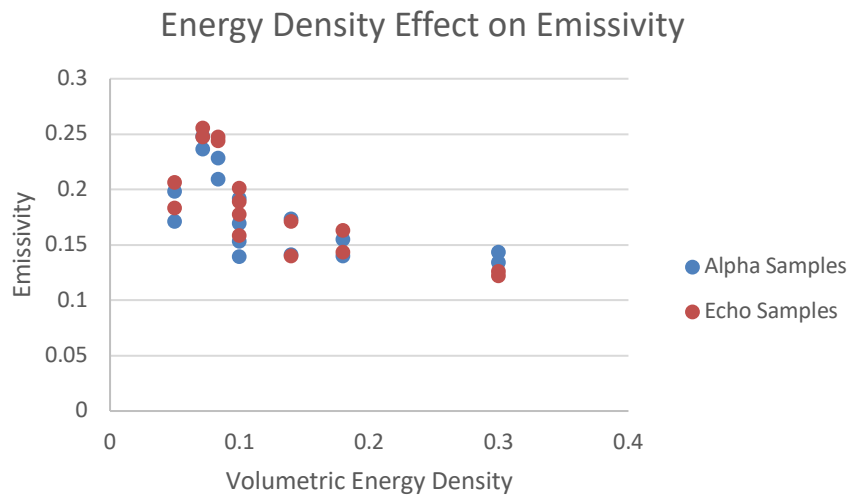


**Figure 52:** Total Hemispherical Emissivity based on Volumetric Energy Density.

### OXIDE LAYER MEASUREMENT

One other major consideration with the emissivity results is the effect of the thickness of the oxide layer on the parts. Oxidation can have a large influence on the optical properties of metallic parts. Since the parts see high temperatures during the build

process, the possibility for oxidation is high. Since the parts in this study were made with a range of build parameters, the dynamics of the process vary, providing the possibility that the oxide thickness of the parts may vary. Therefore, it is necessary to measure the oxide layer thickness of the parts whose emissivity was measured in order to discover whether or not the emissivity trends follow the oxide layer thickness trends or if they are independent of this property.

To perform the oxide layer thickness measurement, Auger electron spectroscopy (AES) was used. Since the parts are extremely rough, with varying surface roughness values, only a relative oxide layer thickness measurement could be performed. Traditional methods such as XRD, which uses index of refraction changes of the oxide layer thickness are unable to cope with the non-planar surfaces of the AM parts of this study. Even the chosen method, Auger Electron Spectroscopy, has challenges with the variability of surface roughness between the parts. The AES method removes the upper layer of the surface through sputtering and ejects, using an electron beam, Auger electrons that are analyzed to obtain its composition throughout the depth of material [39]. When the oxygen component of the composition drops, it is concluded that the oxide layer has concluded. A scanning electron microscope image of one of the samples used for this measurement can be seen in Figure 53. The red boxes represent the areas of measurement for the sample. The oxygen composition results for that sample can be found in Figure 54.

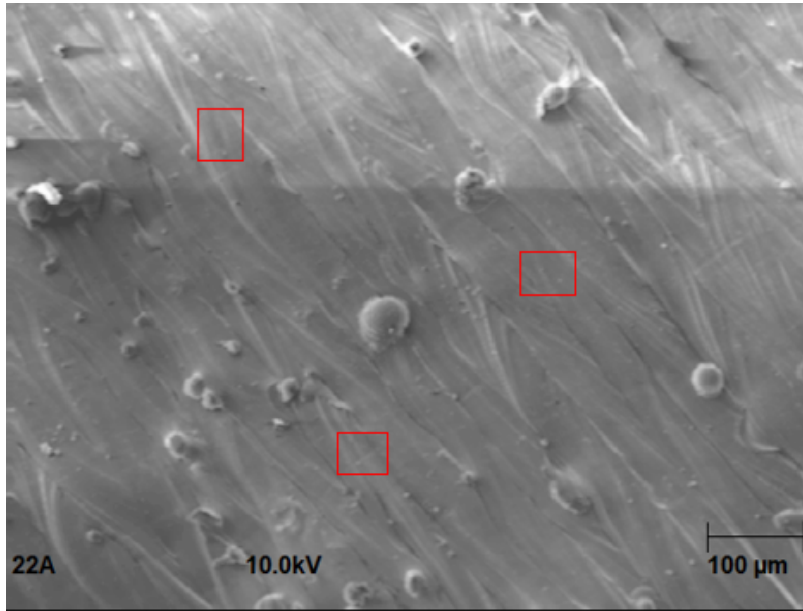


**Figure 53:** SEM Image of Sample A from Set 2 Build 2.

**Sample A from Set 2 Build 2 Oxide Average**

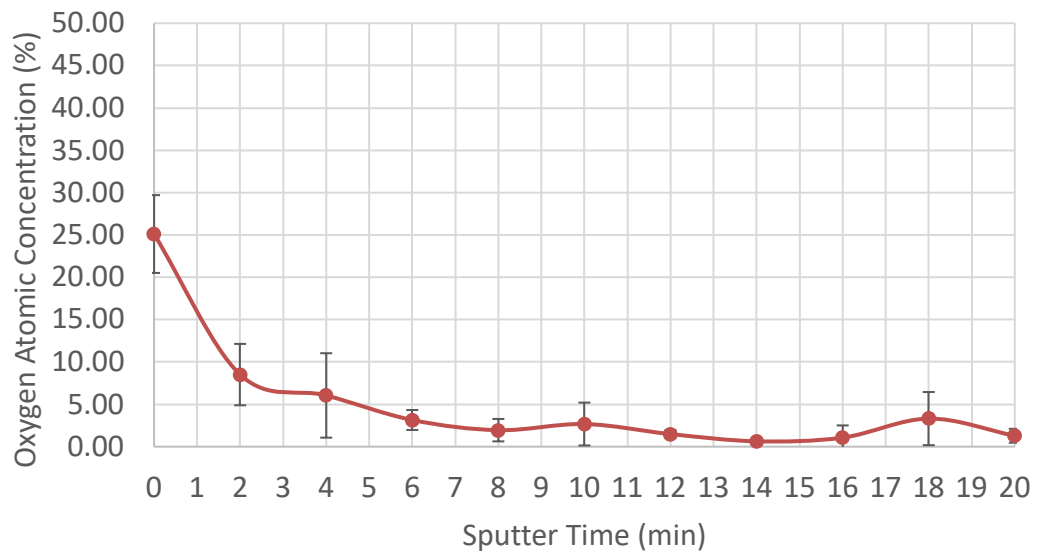


**Figure 54:** Oxygen Composition Results from AES for Sample A from Set 2 Build 2.

For these measurements, samples were compared with the time it took for the oxygen composition to drop below ten percent. A graph of part emissivity vs sputter time can be found in Figure 55 below. As can be viewed in the figure below, the difference in sputtering time between samples is negligible and is not the cause for emissivity differences. These results demonstrate that the parts only had a native surface oxide common to 316 stainless steel and no significant differences in oxide layer thickness. Therefore, it is believed that the emissivity of the samples is being controlled by the surface roughness.

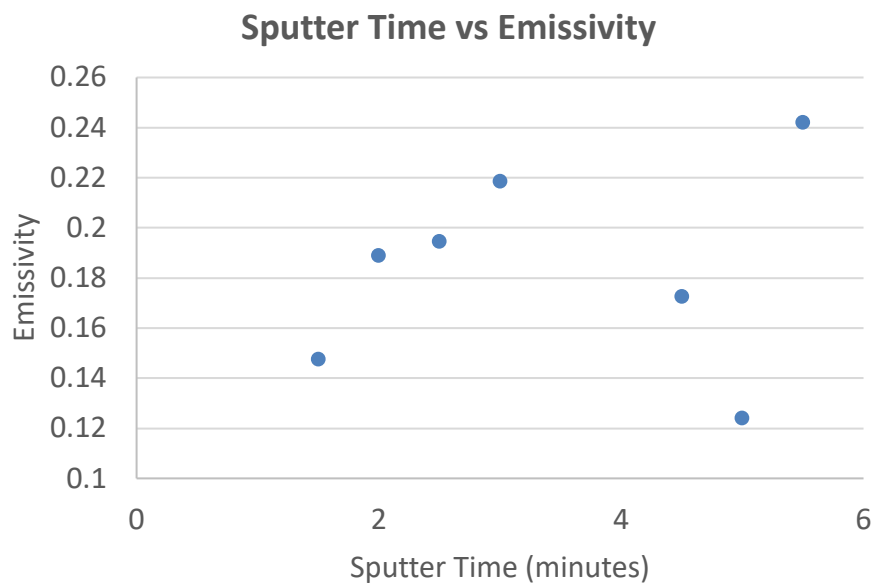


**Figure 55:** Sputter Time to Signal End of Oxide Layer Versus Sample Emissivity.

### **EMISSIVITY DEPENDENCE ON SURFACE ROUGHNESS**

Now that the surface roughness and emissivity data sets have been created, the next task was to investigate the best surface topography measurement that indicates emissivity changes. To be able to measure unique and novel surface topography

parameter, a custom MATLAB script was written to analyze the raw surface topography data produced from the Keyence MacroScope. This MATLAB script imports the raw surface height data and first removes the tilt plane if one is present in the surface data. The script calculates several standard areal surface roughness parameters to check the validity of the script in comparison to commercial surface analysis software. The script also calculates already existing linear surface roughness parameters in addition to the novel ones produced in the study in both the 0 and 90-degree orientation with respect to the last layer scan direction. The MATLAB program is flexible in terms of measurement spacing. Initial calculations were performed for every line of data available, which was 1.8 microns in width. Calculations were also performed at spacing of every 8 and 32 lines, but the correlation strengths did not change. However, calculations were also performed on the 12x zoom data, which had a linear spacing of 23 microns for each line, and the correlations were significantly smaller, demonstrating the need for high resolution at the level of the wavelengths of interest.

Some of the linear surface roughness parameters that were calculated for the surfaces include  $R\Delta a$  (average tilt angle),  $R\Delta q$  (root mean square slope), and  $Pc/cm$  (peak count per centimeter). These already existing surface roughness parameters are related to the shape of the peaks and valleys of the surface. Some of the unique parameters that were calculated included valley angle, valley height, and the ratio of the valley height and width. All of these unique parameters were calculated by finding each valley that was straddled by two peaks. Then the distance between the valley and each peak height was measured in addition to the distance between the successive peaks. Two angles were

calculated using each height with the peak to peak width, because one angle is wider than the actual valley angle while one is smaller. Therefore, the average of the angles is used to estimate the actual valley angle while remaining computationally simple. A diagram of this calculation can be found in Figure 56 below.

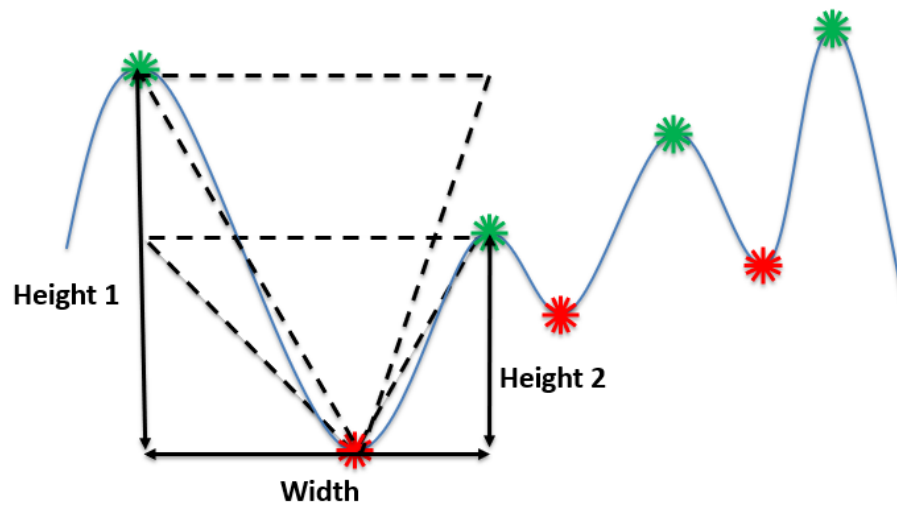


**Figure 56:** Valley Angle Calculation Diagram.

Once these new and existing surface roughness parameters were calculated, they were used to discover the parameter that had the best relationship with emissivity. The already existing parameters,  $R_a$  and  $R\Delta q$ , plotted against the emissivity values for the samples to observe the correlation strength.  $R_a$ , the average surface roughness, was plotted specifically since it was the most prevalent parameter in the literature that described surface roughness for additively manufactured parts. However,  $R_a$  only had an  $R^2$  value of .66, which was one of the weakest relationships with emissivity among the already existing surface roughness parameters.  $R\Delta q$ , the root mean square slope, was plotted since it was suggested that it is a better distinguisher between surfaces that have

similar average roughness values [36].  $R\Delta q$  had a  $R^2$  value of .79, which was one of the strongest relationships with emissivity. These plots are found in Figure 57 and Figure 58.

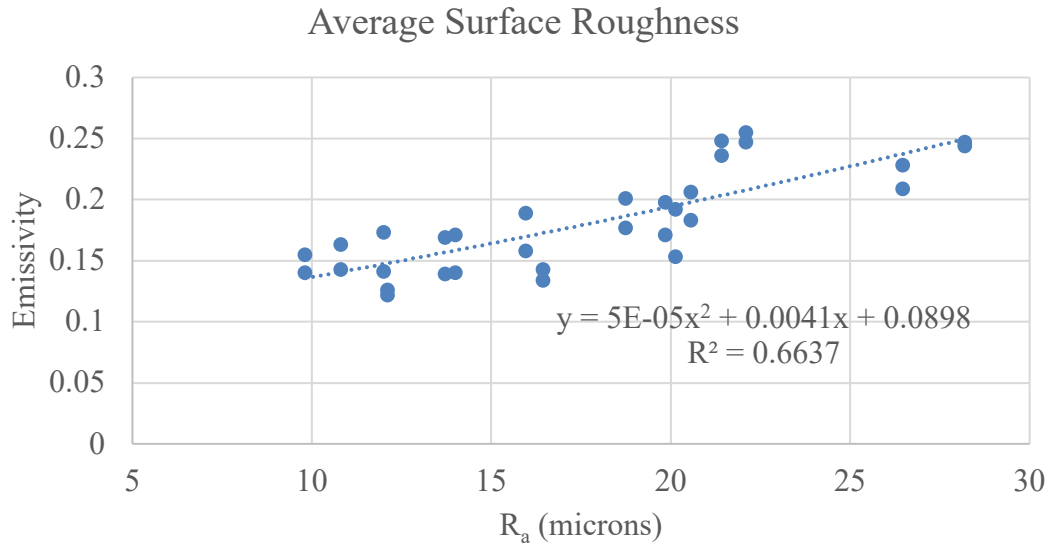


**Figure 57:** Linear Average Surface Roughness Plotted Against Hemispherical Emissivity.

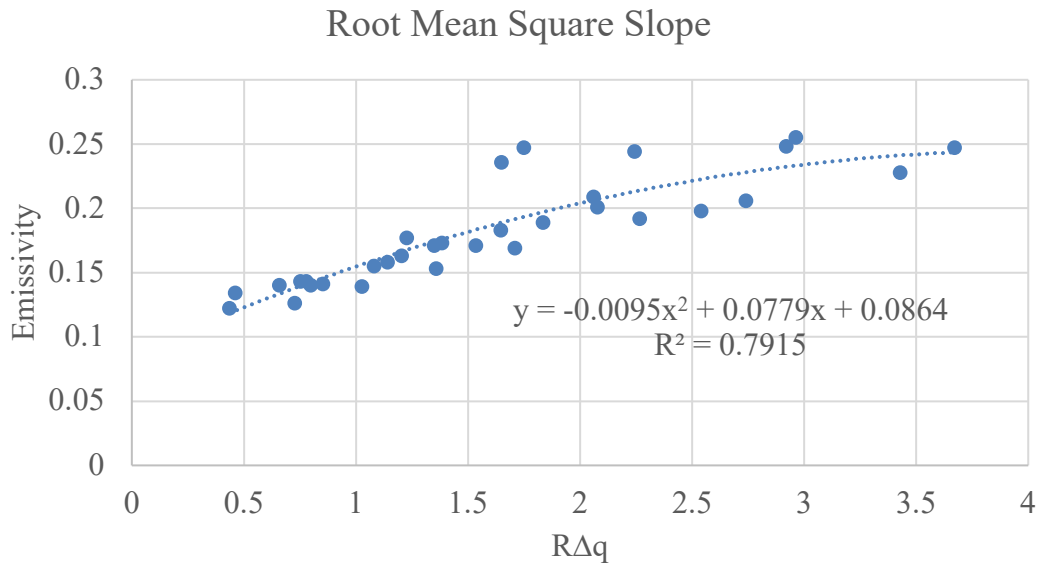


**Figure 58:** Linear Root Mean Square Slope Plotted Against Hemispherical Emissivity.

Single parameters and various combinations of parameters were tested for the strongest correlation. It was found that both new and a combination of already existing parameters had the best correlations with emissivity measurements. The new parameter with the best correlation was the valley angle multiplied by the valley height, which had an  $R^2$  value of 0.823. The combination of already existing parameters, which was  $R_a$  multiplied with the  $R\Delta a$ , had a  $R^2$  value of 0.834. This combination of parameters refers to the average height of the surface profile multiplied by the slope of the surface, both of which are related to the valley angle and height as described by the new surface roughness parameter.  $R\Delta a$  describes how steep the valleys of the surface are while the  $R_a$  value shows how deep the valleys could be. The steeper and taller valleys provide more opportunity for internal reflections, increasing the emissivity value. The plots of each can be found in Figure 59 and Figure 60 below.

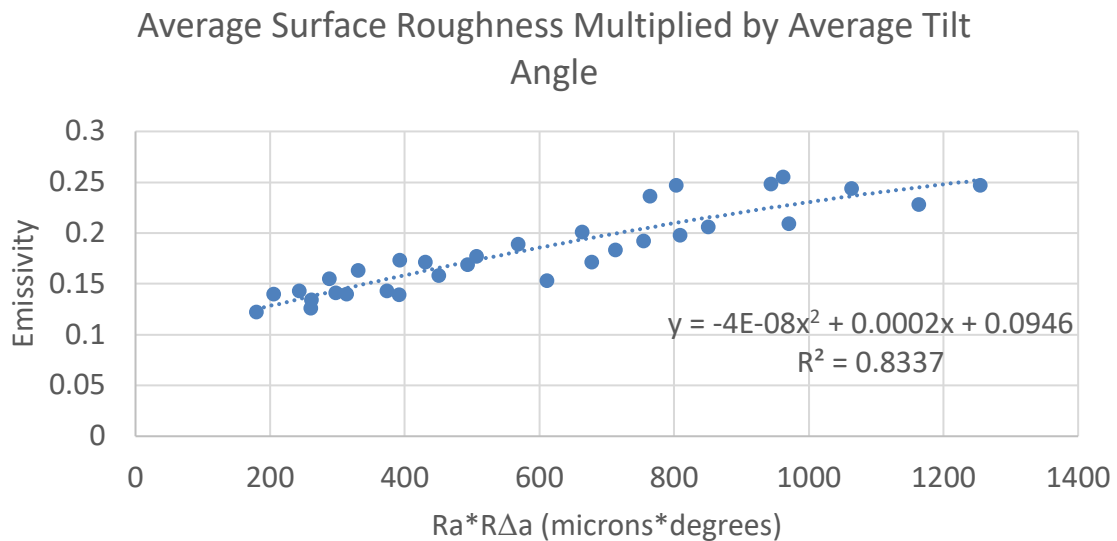


**Figure 59:** Average Surface Roughness Multiplied by Average Tilt Angle Plotted versus Hemispherical Emissivity.

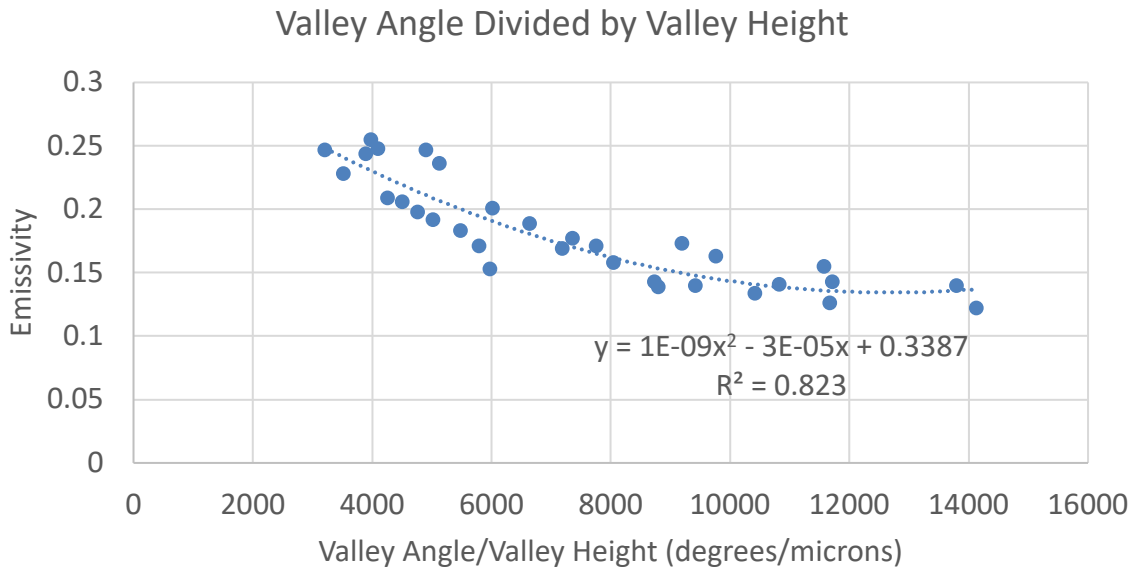


**Figure 60:** Surface Valley Angle Divided by Valley Height Plotted versus Hemispherical Emissivity.

While the average value of the nine measurements taken for each sample was used to compare with emissivity results, there was some surface variation within each sample. The variable surfaces across the sample affect the overall emissivity, so the average value of the nine points was used. As can be seen in Table 14 below, there is some slight variation within the samples as seen from analyzing the data of the nine measurement points. The table represents the average value and average standard deviation of surface roughness parameters within all AM samples that had the emissivity measured. All of these single measurement points would produce different emissivity values based on their differing geometry, but since the surface is being measured as a whole, the surface measurements are averaged together. This is one complexity that additive surfaces add to predicting emissivity based on surface roughness. In traditional

manufacturing techniques, this issue is not usually present as most subtractive techniques produce periodic structures with very little variance across the surface.

**Table 14:** Surface Roughness Variation Among Nine Measurement Points Taken Within AM Samples.

	<b>R<sub>a</sub> (μm)</b>			<b>RΔq</b>			<b>RΔa (degrees)</b>		
	Average	Std. Dev.	Percent Dev.	Average	Std. Dev.	Percent Dev.	Average	Std. Dev.	Percent Dev.
<b>0 Degree Direction</b>	17.65	2.05	11.6 %	1.23	0.12	9.7 %	28.15	1.53	5.4 %
<b>90 Degree Direction</b>	17.65	2.05	11.6 %	2.04	0.20	9.8 %	35.62	1.62	4.5 %

The results and figures in this results section demonstrate the relationship between emissivity and just a few key surface roughness parameters. A more comprehensive list of what surface roughness parameters both new and existing that were looked into can be found in Appendix A with their correlation coefficient (R<sup>2</sup>) value included.

## Conclusions

For the geometric optical region where the average surface roughness value is greater than or equal to the measurement wavelength, the emissivity is highly affected by the surface roughness. Through the simulation work, it was found that the most influential aspect of the surface roughness was the valley angle. This aspect dictates the internal reflections, which increase absorbance of the surface. This behavior causes the emissivity to increase. It was also found that arithmetic mean surface roughness, R<sub>a</sub>, was a very poor indicator of emissivity trends as surfaces would have the same arithmetic mean height, but different shapes and therefore emissivity values. It was confirmed with the experimental measurements, that the valley angle was key to predicting emissivity

behavior. It was found that combination of the angle and overall height of the valleys that composed the surface had the best relationship with emissivity when looking at possible new surface roughness measurements. A combination of already existing surface roughness parameters which relate to the slope and height of the valleys, was found to have the strongest relationship with emissivity. This combination was the product of average tilt angle and the arithmetic mean height. This combination is believed to have the best relationship because it is indicative of the surface shape that creates the Mendenhall wedge effect where a steeper and taller wedge or valley will produce more internal reflections, which cause a greater absorbance. This is observed as an increase in emissivity.

This study focused on a single material, 316 stainless steel, to keep that aspect of the experiments constant. However, it is suggested that the effects that surface roughness has on other metals varies. Bergstrom et al. showed that the more reflective the metal, the more sensitive its emissivity behavior will be to surface roughness differences. Since the reflection of the surface is larger, the more surfaces, the more chances a ray of light has to reflect off multiple surfaces, increasing the effective reflection of the entire surface. For less reflective materials, the relative amount of reflection when encountering multiple surfaces does not increase as much as the higher reflective materials, making it less dependent on surface roughness changes [40].

## **CHAPTER 2: ANGULAR SENSITIVITY OF SURFACE ROUGHNESS DEPENDENT EMISSIVITY BEHAVIOR**

The purpose of this task is to observe emissivity trends of varying surface roughness, view angle, and temperature and to discover the possible measurement errors caused by incorrect assumptions. For this task, in build conditions will be more closely simulated to discover more realistic emissivity values that will be present during a build. Since the HDR measurements were made near room temperature, it is key to observe the surfaces at the elevated steady state temperatures closer to those seen during the DMLS process. To create the simulated build environment, a vacuum furnace setup will be leveraged. Once the tests have been performed, trends between the three variables mentioned above will be investigated and best practices will be deduced from the results and discussed in the conclusion of this section.

### **Vacuum Furnace Setup**

The vacuum furnace system used for this study includes a vacuum furnace, consisting of a vacuum chamber with a tungsten coil heating element surrounding an aluminum oxide crucible, optical train, and LabVIEW control software. This vacuum furnace system was previously designed for calibrating infrared cameras using a concurrent passive microwave system. The passive microwave sensor allowed for both a direct temperature and direct emissivity measurement due to its unique capabilities. More information on the microwave measurement process can be found in Woskov and Sundaram [41].

The system was slightly modified to fully leverage it for this study. Mainly, this consisted of simplifying the optical train and adding sample holders inside of the crucible. A diagram of the system as it was setup for this study can be seen below in Figure 61.

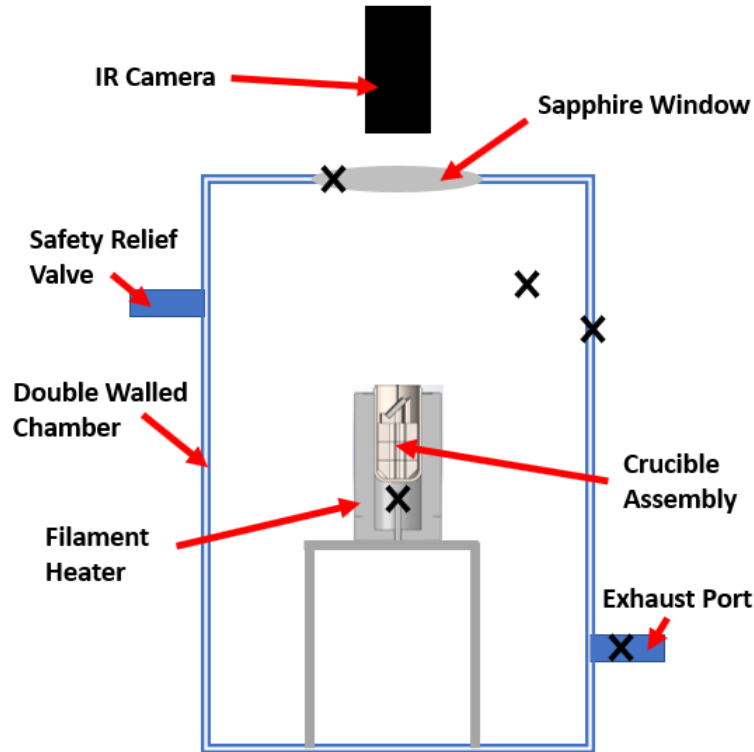


**Figure 61:** Vacuum Furnace Setup Diagram.

As seen in Figure 61, the vacuum chamber has a double wall to contain a water cooling system that creates a safer system for the operator, allowing for the system to achieve higher temperatures while still maintaining a lower outer shell temperature. The chamber has a sapphire viewing window which is located at the top of the chamber which allows the parts in the crucible to be easily viewed by the camera as seen in Figure 61 above.

The transmission of this viewing window is high for the short-wave infrared, mid-wave

infrared, and microwave ranges, which were used in previous studies conducted with this system. The transmission spectrum for the window can be seen for the infrared wavelengths below in Figure 62.

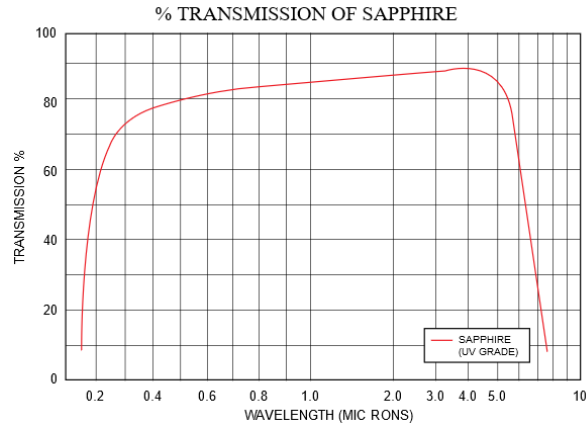


**Figure 62:** Transmission Spectrum of Sapphire Viewing Window [42].

The heating element in the system is a tungsten heater coil which is placed towards the center of the chamber via a built-in shelf. An aluminum oxide crucible that is 75 mm in diameter and 100 mm tall sits in the middle of the heating coil. This crucible will contain the sample and any fixturing that will be used. A detailed view of the crucible assembly can be seen in Figure 64 below. There are five thermocouples placed on various aspects of the chamber as well as the heating element and crucible. Their locations are marked with a black 'X' in Figure 61.

The optical train for this study is composed of the mid-wave infrared (MWIR) camera and the sapphire window that allows the MWIR to have a direct line of sight to the metal AM sample in the crucible. The MWIR camera used is a FLIR SC6811 camera that has a maximum temperature of 350 degrees Celsius when not using a filter. The camera control and monitoring will be performed by ResearchIR, which is the FLIR

proprietary software. A custom LabVIEW code was written to monitor and control every aspect of the vacuum furnace system except for the vacuum pump and optional atmospheric gas controls. The LabVIEW software dictates the rate of heating of the tungsten element. It also displays and records all the thermocouple measurements throughout the system including the sample temperature.

### **Simulating in Build Environment**

There are several aspects of the vacuum chamber that were modified to more accurately simulate a DMLS build. Instead of the heating of the samples in a low vacuum atmosphere, the system is first placed at a low vacuum and then backfilled with argon gas at a pressure of about 1 Torr. Argon is a common atmosphere for both 316 SS and many other metals when processing with DMLS. In addition to the atmosphere, the viewing angle of the IR camera with respect to the surface normal of the sample is key in reproducing near build conditions. Thermal monitoring is popular in the qualification of both the DMLS process and parts produced. Since commercial machines are difficult to modify, the placement of view windows or IR cameras is difficult, therefore the angle of the camera relative to the surface normal varies a great deal as researchers place the cameras or viewports in any viable location they can. Through reviewing several AM thermal monitoring papers, it was found that the most common viewing angles of IR cameras placed for monitoring are 0, 25-35, and 45 degrees [43, 44, 4, 3]. The 0 degree view angle is a reference to many thermal monitoring sensors that are bore-sighted with the laser and therefore view the surface at or very near the normal. It was decided that 0,

30, and 45 degrees would be used as the viewing angles for the heated tests. To create these viewing angles, the samples will be held using a custom angled sample holder designed for this experiment. CAD images of some of the sample holders can be seen below in Figure 63.

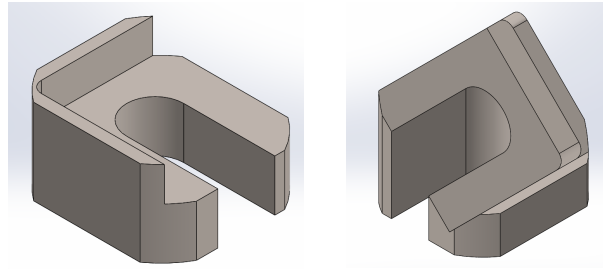


**Figure 63: (LEFT) 0 Degree Sample Holder (RIGHT) 45 Degree Sample Holder.**

As stated before, this study focuses on the emissivity of solid surface in a DMLS build. Since the melt pool's emissivity is even more complex due to the rapid changes in temperature, fluid dynamics, and phase transformation, this study's focus is on fully solidified surface generated during the process. Since the surfaces will be fully solidified, they will be at steady state temperatures. To discover what the steady state temperature is during a build, inquiries with machine operators and a literature review were conducted. Machine operators for both the DMLS process and the laser engineered net shaping (LENS) process were questioned as to the estimated steady state temperature for 316 stainless steel processing. The recently solidified regions of the parts produced were observed to be slightly below red-hot, which was around 600 degrees Celsius [45]. Through a combination of simulation studies that were found through a review of literature, the steady state temperature range was estimated to be 700-800 Celsius [46, 47]. Although the consensus for steady state build temperatures are around 600-800

degrees, the maximum operating temperature for this study will be 300 degrees Celsius due to the limitations of the MWIR camera used. The main difference in running at the lower temperatures is that the wavelength of peak radiation is longer, at about 5 microns compared to the peak wavelength of about 3 microns when running up to 700° as seen in Figure 1.

### **Experimental Procedure**

Before the heated runs were performed, data sets were gathered at room temperature for all angles and samples using both MWIR and LWIR cameras. The LWIR camera was used for these measurements in addition to the MWIR to observe the effects of the view angle and surface roughness differences on different wavelength range cameras. The LWIR camera was unable to be used in the heated runs because the sapphire window of the furnace is opaque for the 8-13 micron wavelength range of this camera. For these room temperature measurements, the furnace lid was removed, and IR images were taken of all the samples while sitting in the crucible assembly, just like they would be during the heated runs. Four angles were used in these room temperature measurements to observe the possible effects for 0, 15, 30, and 45 degree view angles since a large range of view angles can be found in AM literature. The results of these room temperature measurements can be found in the results selection below.

For this study, a subset of six samples from the sixteen, whose emissivity was measured with the HDR, will be measured in this experiment. For each sample, three runs will be conducted, each at a different view angle. For each run, the emissivity will

be back calculated at increments of thirty degrees from room temperature to 300° C. The procedure for each run is as follows. First, stainless steel spacers will be placed in the crucible to place the angled sample holder and sample in the focal range of the IR camera. A high temperature, bare type K thermocouple will be attached to the sample holder via a spot weld using an Orion Pulse 250i micro TIG welder in order to monitor the temperature of the sample. A cross sectional view of the completed assembly within the crucible can be found in Figure 64 below.

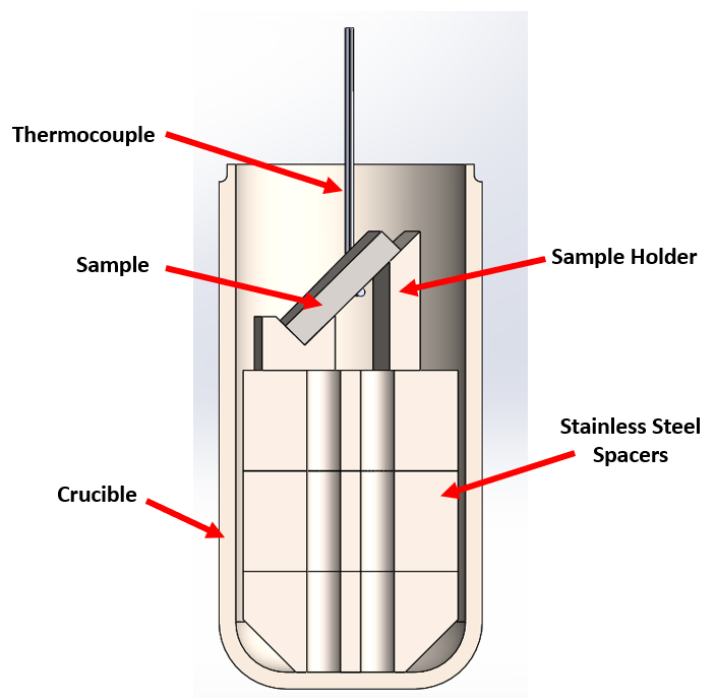


**Figure 64:** Cross Sectional View of Crucible Assembly.

Once the assembly has been completed, the crucible will be placed into the heater within the chamber. The vacuum chamber lid will then be lowered and bolted to the body. A vacuum will be placed on the chamber. Following this, the chamber will be backfilled with pure Argon until the pressure is about 1 Torr. Using the LabVIEW

software, the heater will be ramped up using a PID controller to achieve set temperature points at a spacing of 30° C from 30-300° C. This method of control will allow the temperature of the sample to remain at the desired temperature while the saving of data is occurring. Data points will be taken at 30° C increments starting at room temperature and concluding at 300 C. The data gathered at each increment includes thermocouple measurement values, chamber pressure, and a set of IR temperature images at a range of emissivity values. Once the final temperature of 300° C has been reached, the heater will be turned off, and the entire system will be allowed to cool to setup for the next experimental run.

Once the physical experiments have been conducted, the emissivity values for each sample at each viewing angle and temperature point will be calculated. During the experiments, a set of IR images was saved with each image at a different emissivity value. The temperature images will be analyzed and the image that minimizes the error between its temperature reading of the sample and the temperature from the thermocouple attached to the sample will be used. The camera input parameters such as ambient temperature, atmospheric temperature, and external optics temperature can be measured directly through thermocouples placed in the vacuum chamber. Since the emissivity of the samples is what is being calculated, temperature images are generated using an emissivity range of 0.1-1.00 in 0.01 increments for each temperature data point taken during a run. For a single temperature point, the temperature of the sample measured with the attached thermocouple is used to compare with the temperature images generated from the camera. The image that generates the temperature image that

minimizes the difference between the average sample temperature and the measured thermocouple value is determined to be indicative of the emissivity value for the sample at that given temperature point. A similar procedure has been performed in similar studies that looked at determining emissivity of an irregular surface such as in Larciprete et al. [48].

### **Sample Selection**

The samples used in these experiments were chosen with the same logic as the down selection for the emissivity measurements. Samples were chosen so that there was both a range and similar values of emissivity. As seen in Figure 65, samples (boxed in red) were chosen that had similar emissivity values, similar positions in a build, and similar volumetric energy densities. All of these factors were considered in order to be able make conclusions on the effects of these factors on the estimated emissivity value of the samples. The build parameters and measured emissivity value from the HDR can be found in Table 15 below.

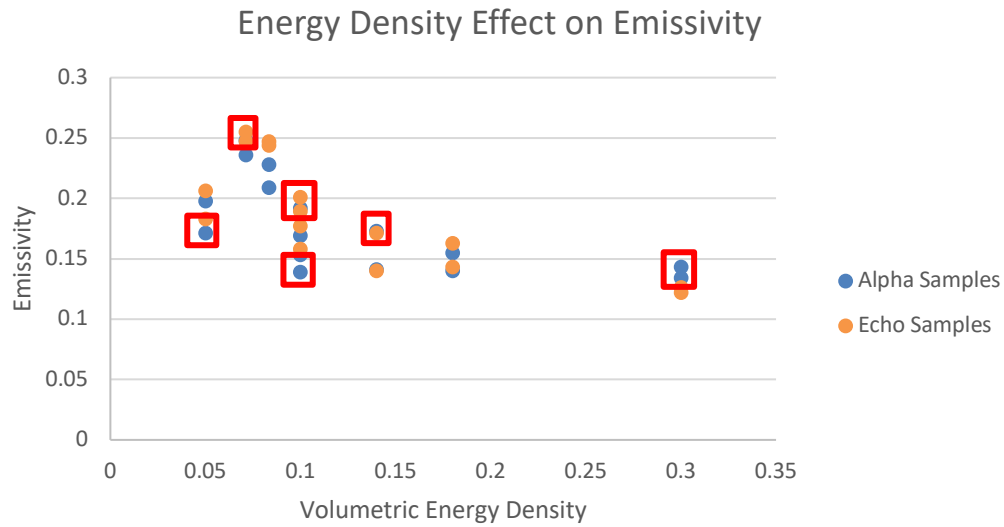


**Figure 65:** Energy Density Effect on Emissivity with Selected Samples Boxed.

**Table 15:** Selected Samples for Vacuum Furnace Tests.

Sample Position	Laser Power	Scan Velocity	Volumetric Energy Density	Orientation	Emissivity
A	100	2000	0.05	0	0.171
A	140	1400	0.1	0	0.139
A	180	600	0.3	90	0.143
E	140	1400	0.1	0	0.158
E	100	1400	0.07	90	0.255
E	140	1000	0.14	90	0.171

In addition to the total hemispherical emissivity measurements seen above in Table 15, the HDR also produced reflection data at an angle range of 10-65 degrees from surface normal. This data demonstrated that the angle of observation was key in the amount of reflection given by the AM surfaces. As seen in Figure 66 and Figure 67 below, for the samples chosen for this experiment, it is expected that the view angle of the IR camera will influence the optical response seen from the surface. Although the

HDR measured over the wavelength range of 2-24 microns, the data was grouped into the common IR camera wavelength ranges of 1-3 microns (which was actually 2-3 since the HDR didn't measure the shortest wavelengths), 3-5 microns, and 7-13 microns. As can be seen in the figures below, the angular behavior between samples varies, demonstrating the need to observe the AM samples at a range of common observation angles used to see how much the view angle affects the emissivity for a given IR camera range.

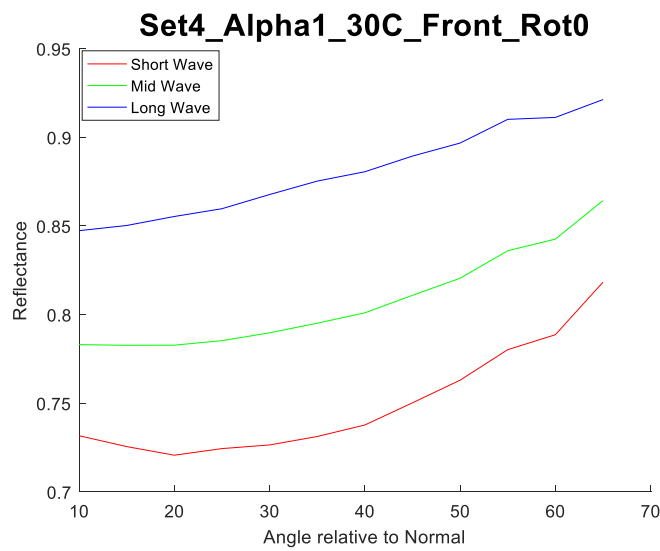


**Figure 66:** Angular Reflectance at Various Common IR Wavelength Ranges for the 0 Degree Orientation of Sample A Built from Set 4 Parameter Set A.

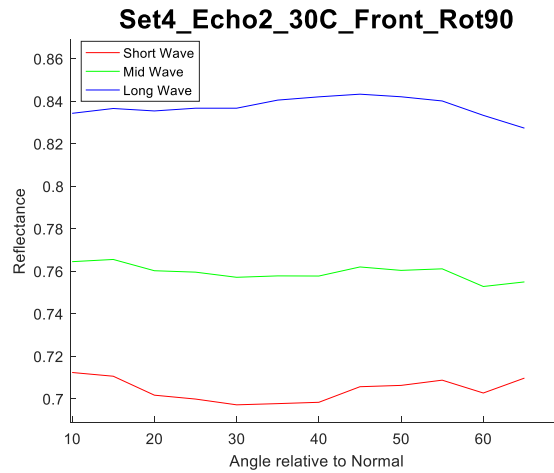


**Figure 67:** Angular Reflectance at Various Common IR Wavelength Ranges for the 90 Degree Orientation of Sample E Built from Set 4 Parameter Set B.

## Results

A variety of results were analyzed for this experiment. The effects of temperature in conjunction with varying surface topographies was considered. View angle dependence of emissivity changes for various surfaces was also investigated.

### ROOM TEMPERATURE MEASUREMENTS

These measurements were performed to observe the effects of view angle and observation wavelength on emissivity of samples that had a range of surface topographies. For the MWIR camera, all of samples saw a decrease in emissivity as the view angle increased from normal to the surface to 45 degrees from the surface normal. This trend can be seen in Figure 68. It is believed that as the view angle increases relative to the surface normal, for these extremely rough surfaces, shadowing phenomena comes into play where light doesn't reach parts of the surface, which can prevent internal

reflections [40]. As internal reflections decrease, the observed absorption decreases, and through the ideal assumptions, so does emissivity.

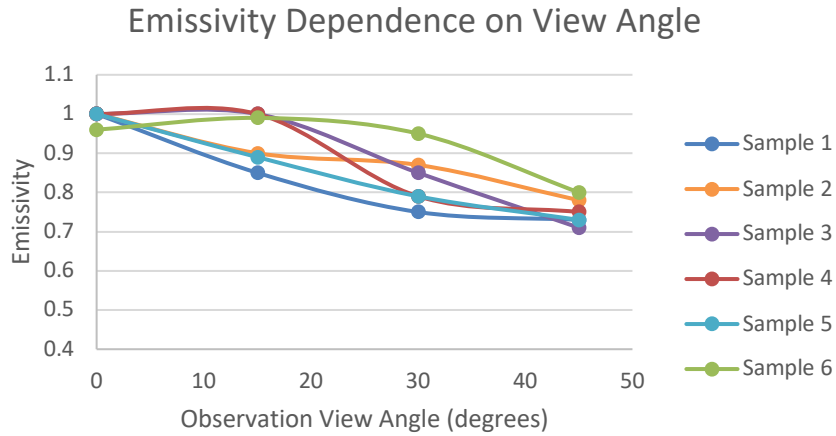


**Figure 68:** Emissivity Dependence on View Angle Measured with MWIR Camera at Room Temperature.

For the LWIR camera, there were no set trends related to view angle. For an increasing view angle, most of the samples had varying degrees of increase and decrease, with no consistent trend between them. This can be seen in Figure 69 below.

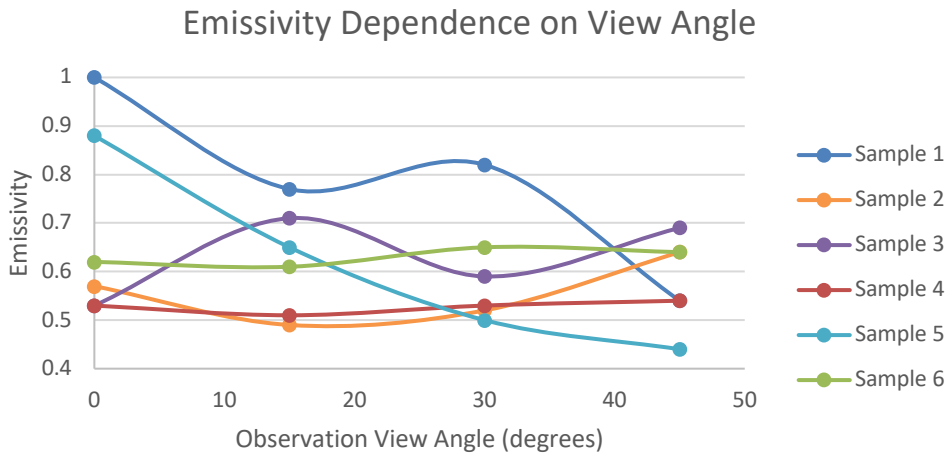


**Figure 69:** Emissivity Dependence on View Angle Measured with LWIR Camera at Room Temperature.

It is believed that the measurements for the LWIR are more randomized due to the changing optical regimes. As discussed in the introduction section, as the ratio between the  $R_q$  roughness of the surface and the measurement wavelength approaches and falls below 1, the effects of surface topography on the emissivity decrease. Therefore, as there is a range of roughness among the samples, the optical regimes they fall under using the LWIR camera vary. The different results between the LWIR and MWIR camera clearly demonstrate the effects of various optical regimes describing the relationship between surface roughness and emissivity. It is also clearly seen in these results that view angle does influence emissivity no matter which camera is used.

#### **RAISED TEMPERATURE MEASUREMENTS**

Emissivity calculations were performed at elevated temperatures to observe emissivity trends at a range of temperatures. This is key due to the large ranges of temperature seen in the metallic additive manufacturing processes. To reiterate, these elevated temperature experiments were performed using the MWIR camera. An example image of one of the sample runs can be found in Figure 70 below.

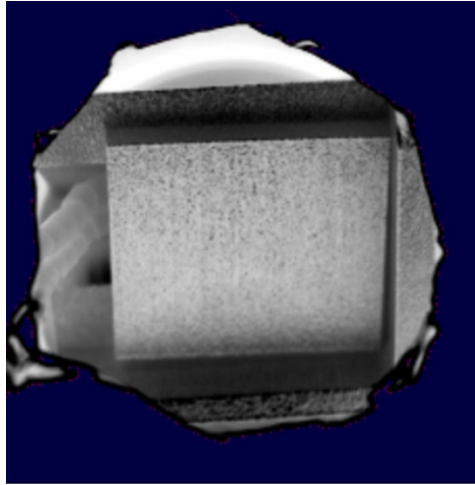


**Figure 70:** MWIR Image of Metal AM Sample Placed in 45 Degree Holder.

It was found that up to a threshold temperature, the emissivity trends for the changing view angle were like those found during the room temperature measurements. As can be seen in Figure 71-70, as view angle increases, the emissivity decreases. This again is attributed to the shadowing effect which counteracts the internal reflection phenomena that increases emissivity with increasing surface roughness. The decrease in emissivity as view angle increases can produce temperature error of at least 20 degrees Celsius before the threshold temperature where emissivity reaches a steady state value for all view angles.

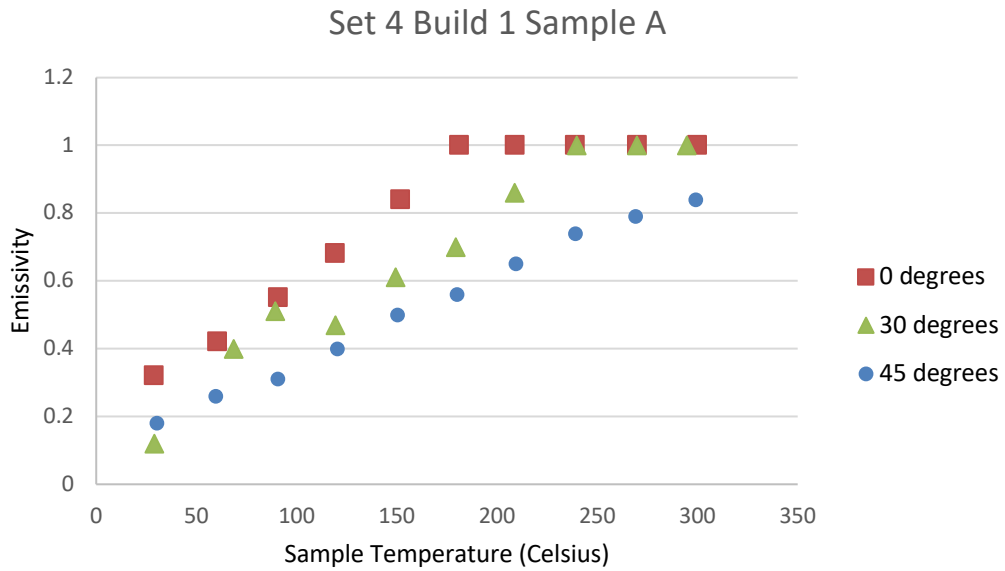


**Figure 71:** Elevated Temperature Emissivity Results at Range of View Angles for Set 4 Build 1 Sample A.

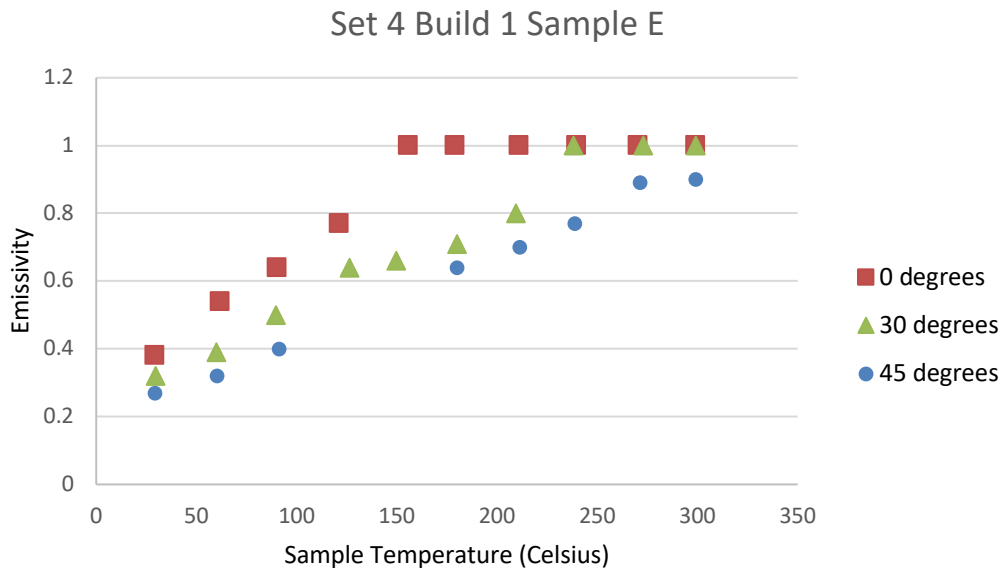


**Figure 72:** Elevated Temperature Emissivity Results at Range of View Angles for Set 4 Build 1 Sample E.

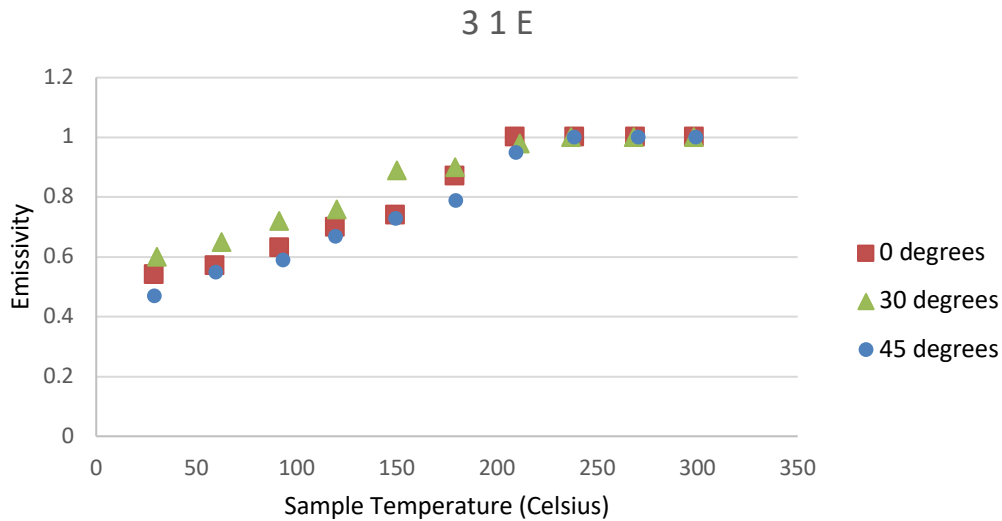


**Figure 73:** Elevated Temperature Emissivity Results at Range of View Angles for Set 3 Build 1 Sample E.

As clearly seen in Figure 71-70, as temperature increases, the emissivity reaches a steady state value. This trend means that at the elevated temperatures, the emissivity difference between view angles is non-existent. The trends observed, while the values are incorrect, since emissivity cannot be 1.00 unless the object is a black body, follow general emissivity trends seen with increasing temperature. The incorrect emissivity values for the higher temperatures are believed to be attributed to incorrect window transmission values as the temperature of the window changes, but the effects on the window transmission were unknown. Another possible source of error is the incorrect reflected temperature input into the MWIR camera. The exact reflected temperature was estimated as the exact temperature of the crucible and aluminum foil aperture were unknown.

There are also still differences between samples with different surface roughness values. Although the  $R_a R_{\Delta a}$  value describes the emissivity normal to the surface, the

effects that the roughness has on the emissivity at different view angles is more complex. Due to the shadowing effects, which were not a focus of this study, the emissivity value changes in different ways for the different roughness values. The general trend observed was as the surface roughness increases, the range of emissivity values between view angles decreases. This trend can be observed by looking at Figure 71, which has a  $R_a R_{\Delta a}$  value of 391 microns $\times$ degrees, then Figure 72 which has a  $R_a R_{\Delta a}$  value of 567 microns $\times$ degrees, and finally Figure 73 with a  $R_a R_{\Delta a}$  value of 961 microns degrees. It is believed that as the roughness increases, the shadowing is not as influential as with the less rough samples. In the less rough samples, the change of view angle shadows more of the valleys than with the rougher samples, allowing the emissivity to decrease significantly.

When looking at the ranges of emissivity seen among the samples, it was observed that the 45 degree view angle had the smallest range of emissivity between the different samples tested. As can be seen in Figure 74 the emissivity values remain close between the majority of samples across the temperature range investigated.

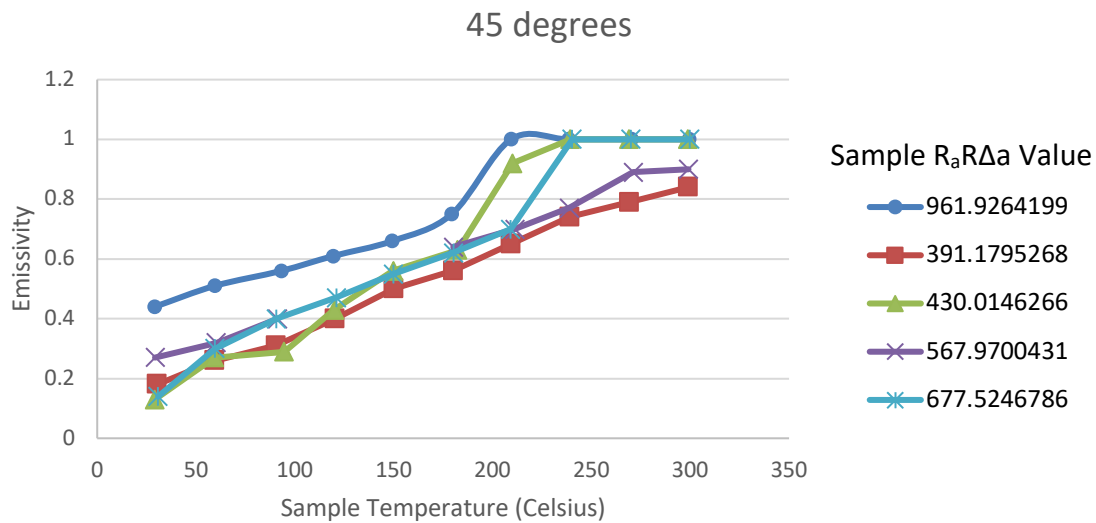


**Figure 74:** 45 Degree View Angle Emissivity Results for All Tested Samples.

Due to this smaller range, it would create smaller temperature errors if the variable surface roughness effects on emissivity were not considered. However, if emissivity was not measured at this 45 degree view angle initially, but assumed to be the value of the 0 degree, or normal to the surface plane, then the temperature errors would be the largest at the lower temperature ranges since the emissivity drastically decreases between the 0 and 45 degree view angles.

To demonstrate the temperature errors possible due to incorrect emissivity assumptions, a test case was calculated. The test case assumed a single emissivity value as an estimate for the emissivity of all. The samples used in this test case in addition to the sample whose emissivity was used as the estimate for all were built using standard build conditions to obtain temperature errors that would most likely be seen in the majority of metallic laser powder bed fusion AM builds. The assumed emissivity was chosen to be measured with the MWIR camera at the 0 degree view angle for the sample

that was built using 100 watts laser power and 1400 mm/s scan speed, with a RaRda value of  $391 \mu\text{m}^\circ$ . Two emissivity values were used in the temperature error calculations. The first set used an emissivity measured at room temperature to see what the possible temperature errors would be when the dependence on temperature, view angle, and surface roughness of the emissivity was ignored. The second set used an emissivity value of the sample that was measured at the test temperature of  $150^\circ$  Celsius, which was the temperature assumed for all the samples. This set would be looking at the effects of the dependence on view angle and surface roughness if emissivity were not taken into account. Results of the temperature error calculations can be found below in Table 16. Errors that are negative in the table represent a perceived colder value than the true sample temperature.

**Table 16:** Possible Temperature Errors Due to Incorrect Emissivity Assumptions.

	Ra×RΔa Value	Estimated Emissivity taken at 0 degree view angle and 30° C			Estimated Emissivity taken at 0 degree view angle and 150° C		
		0 degree	30 degree	45 degree	0 degree	30 degree	45 degree
<b>Sample 1</b>	$391 \mu\text{m}^\circ$	17 °C	25 °C	18 °C	0 °C	-12 °C	-18 °C
<b>Sample 2</b>	$430 \mu\text{m}^\circ$	49 °C	25 °C	22 °C	7 °C	-12 °C	-15 °C
<b>Sample 3</b>	$567 \mu\text{m}^\circ$	49 °C	30 °C	22 °C	-5 °C	2 °C	-6 °C
<b>Sample 4</b>	$961 \mu\text{m}^\circ$	49 °C	43 °C	33 °C	13 °C	-9 °C	-14 °C

All of the above results and conclusions drawn from the elevated temperature measurements are applicable to the mid-wave infrared range, 3-5 microns. For the shorter wavelength infrared cameras that operate in 0.75-3 micron range, the effects of surface roughness will be stronger, while for longer wavelengths (8-13 microns), as can be seen by the room temperature comparison, the effects will be weaker.

## **CHAPTER 3: IN-SITU MEASUREMENTS**

The purpose of this task is to determine if there is a suitable method for measuring the surface roughness of the as built surface in-situ to adjust the emissivity input for a thermal monitoring instrument throughout an additive build. Since a combination of already existing surface roughness parameters was found to have a good relationship with emissivity changes, the task now is to allow that knowledge to be applied to improve the accuracy of in-situ thermal measurements. To disturb the build or machine as little as possible, non-contact methods will be investigated for this purpose. Traditional contact methods, such as stylus based, require too much space and mechanical integration to be sensible in an additive manufacturing machine. In addition to requiring too much space, contact methods are not suited to the very rough surfaces of metallic AM parts, as was discussed when selecting a proper method to measure the surface roughness of the parts for the first task of this study. Once a suitable non-contact method has been selected, the in-situ measurements will be compared to measurements taken with already proven ex-situ methods to analyze its capabilities. From this comparison it will be determined if the in-situ measurement technology is suited to assist in in-situ emissivity adjustments based on changing surface roughness during a AM build.

### **Surface Topography Measurement Technique Selection Process**

There were several different non-contact measurement methods considered. The majority of all the technologies considered were found to be post-process measurement methods in literature as the in-situ measurement of surface roughness in AM builds has not gained popularity. In a review of optical techniques currently used for post-process

measurement of metallic AM surfaces, it was suggested that active systems, those that provide their own means of surface illumination, have an advantage over passive systems in that they do not require a certain level of roughness to have identifiable features that are used relate images [49].

One of the active methods considered is laser triangulation, which uses triangulation to calculate the height of the surface at distinct points. This method was considered since its footprint near the build surface is minimal and could possibly be integrated into an AM machine. However, one major issue that arises with laser triangulation is that as the metallic AM surface's roughness value approaches and exceeds the wavelength of the laser light used, scattering of the light by the surface increases, thereby increasing the uncertainty in the measurement [49].

One method considered was Raman spectroscopy. This method uses the intensity of reflected spectra from a surface of interest to measure an increase in surface roughness [50]. In Beard et al., the level of sintering was investigated by measuring the relative surface roughness between AM samples with the understanding that the smoother surface had a higher degree of sintering. In the study, it was found that the intensity of the backscattered spectrum increased as the AM surface roughness increased [50]. The major disadvantage for this technique is that it is currently only being used as a relative measurement technique instead of measuring the absolute height of the surface. Therefore, it is not a feasible method for measuring in-situ surface roughness for the purpose of emissivity adjustment.

Another active measurement technique considered is projection Moiré profilometry. This method works by projecting a pattern of black and white lines onto the measured surface. Due to the deviations in surface height, the pattern is distorted on the surface. The distorted pattern is captured with a camera which is then digitally overlaid with the original pattern, creating an interferogram. The resultant interferogram is then used to create a 3D height map of the surface [49]. This method is not sensitive to the roughness of the parts like laser triangulation, but in order to achieve high resolution, dense patterns need to be used, which decreases measurement area [49]. One disadvantage to this method for implementation into a machine is that it requires two pieces of hardware, the projector and camera, to have a clear view of the build surface, which can be difficult. This machine implementation has been performed before in Zhang et al., where a projector was placed at an angle to the build surface with the camera at a position directly normal to the build surface [51]. While this study was able to physically implement the measurement instruments into the AM machine, one issue they did identify was that the brightness level of the projector is key since the level of surface reflection can change based on the level of sintering seen during the process [51]. Since the accuracy of the technique depends upon the reflection, which is dependent on the roughness, this measurement technique is not the most suitable method for the purposes of this study.

Another method considered was optical coherence tomography (OCT). OCT traditionally is used for medical imaging of certain soft tissues such as the human eye [52]. How this technique works is that a laser beam is split in two to travel through either

a reference arm or to the sample. In the sample path, the light travels through the material and is either transmitted, absorbed, or reflected back into the optical train of the system. The backscattered light from the sample is combined with the light that traveled through the reference arm to create an interference pattern. This pattern is then analyzed to generate a 1D image of this sample. This process is repeated along a line or area, to generate 2D or 3D images, respectively [52]. The specific type of OCT investigated is spectral-domain, which uses a range of wavelengths to generate the several interference patterns in a short amount of time to determine the height of a sample. [53]. With this type of OCT, acquisition speeds of at least 50 kHz can be achieved [53]. With additive manufacturing laser scan speeds reaching up to 2000 mm/s in this study, large sampling rates are needed for accurate measurements. This measurement technique has already been applied in AM machines both for metals and polymers [53, 52]. The main disadvantage with this method is that as the measurement area of interest is farther removed from the center of the build surface, the time of flight increase between the light source and the sample surface, causing an artificial distortion of the surface in addition to greater uncertainty in the measurement [53].

The method chosen to proceed forward with was the spectral-domain optical coherence tomography (SD-OCT). This method was chosen due to its high sampling rate, ease of machine integration, and high resolution. The other measurement techniques like laser triangulation and Moiré profilometry required significant space for instrument installation, which is difficult to find in metal AM machines. In addition to this, methods such as laser triangulation, are sensitive to certain levels of roughness that approach the

wavelength of light used, which is the same phenomenon that was a driving force behind this study. Therefore, this method is not suitable for the wide range of roughness that are to be investigated in this study. Another reason SD-OCT was chosen was the ease of access as the system used at Lawrence Livermore National Labs was already integrated into an Aconity Lab laser powder bed fusion (L-PBF) machine and ready for testing [53].

One disadvantage for most optical methods of surface metrology is that the area of surface they can accurately measure is limited by their line of sight [49]. Therefore, either the area of measurement or the build area needs to be limited, which is not feasible. Therefore, having multiple locations of measurement is the most likely method to negate this issue. However, the problem will not be addressed, as the purpose of this task is to look at the feasibility of the selected method in measuring the surface roughness parameters of interest with the express purpose of adjusting the emissivity input of a thermal monitoring instrument on a layer wise basis.

### **Experimental Procedure**

To test the ability of the OCT technique to measure in-situ surface topography, a system which had already been integrated into an Aconity Lab L-PBF research machine was leveraged. The OCT system and AM machine was owned by the AM group at Lawrence Livermore National Laboratory. The leveraged OCT system was a LD-600 (Laser Depth Dynamics) [53]. The estimated experimental axial resolution was ~25 microns while the lateral resolution was calculated to be about 5 microns. Although the lateral resolution is high, to reduce the signal to noise ratio of the measured reflected

light, several A scans were averaged together to strengthen the signal, which could cause the smoothing of features that are of interest to this study. Its effect will be discussed during the results section. Further details about the system and machine settings can be found in DePond et al. [53].

Nine parts with roughly a 1 cm square cross section with a slight protrusion on one side to allow for ease of orienting the measurement data was built. The parts were built using SS 316L powder with an average particle size of 30-50 microns. The scan strategy was a serpentine pattern with scan lines parallel to the edges of the cube with a 90 degree rotation between layers. The other build settings used consistently for all the parts can be found in Table 17 below. The Aconity Lab L-PBF machine uses a brush for spreading the powder and no compaction step afterward. An image showing some of the parts can be found in Figure 75 below.

**Table 17:** OCT Part Build Settings.

Layer Thickness	Hatch Spacing	Laser Spot Size
50 microns	100 microns	100 microns

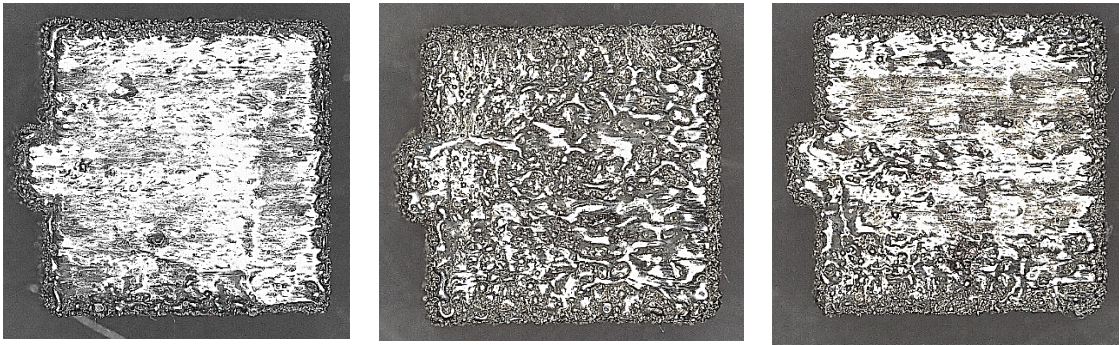


**Figure 75:** Stainless Steel 316 Cubes Built for OCT Measurement Test **(Left to Right):** Cube 2, Cube 7, Cube 9.

Each part was built with a different volumetric energy density, caused by changing the laser power while maintain a constant steady state scan speed. The build parameters can be found below in Table 18.

**Table 18:** Build Parameters for OCT AM Specimens.

<b>Cube Number</b>	<b>Laser Power (W)</b>	<b>Scan Speed (mm/s)</b>
1	140	380
2	170	380
3	200	380
4	230	380
5	260	380
6	290	380
7	320	380
8	350	380
9	380	380

The parts were built to completion and the OCT system was then used to measure the surface topography of the final layer of the build. The final layer was the only layer of interest since the ex-situ measurement technique could only measure the surface of the top/final layer.

Once the parts were built, they were sent to Sandia National Laboratories where the top surfaces were measured using the Keyence VR3100 visual microscope. A range of magnifications, with different lateral resolutions, were used to provide a variety of calculated surface roughness parameters to compare to those calculated with the OCT surface height data. Four magnifications were used and the resolutions of each of these can be found in Table 19 below.

**Table 19:** Keyence VR3100 Measurement Resolution Based on Magnification Level.

<b>VR3100 Zoom</b>	<b>Height Resolution</b>	<b>Lateral Resolution</b>
12x	0.1 micron	23.44 microns
40x	0.1 micron	7.42 microns
80x	0.1 micron	3.71 microns
160x	0.1 micron	1.86 microns

The reasoning behind the multiple magnifications was that it was found in the first task of this study that the value of the calculated surface parameter product of  $R_a$  and  $R\Delta a$  depended on the magnification used to obtain the height data. As seen in Figure 76, the level of fit of the calculated roughness parameters to the measured emissivity depended on the level of magnification. It is also interesting to note that although between magnifications, the lateral resolution increases by a factor of roughly two, the level of fit approaches more of a steady state than continually increasing.

All the surface data both from the Keyence VR3100 and the OCT system were analyzed using the custom MATLAB script discussed in the first task section. This MATLAB program removed any underlying tilt in the data before measuring the desired surface roughness parameters.

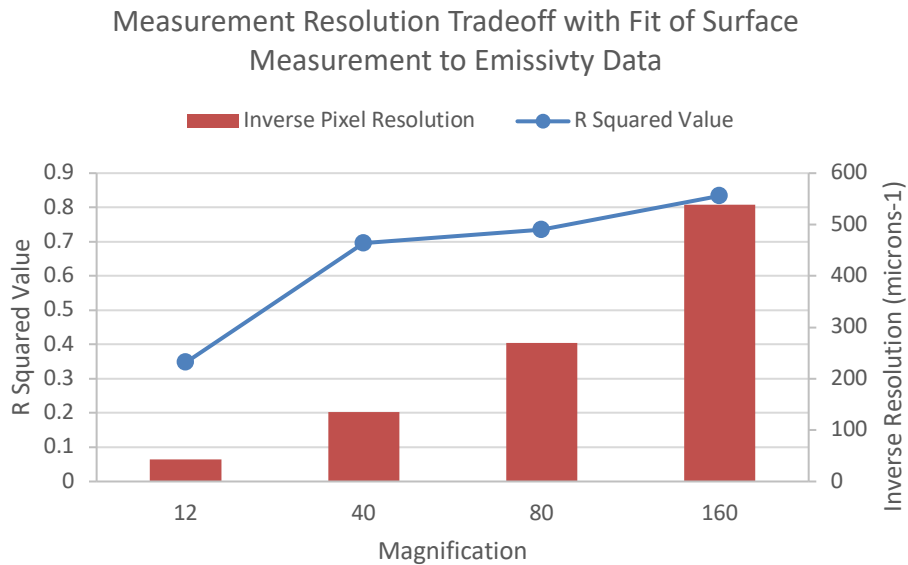


**Figure 76:** Effects of Surface Topography Measurement Magnification on Level of Fit with Emissivity Trends.

## Results

The critical measurements taken with both techniques as seen in the results from the first task are  $R_a$  and  $R\Delta a$ , since the product of these two parameters have the best relationship with emissivity trends. Absolute and percent deviations were calculated between the surface roughness parameter values calculated using the raw OCT data and height data measured with the Keyence VR3100. The results can be found in Table 20 below.

**Table 20:** Surface Roughness Differences between Measurement Techniques.

<b>VR3100 Magnification</b>	<b><math>R_a</math> Deviation (Microns)</b>	<b>Average <math>R_a</math> Percent Deviation</b>	<b><math>R\Delta a</math> Deviation (Degrees)</b>	<b>Average <math>R\Delta a</math> Percent Deviation</b>
12x	4.53	26.33	5.53	60.94
40x	5.78	30.28	7.30	69.15
80x	0.35	44.89	9.20	76.87
160x	2.56	63.93	11.43	80.74

The measured  $R_a$  from the OCT data was larger compared to the low magnifications, 12x and 40x, but was lower in value when compared to the higher magnifications of 80x and 160x from the Keyence VR3100. The lower  $R_a$  values measured with OCT compared to the higher magnifications of the Keyence was most likely a result of the lower resolution of the OCT system that did not allow it to accurately capture the smaller peaks and valleys that would be smoothed out due to the lack of resolution. Another result of the lower resolution of the OCT system is that the  $R\Delta a$  values calculated with its height data were consistently lower than those calculated with the Keyence data. It is also thought that the smoothing of data is occurring due to the averaging of the A scans during the pre-processing phase of the OCT data analysis. This would result in a lower  $R\Delta a$  since steeper features could be smoothed out with the step.

Although the percent deviations are significant in value, the resultant product of these two surface parameters, which was the key number found back up in the first task, and estimated emissivity values between those calculated with the OCT and Keyence measurements are close in value. The estimated emissivity value used the best fit line equation from the 160x magnification surface roughness vs emissivity graph seen in Figure 59. As seen in Figure 77 below, although the product of  $R_a$  and  $R\Delta a$  measurements vary between the measurement techniques, the average difference in estimated emissivity values is about 0.04.

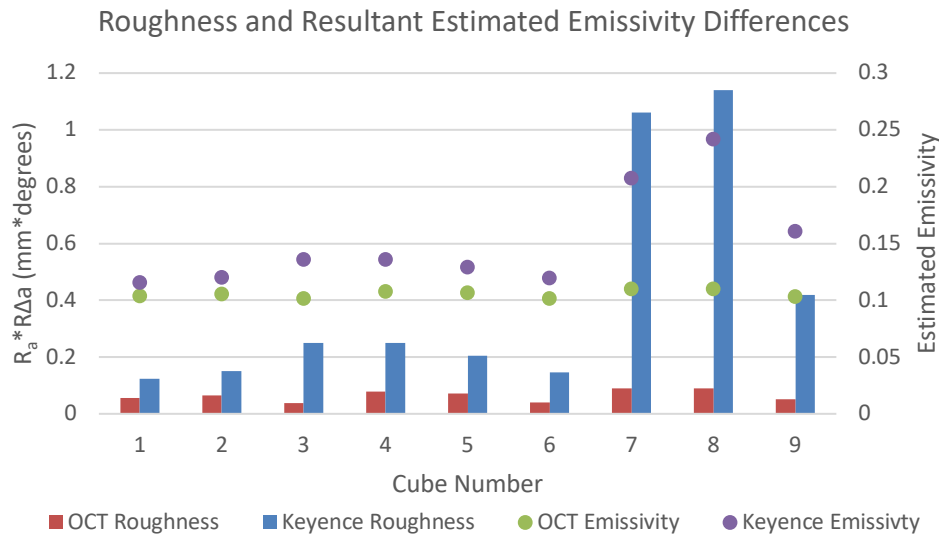


**Figure 77:** OCT and Keyence Microscope Surface Roughness Differences and Resultant Emissivity Differences.

## Conclusion

In observing the surface roughness measurements and estimated emissivity values, it is believed that the OCT technique is a viable measurement method for the in-situ adjustment of emissivity based on surface topography. Although the measurements varied from the ex-situ Keyence VR3100 measurements, the estimated emissivity for the two methods were close in value. However, the emissivity value was for a wavelength range of 2.5-24 microns. As the wavelength range of interest gets shorter, for example with the SWIR cameras that operate at 1-3 microns, the effect of the surface roughness measurement differences will increase. Therefore, it is suggested a higher resolution OCT be developed to ensure higher accuracy for the shorter measurement wavelengths commonly used in metal AM thermal monitoring methods.

## OVERALL CONCLUSIONS

Through this study it was found that the emissivity of metallic additively manufactured parts can be significantly influenced by their surface roughness. For this to occur, the ratio of root mean square roughness of the surface to the observation wavelength must be equal or greater than one, which is known as the geometric optical region. This is a common occurrence as metallic AM surfaces are very rough and shorter wavelengths are used for thermal measurements due to the high temperatures, whose peak radiation becomes shorter with increasing temperature, seen in the metallic AM processes. Through the simulation work, it was determined that the geometry of the valleys that compose the surface was the most influential geometric feature of the surface in observed emissivity trends. This can be explained with the Mendenhall wedge effect, which states that as a valley angle decreases, the amount of internal reflections increases, increasing the absorption, and thereby increasing the emissivity. This knowledge was leveraged during the experimental measurements of surface roughness and emissivity. It was determined that the product of  $R_a$  (arithmetic mean height) and  $R\Delta a$  (average tilt angle) for a given surface produced the best correlation to the emissivity of that surface. These parameters agree with the Mendenhall wedge effect since they describe the height and angle of the valleys that compose the surface. It was also found that arithmetic mean surface roughness,  $R_a$ , although a popular descriptor for surfaces in general, was a very poor indicator of emissivity trends as surfaces would have the same arithmetic mean height, but different shapes and therefore different emissivity values.

Not only does the surface roughness need to be considered when estimating the emissivity of a metallic AM surface, but also the view angle of the observation instrument. It was found that as the view angle increases, when measured relative to the surface normal, the observed emissivity value decreases. This observation can be attributed to the shadowing effect, which decreases the internal valley reflections discussed above and prevents radiation from reaching the measurement instrument. It was also found that of the three view angles tested, the 45 degree view angle had the least spread between samples, so could be the better view angle to have measurement instruments placed so that incorrect emissivity assumptions would have minimal temperature error compared to other view angles.

In order to test the viability of this information to adjust emissivity values in-situ, a method for measuring the surface roughness during a build was determined. Optical coherence tomography (OCT) was the method chosen and tested. It was found that the technology was suitable to measuring roughness in-situ on a layerwise basis. The accuracy of the OCT system was sufficient in producing minimal errors in calculated emissivity.

### **Future Work**

There are several aspects to be discussed for the continuation of this study. First and foremost, this study will be performed on other common metallic materials used in the AM processes. The correlation between what ideal surface roughness parameters determined in this study and emissivity for different metallic materials will be

investigated. In addition to new materials, the phenomena of the shadowing effect, which produces different emissivity values for different view angles will be fundamentally studied through simulation work. In addition to the simulation work, the influence of the various observation wavelengths on the shadowing effect will be studied by leveraging different cameras, such as a SWIR and LWIR for the elevated temperature measurements. Finally, to combine all segment of this study, an infrared camera and OCT system will be implemented simultaneously to test the accuracy of thermal measurements when estimating the emissivity that uses in-situ surface roughness measurement.

## Appendix A - Surface Roughness vs Emissivity Analysis

**Table 21:** Correlation Strengths of Surface Roughness Parameters and Combinations of Parameters to Measured Sample Emissivity

Surface Roughness Parameter or Combination of Parameters	Description	R <sup>2</sup> Value
R <sub>a</sub>	Arithmetic Mean Surface Height	0.66
R <sub>rms</sub>	Root Mean Square Roughness	0.67
R <sub>sk</sub>	Skewness	0.38
R <sub>ku</sub>	Kurtosis	0.34
Pc/mm	Peak Count per Millimeter	0.02
RΔa	Arithmetic Tilt Angle	0.8
RΔq	Root Mean Square Slope	0.79
Valley Height ÷ Valley Width	Average Value of Individual Valley Height Divided by Valley Width	0.46
Average Valley Angle	Average Angle of Valleys that Compose the Surface	0.38
Average Valley Angle ÷ Valley Height	Average Value of Individual Valley Angle Divided by Valley Height	0.82
R <sub>a</sub> × RΔa	Arithmetic Mean Height Multiplied by Arithmetic Tilt Angle	0.83
RΔq × R <sub>a</sub>	Root Mean Square Slope Multiplied by Arithmetic Mean Height	0.83
R <sub>rms</sub> × RΔq	Root Mean Square Roughness multiplied by Root Mean Square Slope	0.82
Average Valley Angle ÷ R <sub>a</sub>	Average Valley Angle Divided by Arithmetic Mean Height	0.7
Average Valley Angle ÷ RΔa	Average Valley Angle Divided by Arithmetic Tilt Angle	0.66
Average Valley Angle ÷ R <sub>rms</sub>	Average Valley Angle Divided by Root Mean Square Roughness	0.72
R <sub>sk</sub> × RΔa	Skewness Multiplied by Arithmetic Tilt Angle	0.47
R <sub>a</sub> × R <sub>sk</sub>	Arithmetic Mean Height Multiplied by Skewness	0.51
R <sub>a</sub> × R <sub>ku</sub>	Arithmetic Mean Height Multiplied by Kurtosis	0.65

## REFERENCES

- [1] A. Townsend, N. Senin, L. Blunt, R. K. Leach and J. S. Taylor, "Surface Texture Metrology for Metal Additive Manufacturing: A Review," *Precision Engineering*, no. 46, pp. 34-47, 2016.
- [2] S. Price, J. Lydon, K. Cooper and K. Chou, "Experimental Temperature Analysis of Powder-Based Electron Beam Additive Manufacturing," in *Solid Freeform Fabrication Symposium*, Austin, 2012.
- [3] B. Cheng, J. Lydon, K. Cooper, V. Cole, P. Northrop and K. Chou, "Melt Pool Dimension Measurement In Selevtive Laser Melting Using Thermal Imaging," in *Solid Freeform Fabircation Symposium*, Austin, 2017.
- [4] E. Rodriguez, F. Medina, D. Espalin, C. Terrazas, D. Muse, C. Henry, E. MacDonald and R. B. Wicker, "Integration of a Thermal Imaging Feedback Control System in Electron Beam Melting," in *Solid Freeform Fabrication Symposium*, Austin, 2012.
- [5] J. H. Taylor, *Radiation Exchange: An Introduction*, San Diego: Academic Press, INC., 1990.
- [6] R. Murphy, "A Review of In-situ Temperature Measurements," in *NCSL International*, 2016.
- [7] T. L. Bergman, A. S. Lavine, F. P. Incropera and D. P. Dewitt, *Introduction to Heat Transfer*, Hoboken: John Wiley & Sons, Inc., 2011.
- [8] FLIR Systems, AB, "The Ultimate Infrared Handbook for R&D Professionals," FLIR AB.
- [9] ASME, *B46.1: Surface Texture (Surface Roughness, Waviness, and Lay)*, 2009.
- [10] International Organization for Standardization, *Geometric Product Specifications (GPS) - Surface Texture: Profile Method - Terms, Definitions, and Surface Texture Parameters*, Geneva, 1997.
- [11] Keyence Corporation, "Area Roughness Parameters," 2019. [Online]. Available: <https://www.keyence.com/ss/products/microscope/roughness/surface/sdq-root-mean-square-gradient.jsp>. [Accessed 31 January 2019].
- [12] G. Strano, L. Hao, R. Everson and K. Evans, "Surface Roughness Analysis, Modelling, and Predition in Selective Laser Melting," *Journal of Materials Processing Technology*, no. 213, pp. 589-597, 2012.
- [13] Y. Tian, D. Tomus, P. Rometsch and X. Wu, "Influence of Processing Parameters on Surface Roughness of Hastelloy X Produced by Selective Laser Melting," *Additive Manufacturing*, pp. 103-112, 2017.
- [14] M. Rombouts, G. MAes, W. Hendrix, E. Delarbre and F. Motmans, "Surface Finish After Laser Metal Deposition," *Physics Procedia*, no. 41, pp. 810-814, 2013.

- [15] S. Kleszczynski, A. Ladewig, K. Friedberger, J. zur Jacobsmuhlen, D. Merhof and G. Witt, "Position Dependency of Surface Roughness in Parts from Laser Beam Melting Systems," in *Solid Freeform Fabrication Symposium*, Austin, 2015.
- [16] J. C. Fox, S. P. Moylan and B. M. Lane, 30 June 2016. [Online]. Available: [www.nist.gov](http://www.nist.gov). [Accessed February 2018].
- [17] T. Kralik, P. Hanzelka, V. Musilova and A. Srnka, "Factors Influencing Thermal Radiative Properties of METals," in *The 13th Cryogenics IIR International Conference*, Prague, 2016.
- [18] C.-D. Wen and I. Mudawar, "Modeling the Effects of Surface Roughness on the Emissivity of Aluminum Alloys," *International Journal of Heat and Mass Transfer*, no. 49, pp. 4279-4289, 2006.
- [19] W. Sabuga and R. Todtenhaupt, "Effect of Roughness on the Emissivity of the Precious Metals Silver, Gold, Palladium, Platinum, Rhodium, and Iridium," in *15th European Conference on Thermophysical Properties*, Wurzburg, 1999.
- [20] SPIE Europe, "Optical software: which program is right for me?," 21 July 2006. [Online]. Available: [optics.org/article/25404](http://optics.org/article/25404). [Accessed 31 October 2018].
- [21] Lumerical, "FDTD," 2018. [Online]. Available: [https://kb.lumerical.com/solvers\\_finite\\_difference\\_time\\_domain.html](https://kb.lumerical.com/solvers_finite_difference_time_domain.html). [Accessed May 2018].
- [22] Lumerical Inc., "Material Permittivity Models," 2018. [Online]. Available: <http://kb.lumerical.com>. [Accessed 25 May 2018].
- [23] S. B. Boyden and Y. Zhang, "Temperature and Wavelength-Dependent Spectral Absorptivities of Metallic Materials in the Infrared," *Journal of Thermophysics and Heat Transfer*, vol. 20, no. 1, pp. 9-15, January-March 2006.
- [24] Wikipedia, "Drude Model," 8 January 2019. [Online]. Available: [https://en.wikipedia.org/wiki/Drude\\_model](https://en.wikipedia.org/wiki/Drude_model). [Accessed 15 January 2019].
- [25] Lumerical Inc., "Simulation - FDTD," 2018. [Online]. Available: <http://kb.lumerical.com>. [Accessed 25 May 2018].
- [26] Lumerical Inc., "Mesh Refinement," [Online]. Available: <https://kb.lumerical.com/en>. [Accessed 13 December 2018].
- [27] T. L. Bergman, A. S. Lavine, F. P. Incropera and D. P. Dewitt, *Introduction to Heat Transfer*, Hoboken: John Wiley & Sons, Inc., 2011.
- [28] Lumerical Inc., "Monitors - Frequency-Domain Field Profile," [Online]. Available: <https://kb.lumerical.com>. [Accessed 13 December 2018].
- [29] Lumerical Inc., "Lumerical University: FDTD 100," Open edX, [Online]. Available: <https://edu.lumerical.com>. [Accessed 5 June 2018].
- [30] S. Y. Jeong, C. Y. Tso, Y. M. Wong and C. Y. Chao, "FDTD Simulations Inspired by the Daytime Passive Radiative Cooling of the Sahara Silver Ant," in *4th International Conference On Building Energy, Environment*, Melbourne, 2018.

- [31] Y. Yang and R. O. Buckius, "Surface Length Scale Contributions to the Directional and Hemispherical Emissivity and Reflectivity," *Journal of Thermophysics and Heat Transfer*, vol. 9, no. 4, pp. 653-659, 1995.
- [32] C. E. Mendenhall, "On the Emissivity Power of Wedge-Shaped Cavities and Their Use in Temperature Measurements," *The Astrophysical Journal: An International Review of Spectroscopy and Astronomical Physics*, vol. XXXIII, no. 2, pp. 91-97, 1911.
- [33] "ProX DMP 200," 2018. [Online]. Available: <https://www.3dsystems.com/3d-printers/prox-dmp-200/specifications>. [Accessed 26 October 2018].
- [34] I. Gibson, D. Rosen and B. Stucker, *Additive Manufacturing Technologies: 3D Printing, Rapid Prototyping, and Direct Digital Manufacturing*, New York: Springer, 2015.
- [35] J. R. Koepke, "The Influence of Process Variables on Physical and Mechanical Properties in Laser Powder Bed Manufacturing," University of New Mexico, Albuquerque, 2019.
- [36] T. Grimm, G. Wiora and G. Witt, "Characterization of Typical Surface Effects in Additive Manufacturing with confocal Microscopy," *Surface Topography: Metrology and Properties*, no. 3, pp. 1-12, 2015.
- [37] Keyence Corporation, "VR-3100 - Wide-Area 3D Measurement System Sensor Head," 2018. [Online]. Available: <https://www.keyence.com>. [Accessed 25 May 2018].
- [38] Surface Optics Corporation, "SOC-100 HDR Hemispherical Directional Reflectometer," 2018. [Online]. Available: <https://surfaceoptics.com>. [Accessed 24 May 2018].
- [39] Physical Electronics, Inc., "Auger Electron Spectroscopy," 2019. [Online]. Available: <https://www.phis.com/surface-analysis-techniques/aes.html>. [Accessed 13 March 2019].
- [40] D. Bergstrom, J. Powell and F. H. Kaplan, "The Absorption of Light by Rough Metal Surfaces - A Three-dimensional Ray-tracing Analysis," *Journal of Applied Physics*, no. 103, pp. 103515:1-12, 2008.
- [41] P. P. Woskov and S. K. Sundaram, "Thermal Return Reflection Method for Resolving Emissivity and Temperature in Radiometric Measurements," *Journal of Applied Physics*, vol. 92, no. 10, pp. 6302-6310, 2002.
- [42] Kurt J. Lesker Company, "CF Flanged Zero Length Sapphire Viewports," 2019. [Online]. Available: <https://www.lesker.com>. [Accessed 12 March 2019].
- [43] S. Price, J. Lydon, K. Cooper and K. Chou, "Temperature Measurements in Powder-Bed Electron Beam Additive Manufacturing," in *Proceedings of the ASME 2014 International Mechanical Engineering Congress and Exposition*, Montreal, 2014.

- [44] H. Krauss, C. Eschey and M. F. Zaeh, "Thermography for Monitoring the Selective Laser Melting Process," in *Solid Freeform Fabrication Symposium*, Austin, 2012.
- [45] S. Whetten, Interviewee, *LENS Processing Temperatures*. [Interview]. 24 May 2018.
- [46] J. Zivcak, M. Sarik and R. Hudak, "FEA Simulation of Thermal Processes During the Direct Metal Laser Sintering of Ti64 Titanium Powder," *Measurement*, no. 94, pp. 893-901, 2016.
- [47] Y. Li, K. Zhou, P. Tan, S. B. Tor, C. K. Chua and K. F. Leong, "Modeling Temperature and Residual Stress Fields in Selective Laser Melting," *International Journal of Mechanical Sciences*, no. 136, pp. 24-35, 2018.
- [48] M. C. Larciprete, Y. S. Gloy, R. L. Voti, G. Cesarini, G. Leahu, M. Bertolotti and C. Sibilio, "Temperature Dependent Emissivity of Different Stainless Steel Textiles in the Infrared Range," *International Journal of Thermal Sciences*, no. 113, pp. 130-135, 2017.
- [49] P. I. Stavroulakis and R. K. Leach, "Invited Review Article: Review of Post-process Optical Form Metrology for Industrial-grade Metal Additive Manufactured Parts," *Review of Scientific Instruments*, no. 87, 2016.
- [50] M. A. Beard, O. R. Ghita and K. E. Evans, "Using Raman Spectroscopy to Monitor Surface Finish and Roughness of Components Manufactured by Selective Laser Sintering," *Journal of Raman Spectroscopy*, no. 42, pp. 744-748, 2010.
- [51] B. Zhang, J. Ziegert, F. Farahi and A. Davies, "In Situ Surface Topography of Laser Powder Bed Fusion Using Fringe Projection," *Additive Manufacturing*, no. 12, pp. 100-107, 2016.
- [52] A. Lewis, A. McElroy, T. Milner, S. Fish and J. Beaman, "Initial Investigation of Selective Laser Sintering Laser Power vs. Part Porosity Using In-Situ Optical Coherence Tomography," in *Proceedings of the 28th Annual International Solid Freeform Fabrication Symposium - An Additive Manufacturing Conference*, Austin, 2017.
- [53] P. J. DePond, G. Guss, S. Ly, N. P. Calta, D. Deane, S. Khairallah and M. J. Matthews, "In Situ Measurements of Layer Roughness During Laser Powder Bed Fusion Additive Manufacturing Using Low Coherence Scanning Interferometry," *Materials & Design*, 2018.